

**Design, Modeling and Fabrication of a  
Copper Electroplated MEMS, Membrane Based Electric Field Sensor**

**By Ehsan Tahmasebian**

A THESIS SUBMITTED TO THE FACULTY OF GRADUATE STUDIES OF  
THE UNIVERSITY OF MANITOBA  
IN PARTIAL FULFILLMENT OF THE REQUIREMENTS FOR THE DEGREE OF  
MASTER OF SCIENCE

Department of Electrical and Computer Engineering  
University of Manitoba  
Winnipeg, Manitoba  
© Copyright by Ehsan Tahmasebian, 2014

*For my amazing Parents,*

*My dear supportive brothers and sisters*

*And*

*My beloved Samira*

## **Abstract**

A MEMS based electrostatic field sensor is presented which uses capacitive interrogation of an electrostatic force deflected microstructure. First the deflection of the sensor's membrane which is caused by electrostatic force in the presence of electric field is calculated both by simulation and theoretical model and it has been shown that the results of the simulations have acceptable values compared to the theoretical ones. Simulation models have also been designed to improve the vibration of the membrane for measuring the ac electric fields. It has been shown that by adding perforations to the surface of the membrane, it is possible to reduce the air drag force effect on the membrane and still have similar electrostatic force on the membrane. Therefore, it is possible to reduce the damping due to air resistance in membrane movement when measuring ac fields. After successful modeling of the sensor structure, the fabrication process for the sensor has been designed. The electroplating process as the most important fabrication step has been studied in detail prior to starting the fabrication of sensor. The process parameters for electroplating process, such as current amplitudes, duty cycle and frequency have been optimized to get the lowest surface roughness to thickness ratio for the electroplated films. A lithography molding process was developed for the electroplating. Both dc and pulse plated films have been studied to show the role of pulse plating in improving the quality of the electroplated films. It was found during the release process that the electroplated copper interacted with sulfur during plasma etching of silicon. However, the result of the releasing process was very helpful to find the best recipe of releasing and they can be used in next projects.

## **Acknowledgements**

First and foremost, I would like to thank my advisor, Dr. Cyrus Shafai, for his valuable support and patience during my master's study. His guidance, made me able to find the right path and the discussions that we had always gave me great ideas to overcome all difficulties that I had during my research.

I would also like to thank all graduate student members of Dr.Shafai's group. Their ideas and advises were always helpful during my research, specifically Mr. Yu.Zhou for his great suggestions during my COMSOL simulations. I also want to thank Mr. Yu.Zhou and Mr. Tao Chen for their invaluable assistant in the cleanroom and helping me to be trained to work with clean room facilities.

I am truly thankful to Mr.Dwayne Chrusch, The manager of the NFSL lab, for his patience and care during my training in the cleanroom, running the NSFL facilities and, always being available for tuning and fixing the facilities. Besides, his experiences on practical fabrication process aided me a lot and I really appreciate that.

The support from CMC microsystems for providing the simulation software tools is highly appreciated.

I would like to thank all my friends in Canada who helped me for being settled in a new city and country. I enjoyed every single day of my stay in Winnipeg among them and their company was warm enough that I barely notice the cold winters of Winnipeg.

The last but not the least, I would like to express my deepest appreciation to my loving family. No matter how far was the physical distance between us, I always felt their

endless support and care and they were always close in my heart. I am so glad to have the most amazing and supportive parents in the world. I have truly the most wonderful siblings, their manner and profession always let me to feel proud of my family and was the best courage for me, to do my best and improve myself to be like them. My sincere gratitude goes to my beloved fiancée, Samira, for being always understanding and caring during my studies. I appreciate her patience for tolerating my absence for three years and always being amazingly supportive and loving in my most difficult times of studies.

## Table of Contents

1. Chapter One: INTRODUCTION .....	1
1.1 Electric field measurements applications .....	2
1.2 dc electric field measurement .....	3
1.3 dc Electric Field Measurement Techniques .....	4
1.3.1 The Electro-optic meter .....	4
1.3.2 Induction Probes .....	5
1.3.3 Electric Field Mills .....	6
1.3.4 Micromachined Electric Field sensors .....	7
1.4 MEMS electric field sensor of this thesis and project objectives .....	13
2. Chapter Two: Theory .....	14
2.1 Introduction .....	15
2.2 Sensor Design and Operation Principle .....	17
2.2.1 Design.....	17
2.2.2 Operation Principle .....	18
2.3 Electrostatic theory.....	19
2.4 Mechanical Theory.....	23
2.5 Spring-Mass system .....	28
2.5.1 Over damped .....	30
2.5.2 Under damped .....	30
2.5.3 Critically damped .....	31
2.5.4 Mode of damping for the designed sensor of this project .....	31
3. Chapter Three: Sensor Modeling & Simulations.....	33
3.1 Use of COMSOL Multiphysics.....	34
3.2 Simulations and Results .....	38
3.2.1 Membrane deflection under DC field .....	38
3.3 New design for solving the damping under ac field .....	40

3.3.1	Membrane with holes to reduce the air drag.....	41
3.3.2	Air drag effect on the sensor motion for incident ac electric fields .....	44
3.4	Natural frequencies of the different structures .....	58
3.5	Sensor Output vs. Electric Field .....	60
3.6	Conclusions .....	61
3.7	Future Work.....	62
4.	Chapter Four: Sensor Fabrication .....	63
4.1	Silicon wafer back etching and photoresist mold patterning.....	65
4.1.1	Silicon wafer back etching and mold patterning process design.....	65
4.1.2	Mask design .....	68
4.1.3	Silicon wafer back etching process .....	74
4.1.4	Frontside metallization .....	79
4.1.5	Photoresist mold patterning for electroplating.....	81
4.2	Membrane electroplating process.....	84
4.2.1	Membrane electroplating process design .....	84
4.2.2	Theory .....	84
4.2.3	Experimental electroplating.....	90
4.2.4	Periodic Pulse Reverse current plating .....	95
4.2.5	Electroplating of copper Membranes .....	98
4.2.5	Surface Roughness Analyses on the copper electroplated structure.....	105
4.3	Fabrication of the lower electrodes.....	110
4.3.1	Lower electrode microfabrication process .....	110
5.	Chapter Five: Sensor Release & Tests.....	112
5.1	Sensor releasing process design .....	113
5.2	Etching the copper seed layer.....	114
5.3	Etching the titanium adhesion layer .....	116
5.3.1	Releasing the first sample.....	116
5.3.2	Releasing the second sample.....	119
6.	Chapter Six:Conclusion & Future works.....	123
6.1	Conclusions .....	124
6.2	Future works .....	126
7.	References .....	128

8. Appendix 1 ..... 134

## List of Figures

Figure 1.1: Operating principle of induction probe .....	5
Figure 1.2: Schematic of a conventional field mill [21].....	7
Figure 1.3: Laser deflection measurement system.[22] .....	8
Figure 1.4: Capacitive interrogation system for measurement of membrane deflection [23]. .....	9
Figure 1.5: Schematic view of MEMS field mill of Horenstein et al [24]. .....	10
Figure 1.6: SEM image of MEMS field mill by Yang et al. [25] .....	11
Figure 1.7: The electrostatic field meter chip of [26] .....	11
Figure 1.8: MEFM structure employing thermal actuators .....	12
Figure 2.1: Laser deflection measurement system.[22] .....	16
Figure 2.2: Capacitive interrogation system for measurement of membrane deflection.[23] .....	16
Figure 2.3: Sensor structure.....	17
Figure 2.4: structure of one spring with a quarter of the membrane. ....	18
Figure 2.5:The electrostatic force between two point charges.....	20
Figure 2.6: schematic of Electric field lines.....	21
Figure 2.7: a parallel plate capacitor model. ....	22
Figure 2.8: Schematic of the membrane based electric field sensor by Roncin et al.....	23
Figure 2.9: fixed-free cantilever model.....	24
Figure 2.10: Schematic of the new membrane structure. ....	26
Figure 2.11: Schematic of the spring with beam elements. ....	26
Figure 2.12: Spring-Mass damped system .....	28
Figure 3.1: The meshed model. ....	36
Figure 3.2: Electrical and mechanical applied conditions.....	37
Figure 3.3: The simulation results for the deflection of the membrane .....	39
Figure 3.4: Sensor structure for AC measurement. ....	42
Figure 3.5: Membrane design with 50% duty cycle holes: (a) 40x40 holes. (b) 80x80 holes. ....	44
Figure 3.6: The electrostatic force on different 5 $\mu$ m thick membranes .....	51
Figure 3.7: The electrostatic force on different 10 $\mu$ m thick membranes .....	51
Figure 3.8: The air drag force on the different 5 $\mu$ m thick membranes.....	52
Figure 3.9: The air drag force on the different 10 $\mu$ m thick membranes .....	52
Figure 3.10: Air drag as a percentage of electrostatic force for different membranes.....	56
Figure 3.11: Air drag force as electrostatic force in different frequencies.....	58
Figure 4.1: Schematic of the designed sensor. ....	64
Figure 4.2: Nitride layer photoresist patterning and plasma etching.....	66
Figure 4.3: backside etching in KOH bath .....	66
Figure 4.4: Front side nitride plasma etching and copper metallization .....	67
Figure 4.5: patterning the seed layer with photoresist .....	67
Figure 4.6: Frontside mask for making mold before electroplating of the membranes .....	69
Figure 4.7: 1mm x 1mm Type B membrane with the 40 $\mu$ m x 40 $\mu$ m holes .....	70
Figure 4.8: Anisotropic etching of the Si in the KOH bath .....	71
Figure 4.9: The backside mask for etching the backside holes.....	72

Figure 4.10: Mask for patterning of resistor .....	73
Figure 4.11: Mask for front and back sides patterning, a circle with diameter of three inches ...	74
Figure 4.12: ABM mask aligner optical lithography system.....	75
Figure 4.13: photresist spinner system.....	76
Figure 4.14: plasma etching system.....	76
Figure 4.15: Etched nitride windows .....	77
Figure 4.16: KOH etching setup .....	78
Figure 4.17: Etched holes in the silicon wafer .....	79
Figure 4.18: MRC 8667 sputtering system.....	81
Figure 4.19: Electroplating of the copper into the photoresist mold .....	84
Figure 4.20: The schematic of an electroplating bath for copper plating [37] .....	86
Figure 4.21: The profile of current density between electrodes in the simple electrolytic cell....	87
Figure 4.22: pulsed current waveform and the parameters .....	90
Figure 4.23: Checking the electrical connectivity between sample holder and sample .....	92
Figure 4.24: Electroplating setup .....	93
Figure 4.25: periodic pulse reverse current plating for via filling [33] .....	96
Figure 4.26: periodic pulse reverse current plating waveform .....	97
Figure 4.27: Schematic of the circuit used for dc plating .....	98
Figure 4.28: Electroplated membranes with Thickness of 0.5 $\mu\text{m}$ .....	100
Figure 4.29: Electroplated membranes with Thickness of 2.7 $\mu\text{m}$ .....	101
Figure 4.30: Electroplated membranes with Thickness of 4.02 $\mu\text{m}$ .....	101
Figure 4.31: Large plated particles with thickness of more than 6 $\mu\text{m}$ .....	102
Figure 4.32: Schematic of the circuit used for Pulsed shaped plating.....	103
Figure 4.33: Electroplated membranes with Thickness of 1 $\mu\text{m}$ .....	104
Figure 4.34: Electroplated membranes with Thickness of 2.6 $\mu\text{m}$ .....	104
Figure 4.35: Electroplated membranes with Thickness of 3.3 $\mu\text{m}$ .....	104
Figure 4.36: Electroplated membranes with Thickness of 4.2 $\mu\text{m}$ .....	105
Figure 4.37: Tencor Alpha Step 500 surface profiler, scanning the surface of plated samples ..	106
Figure 4.38: Chosen areas for scanning the thickness of the electroplated copper .....	106
Figure 4.39: Thickness of the electroplated copper over springs and membrane. ....	107
Figure 4.40: Thicknesses of the electroplated copper in different areas .....	107
Figure 4.41: Chosen areas for scanning the thickness of the electroplated copper .....	108
Figure 4.42: Thicknesses of the electroplated copper in different areas .....	108
Figure 4.43: copper sputtering, patterning and etching on top of glass .....	110
Figure 4.44: Fabricated lower electrodes .....	111
Figure 5.1: Etching the seed layer.....	113
Figure 5.2: Releasing the membranes and springs by etching of the silicon.....	113
Figure 5.3: placing the fabricated membranes on top of the electrodes.....	114
Figure 5.4: The electroplated membrane after etching of the seed layer .....	115
Figure 5.5: Sulfurised electroplated copper after the plasma etching.....	118
Figure 5.6: The color change in the electroplated copper during plasma etching with SF <sub>6</sub> .....	120
Figure 5.7: The image of the electroplated membrane after plasma etching.....	121

## List of Tables

Table 3-1: Simulation results for membrane sensor deflection vs. incident electric field. ....	40
Table 3-2: Theoretical expected values for membrane sensor deflection. ....	40
Table 3-3: Total charge at the surface of membrane and lower electrode.....	42
Table 3-4: Total charge at the surface of membrane and lower electrode.. ....	43
Table 3-5: Simulation results for solid membrane with thickness of 5 $\mu\text{m}$ .....	45
Table 3-6: Simulation results for 5 $\mu\text{m}$ thick membranes and 40 $\mu\text{m}$ x40 $\mu\text{m}$ holes.....	46
Table 3-7: Simulation results for 5 $\mu\text{m}$ thick membranes and 80 $\mu\text{m}$ x80 $\mu\text{m}$ holes.....	46
Table 3-8: Simulation results for solid membrane with thickness of 10 $\mu\text{m}$ .....	46
Table 3-9: Simulation results for 5 $\mu\text{m}$ thick membranes and 40 $\mu\text{m}$ x40 $\mu\text{m}$ holes.....	47
Table 3-10: Simulation results for 10 $\mu\text{m}$ thick membranes and 80 $\mu\text{m}$ x80 $\mu\text{m}$ holes .....	47
Table 3-11: Simulation results for solid membrane with thickness of 5 $\mu\text{m}$ .....	49
Table 3-12: Simulation results for 5 $\mu\text{m}$ thick membranes and 40 $\mu\text{m}$ x40 $\mu\text{m}$ holes.....	49
Table 3-13: Simulation results for 5 $\mu\text{m}$ thick membranes and 80 $\mu\text{m}$ x80 $\mu\text{m}$ holes.....	49
Table 3-14: Simulation results for solid membrane with thickness of 10 $\mu\text{m}$ .....	50
Table 3-15: Simulation results for 10 $\mu\text{m}$ thick membranes and 40 $\mu\text{m}$ x40 $\mu\text{m}$ holes .....	50
Table 3-16: Simulation results for 10 $\mu\text{m}$ thick membranes and 80 $\mu\text{m}$ x80 $\mu\text{m}$ holes .....	50
Table 3-17: Simulation results for 5 $\mu\text{m}$ thick membranes .....	53
Table 3-18: Simulation results for 10 $\mu\text{m}$ thick membranes. ....	55
Table 4-1: solution mixture for making one liter of the electrolyte .....	136
Table 4-2: Pulsed current electroplating recipes and results .....	95
Table 4-3: electroplating recipes and results for periodic pulse reverse current plating.....	97
Table 4-4: The Voltage-current characteristics of the electroplating solution.....	99
Table 4-5: Recipes and results for DC plated membranes.....	100
Table 4-6: Recipes and results for pulse plated membranes.....	103
Table 5-1: The recipe for silicon oxide etching, in plasma etching system with CF <sub>4</sub> and O <sub>2</sub> .....	116
Table 5-2: The recipe for silicon etching, in plasma etching system with SF <sub>6</sub> .....	117
Table 5-3: Recipe for Titanium etching, in plasma etching system with CF <sub>4</sub> and oxygen.....	118

# **1. Chapter One**

## **INTRODUCTION**

The goal of this project is designing, modeling and fabrication of a MEMS<sup>1</sup> electric field sensor. This chapter first will review electric field measurement importance and applications and then different instruments and techniques for measuring the electric field will be introduced.

## **1.1 Electric field measurements applications**

Electric field measurement has different applications in our modern world. The range of the applications is wide, and involves atmospheric science, power system applications, electrostatic measurements for controlling and safety purposes in industries, and applications in medical and biological technologies.

The precise measurements of electric field could be used to avoid probable hazards [1-3]. Storing and transportation of electrostatically charged fuels, textile and plastic manufacturing are some examples that the electric field measurement can be used to avoid hazards. In these cases, electric field measurement is used to avoid the uncontrolled electrostatic discharge which can results in explosions [4, 5]. Electric field measurement can also be used to control industrial processes. Electrostatic coating and electro-photography are the instances which electric field measurements are employed to control the processes. [6]

Electric field measurement also can be used for atmospheric studies. Lightning is one of the weather phenomena that can be predicted by electric field measurements. It is possible to predict types of the lightning by measuring the electric field as each type of the lightning has its own electric and magnetic radiation pattern. In addition, location of

---

<sup>1</sup> Micro Electro-Mechanical Systems

the lightning can be predicted, as a high electric field builds up before the lightning hits the ground and electric field measurement can detect it before the lightning actually hits the ground [7-9].

Nowadays, studies on the effect of the high voltage transmission lines on humans is showing a possible association between diseases such as brain cancer and exposure to low frequency electric fields [10-12]. Therefore measuring the electric field under transmission lines and in residential areas is important to investigate more about this probability.

An important role of the electric field measurement is in monitoring and diagnosing the power system equipments. Measurement of the electric fields, by power utilities is common for improving the quality of insulation systems, and increasing the personnel and equipment safety in the live line. Furthermore, it can play a crucial role in detection and diagnosis of the faulty suspension insulators and monitoring of HVDC transformers [13-16].

## **1.2 dc electric field measurement**

Depending on the type of the electric field that we want to measure different techniques should be employed. For the case of ac electric fields, due to the cyclic variations over the time the electric field can be sensed easily. However, for the case of dc electric fields there is no change during the time. Therefore, the measurement technique should be such that instead of sensing the variation of electric field over the time senses a constant value of electric field. This measurement is possible through sensing systems with an initial state, which dc electric field can cause a change in their state and bring them to the

secondary steady state. Thus the deviation from the initial state will be interpreted as the factor for calculating the electric field. This factor could be a change in the capacitance (capacitive sensing), resistance (resistance sensing) or location of the reflected optical signal (electro-optical sensing). Another popular instrument for dc fields is the field mill, in which an alternating electric field is produced by shielding and unshielding the dc electric field in specific period of time. The strength of this alternating field can be used as a factor for measurement of the dc electric field. A brief review on different techniques for dc field measurements is written below. For further studies, referring to [17, 18] is highly recommended.

### **1.3 dc Electric Field Measurement Techniques**

The different instruments for electric field measurement include Electro-optic meters, Induction Probes, Vibrating Field Probes, Electric Field Mills and Micro Machined Electric Field sensors. Below is a brief review on them.

#### **1.3.1 The Electro-optic meter**

The Electro-Optic meter principle of work is based on the change in the optical properties of the materials in the presence of the electromagnetic field. Refractive index of the materials defines the light velocity in that environment. Birefringence is the optical property of some materials having a refractive index that depends on the polarization and propagation direction of light. In the presence of an electromagnetic field, the refractive indexes of birefringent materials in different directions will be changed which results in a change in the orthogonal component of polarization of the light. Equation 1.1 shows the refractive index for each orthogonal component.[19]

$$n = n_0 + aE + bE^2 + \dots \text{ (Higher orders of E)} \quad (1.1)$$

where  $n$  is the refractive index and  $n_0$  is the refractive index in the absence of electromagnetic field.  $E$ ,  $a$  and  $b$  are corresponding to electric field, coefficient of Pockels effect and coefficient of Kerr effect. Higher orders of  $E$  have less effect on the refractive index, therefore can be neglected.

### 1.3.2 Induction Probes

Electrostatic induction is the principle of operation of most of conventional electric field meters. When a conducting plate in contact with ground faces an electric field a net charge will be induced on its surface. The amount of the charge can be calculated using Gauss's law; [19]

$$Q = \epsilon_r \epsilon_0 EA \quad (1.2)$$

where  $A$  is the area of the plate,  $Q$  is the magnitude of the charge and  $E$  is the electric field. Figure 1.1 shows the operating principle of the induction probe.

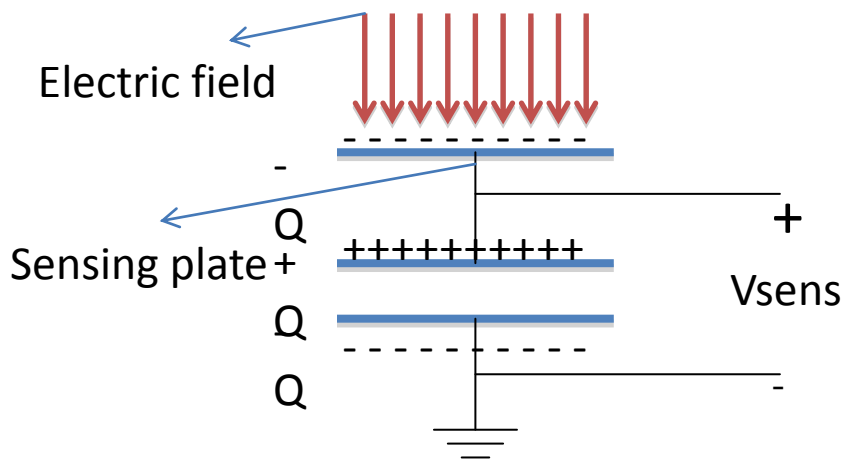


Figure 1.1: Operating principle of induction probe

By connecting the conducting plate to a capacitance which is connected to the ground, if charge  $-Q$  is induced on the plate (sensing plate) due to electric field, the associated displacement current leaves  $+Q$  and  $-Q$  respectively on the upper and lower plates of the capacitor, producing a voltage " $V_{\text{sens}}$ " across the capacitor.  $V_{\text{sens}}$  can be calculated as: [19]

$$V_{\text{sens}} = \frac{Q}{C} = \frac{A\epsilon_0 E}{C} \quad (1.3)$$

where  $E$  is the electric field,  $C$  is the capacitance of the capacitor,  $A$  is the area of the conducting plate.

The disadvantage of these types of electric field sensors is that they can only operate in the charge free environment. Because, the presence of the free charge will cause an error in the measurement of the electric field. This makes the sensor very limited in practice, for example in most power system applications, where ionic corona exists in the environment.

### **1.3.3 Electric Field Mills**

The field mill is designed to solve problems of conventional induction probes. A field mill converts an incident dc field into an alternating field by rotating a grounded chopper above the sensing electrodes. This will solve the charging problem of the sensing electrodes. Previously published research has shown a direct proportion between the peak of the output signal and strength of the electric field [20]. The schematic of structure of a field mill is shown in Figure 1.2. A dc motor is used to rotate the grounded chopper above the sensing plate, and so exposing and shielding the sensing plate repeatedly from

the incident electric field. This results in conversion of the dc field into an alternating field.

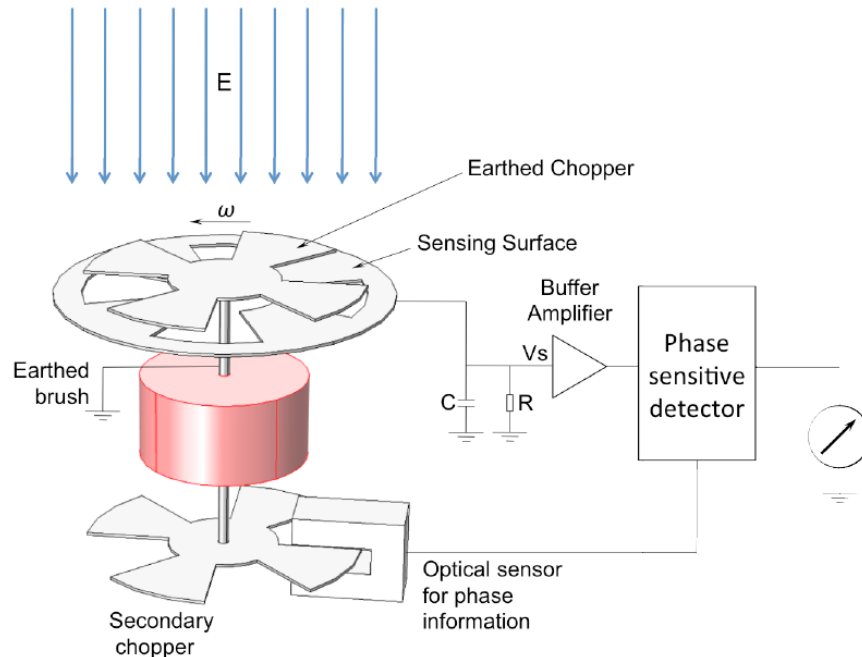


Figure 1.2: Schematic of a conventional field mill [21].

The phase sensitive detector, secondary chopper and optical sensor are used to identify the direction of the incident electric field. High power consumption of the dc motor, size and low lifetime of the device due to mechanical friction are the main disadvantages of using field mills.

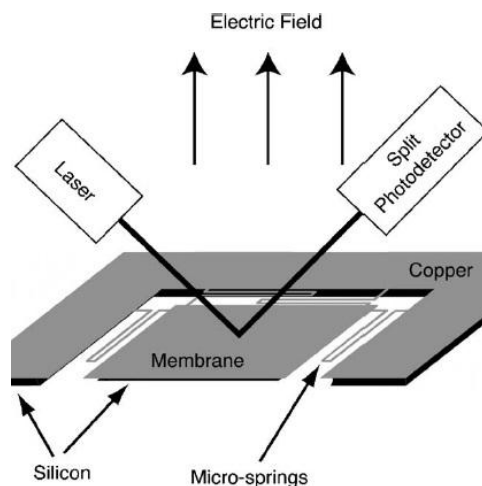
### 1.3.4 Micromachined Electric Field sensors

In order to reduce the power consumption, size, weight and also having the capability of integrating the sensors with electronics, bulky sensors should be replaced with microstructures. Micromachining also offers the mass production, which will reduce the cost. Furthermore, the small feature sensors can be used as a sensor array which will

increase the accuracy of the system. Several micromachined electric field sensors have been developed. Below is a brief review on some of them.

### **Electrostatic force based Micromachined electric field sensors**

In these sensors electrostatic force has been used for deflection of a metalized silicon membrane, which is supported by micro springs. (Figure 1.3). In order to measure the electric field, the deflection of the membrane in the presence of the electric field should be measured. Different techniques can be employed for the deflection measurement. In the first generation of this type of sensors, Roncin et al. [22] employed a laser based position deflection to monitor membrane motion. In the presence of the electric field the membrane will be deflected, and consequently the reflected laser beams motion will be monitored by the detector.



A.Roncin, C.Shafai, and D.R. Swatek, "Electric field sensor using electrostatic force deflection of a micro-spring supported membrane", Sensors and Actuators A, vol. 123-124, pp. 179-184, Sept. 2005

Figure 1.3: Laser deflection measurement system.[22]

In a newer generation, Chen et al. [23], replaced the laser system by a capacitive measurement system. In this system, an adjunct electrode is used to monitor displacement by means of the changing capacitance between the membrane and electrode due to membrane deflection.

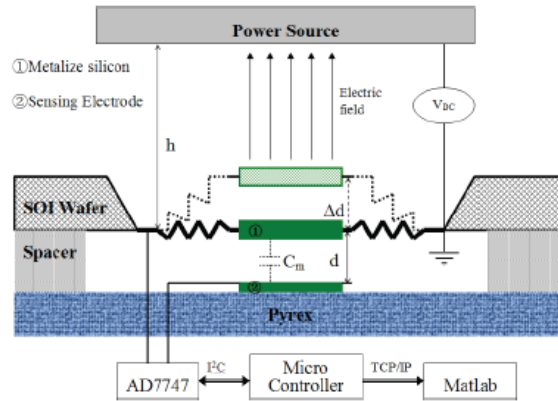


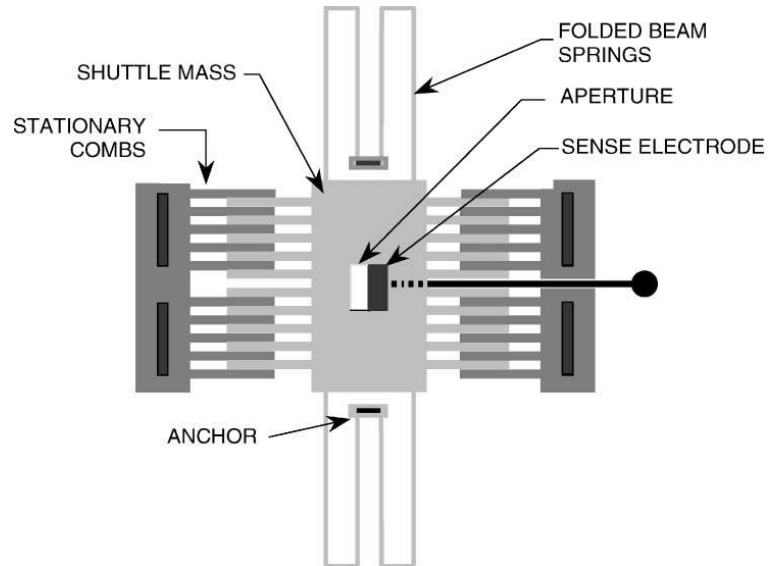
Figure 1.4: Capacitive interrogation system for measurement of membrane deflection [23].

### Micromachined electric field mill (MEFM) using comb drive and thermal actuators

As with conventional field mills, micromachined field mills also have a moving shutter, sensing electrodes and driving system. The difference between the micromachined sensors and the conventional ones is the structure of the shutter. While in the conventional mills the shutter has a rotating structure, in the MEFM the shutter movement is based on a vibration motion because fabrication of a rotating structure in MEMS is very complex. Comb drive and thermal actuators are the systems have been frequently have been used as driving mechanism in the MEFM.

The micromachined field mill developed by Horenstein et al. shown in Figure 1.5 [24], used a comb drive to actuate the shutter. The shutter has a  $10 \times 10 \mu\text{m}$  aperture to expose an electrode measuring  $10 \times 10 \mu\text{m}$  located below the shutter. Their comb drive required

60 V to operate, which can be considered as a disadvantage for the sensor as it will result in higher power consumption compare to the other micromachined sensors.

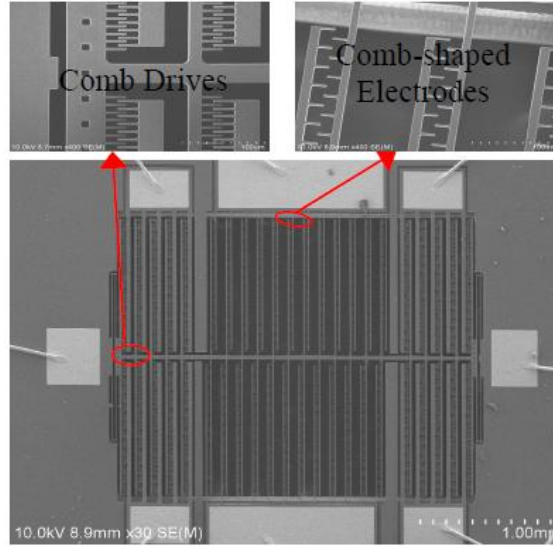


M. N. Horenstein and P. R. Stone, 'A micro-aperture electrostatic field mill based on MEMS technology,' *J. Electrostat.*, May 2001, Vol. 51-52, pp. 515-521

Figure 1.5: Schematic view of MEMS field mill of Horenstein et al [24].

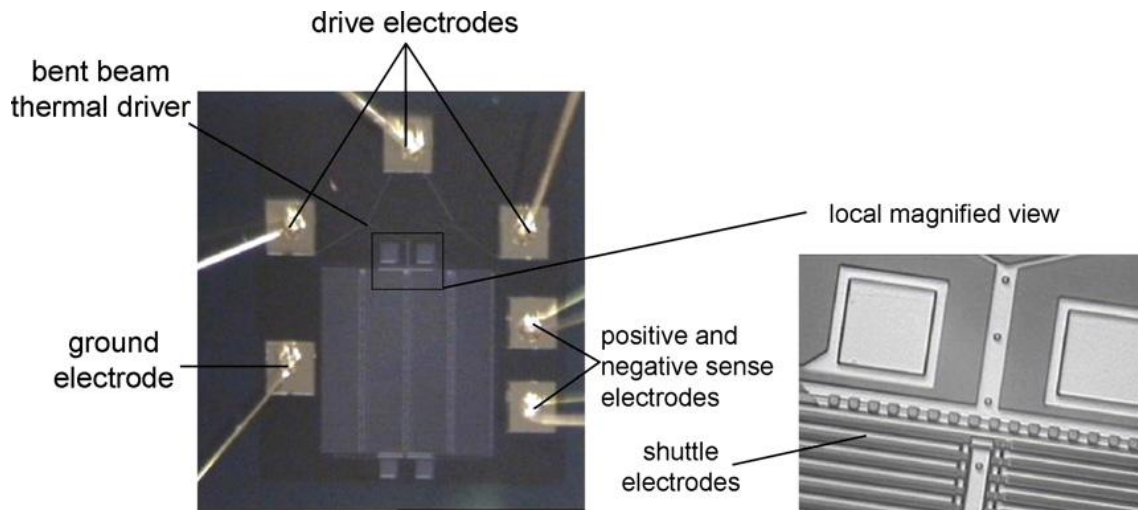
Figure 1.6 shows a MEFM which uses a comb drive system for actuating the shutter, which was developed by Yang et al [25]. A feature of this design is the use of comb electrodes instead of common strip sensing electrodes beneath the shutter.

Figure 1.7 illustrates a MEFM which operates based on a thermal actuating system. [26] This MEFM uses a pair of bent beam thermal actuators as the driving mechanism. In order to improve the total displacement of the shutter the thermal actuators were cascaded.



Pengfei Yang, Chunrong Peng, Haiyan Zhang, Shiguo Liu, Dongming Fang, and Shanhong Xia, 'A high sensitivity SOI electric-field sensor with novel combshaped microelectrodes', 16th International Solid-State Sensors, Actuators and Microsystems Conference, 5-9 Jun. 2011, pp. 1034-1037

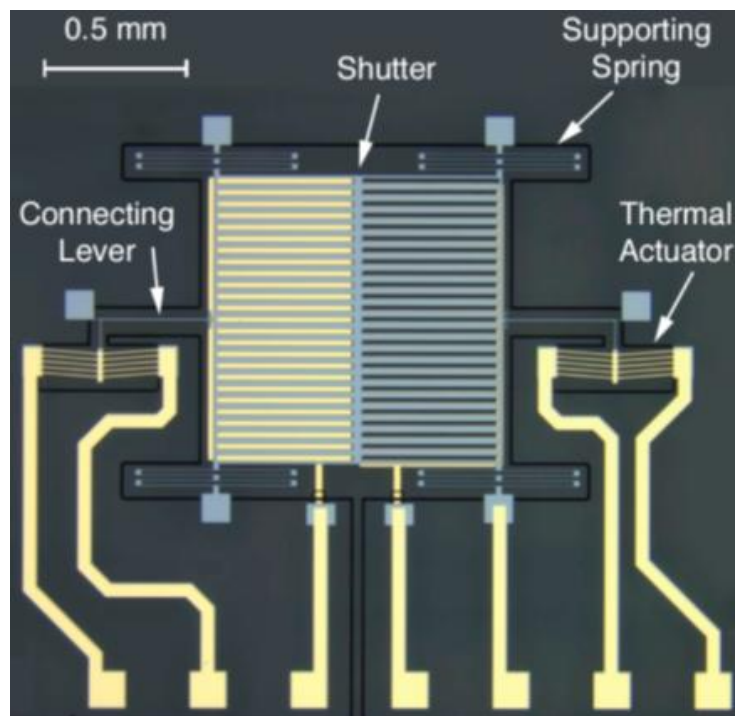
Figure 1.6: SEM image of MEMS field mill by Yang et al. [25]



Xianxiang Chen, Chunrong Peng, Hu Tao, Chao Ye, Qiang Bai, Shaofeng Chen, and Shanhong Xia, 'Thermally driven microelectrostatic fieldmeter', Sensors and Actuators A: Physical. 20Nov. 2006. Vol. 132. Issue 2. pp. 677-682.

Figure 1.7: The electrostatic field meter chip of [26]

Another MEFM structure employing thermal actuators has been fabricated by Wijeweera et al. in our group (Figure 1.8) [27]. It has a silicon shutter with the area of 1mm x 1mm. Two arrays of gold electrodes are patterned at the bottom of an etched hole under the shutter such that a 10  $\mu\text{m}$  gap stands between the shutter and electrodes. The shutter is suspended by four sets of springs (one at each corner), and is actuated by two thermal actuators with a lever system to amplify the displacement. A differential sensing method is employed in this sensor, such that at each time one of the electrodes is shielded by the shutter the other one is exposed to the electric field. Therefore, this sensor does not require any ground reference.



Gayan Wijeweera, Behraad Bahreyni, Cyrus Shafai, and Athula Rajapakse, "Micromachined electric-field sensor to measure AC and DC fields in power systems", IEEE Trans. Power Delivery, vol. 24, pp. 988-995 July 2009

Figure 1.8: MEFM structure employing thermal actuators has been fabricated by Wijeweera et al. [27]

## **1.4 MEMS electric field sensor of this thesis and project objectives**

Due to the high power consumption of conventional field mills there is an interest for using low power devices such as micro machined electric field sensors. Each micromachined device for electric field measurement has its own advantage. For instance the electrostatic force membrane based devices can operate for measurement of both dc and ac electric fields. In addition, the range of sensitivity that they work in ac mode is reported as the most sensitive device among the micromachined electric field devices. However, they are not as sensitive as micromachined field mill devices for the case of the dc fields [21]. Since our group has already developed a version of the electrostatic force membrane based sensor and got acceptable results out of that, we want to improve the design. The problem with the first laser interrogated design was the large power consumption of the laser system as well as the large size of the laser system which was almost shadowing the miniature size of the MEMS device. This made the whole system very bulky and immobile (see Figure 2.3). Therefore a subsequent version of the sensor was designed to use capacitive interrogation and the first generation of the sensor has been successfully fabricated in an SOI wafer process, and tested. However, the SOI wafers are expensive, therefore, in order to reduce the cost of fabrication, electroplating of low stress metals instead of SOI wafer could be an alternative. The other benefits of electroplated thick films (copper or nickel) are their robustness. Therefore, the purpose of this project is designing the next generation of our sensors with electroplated copper. Also we will try to improve the operation of the device under ac fields by solving the air damping problem by modifying the structure of the membrane.

## **2. Chapter Two**

### **Theory**

## 2.1 Introduction

As mentioned in the chapter one, Field mills are conventional devices for measuring dc electric fields, however due to their high power consumption, there is an interest for using low power devices such as micro machined electric field mills (MEFMs) instead. Our group has explored electrostatic force deflected membrane based sensors. Roncin et al. implemented a laser deflection measurement system (Figure 2.1) for measuring the deflection of the membrane. The problem with the laser system was large power consumption; therefore a subsequent version of the sensor was designed to use capacitive interrogation of the deflected membrane position (Figure 2.2) [23]. The metalized membrane will be deflected to the voltage source due to the electrostatic force and the deflection will result in the change of the capacitance between membrane and the electrode beneath. The change in the capacitance  $C_m$  is measured with a capacitance to digital convertor chip and sent to the computer for post processing. The first generation of the sensor has been successfully fabricated in an SOI wafer process, and tested. However, the SOI wafers are expensive, therefore, in order to reduce the cost of fabrication electroplating of the low stress thick metals instead of SOI wafer could be an alternative. The other benefits of electroplated thick films (copper or nickel) are their robustness. Therefore the purpose of this project is designing the next generation of our sensors with electroplated copper.

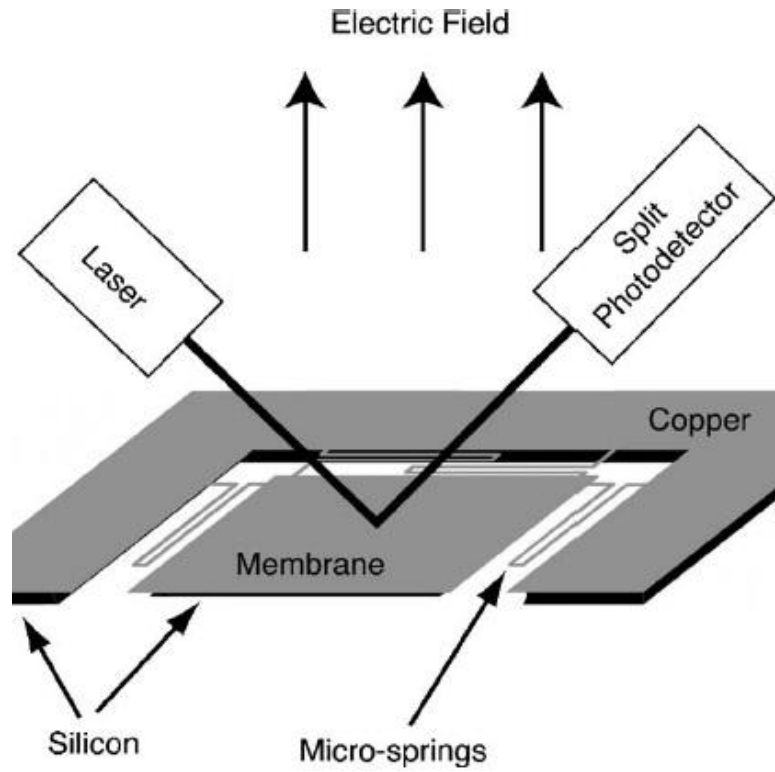


Figure 2.1: Laser deflection measurement system.[22]

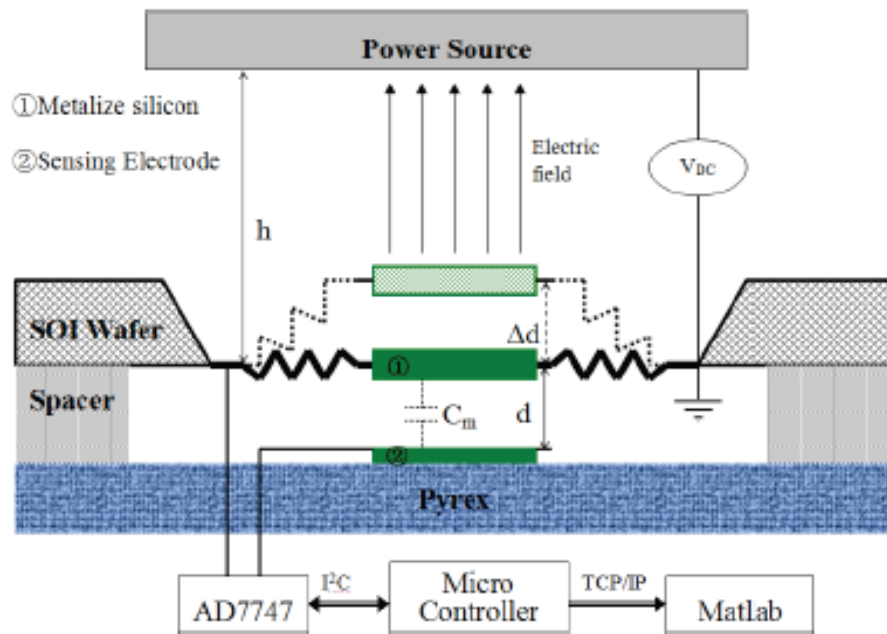


Figure 2.2: Capacitive interrogation system for measurement of membrane deflection.[23]

## 2.2 Sensor Design and Operation Principle

### 2.2.1 Design

The sensor consists of a membrane that is suspended by the four springs (Figure 4.3). The membrane measures 1 mm x 1 mm and the springs are 30  $\mu\text{m}$  wide with width of 470  $\mu\text{m}$ . The whole membrane structure and springs are made of copper, and the ends of the springs are fixed by connecting to a copper substrate. The thickness range of 5 to 10  $\mu\text{m}$  has been chosen in the initial design for membrane and springs. These thicknesses are chosen to result in a robust and flexible membrane at the same time.

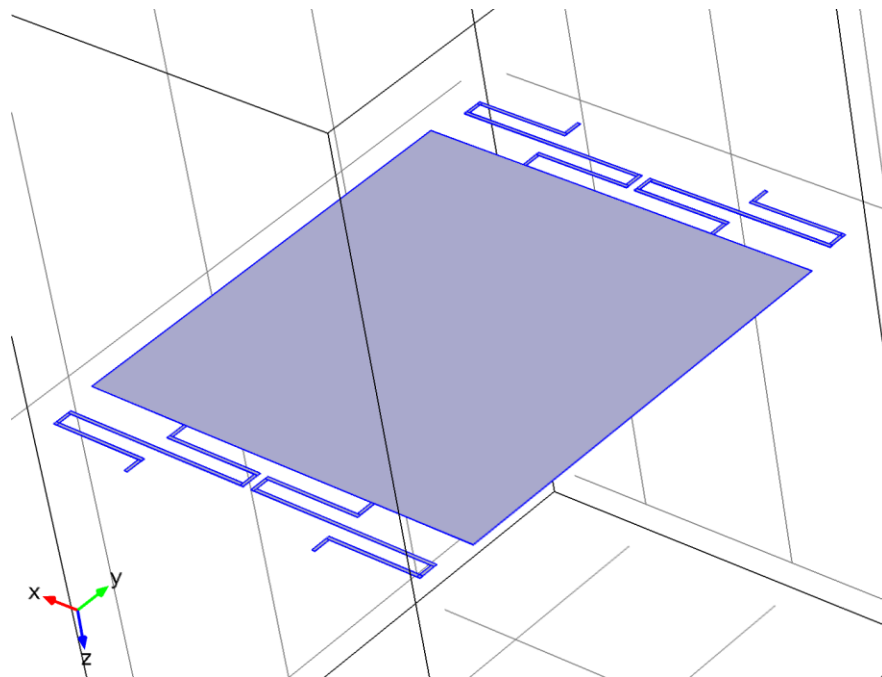


Figure 2.3: Sensor structure.

Figure 2.4 is showing the size and structure of one spring with a quarter of the membrane.

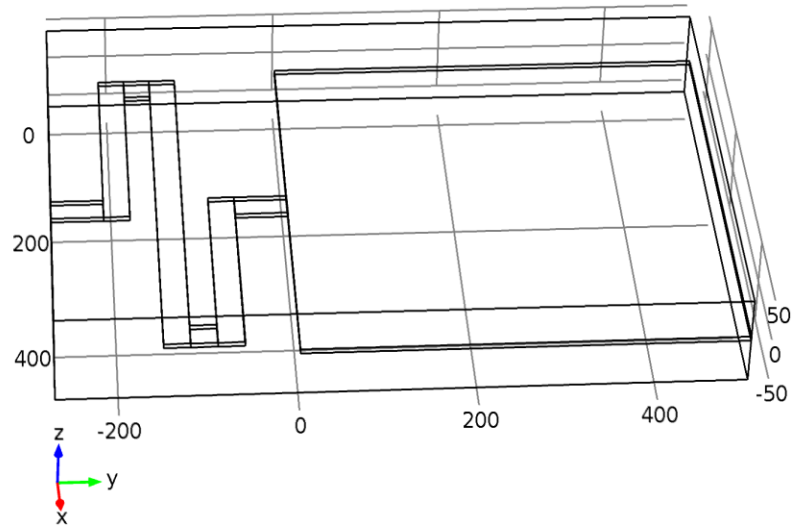


Figure 2.4: structure of one spring with a quarter of the membrane.

### 2.2.2 Operation Principle

The incident electric field will cause an electrostatic force which will pull the membrane toward the voltage source. [23]

$$F = \frac{1}{2} \frac{\epsilon A}{h^2} V_{DC}^2 = \frac{1}{2} \epsilon A E^2 \quad \text{N} \quad (2.1)$$

where A is the surface area of the membrane, V is the voltage of the voltage source,  $\epsilon$  is  $\epsilon_r \epsilon_0$ , where  $\epsilon_r$  is relative dielectric constant and  $\epsilon_0$  is permittivity of the free space, E is the electric field and h is the distance between membrane and voltage source. The restoring force on the springs is given by: [23]

$$F_s = k \Delta d \quad (2.2)$$

where k is the spring constant (total of the four micro-springs supporting the membrane).

The relationship between the incident electric field that causes membrane motion, and the

variation of the capacitance measured by the position sensing electrode (derived by Chen et al. [23]), is:

$$\Delta C = \frac{C_{m\text{ initial}}^2}{\frac{2k}{E^2} + C_{m\text{ initial}}} \quad (2.3)$$

Where,  $\Delta C = C_{m\text{ initial}} - C_{m\text{ final}}$  . ( $C_m$  is the capacitance between membrane and lower electrode)

This chapter will review on the background theory needed. The required background theory of this thesis can be divided into two parts; electrostatic theory and mechanical theory.

### **2.3 Electrostatic theory**

Based on Coulomb's law the magnitude of the electrostatic force between two point charges is proportional to the product of the magnitudes of the charges and inversely proportional to the square of the distance between them. In equation 2.4, F stands for the electrostatic force between the point charges;  $q_1$  and  $q_2$  are the electric charge of the two points.  $\epsilon_0$  is the permittivity of the free space,  $\epsilon_r$  is the relative permittivity of the space where two charges are locating at, and r is the distance between the two charges. [19]

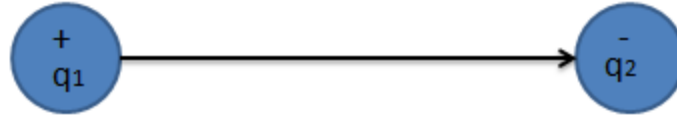


Figure 2.5: The electrostatic force between two point charges.

$$F = \frac{q_1 q_2}{4\pi\epsilon_r\epsilon_0 r^2} \text{ N} \quad (2.4)$$

$$\epsilon_0 = \frac{1}{4\pi} 10^{-9} = 8.85 \times 10^{-12} \text{ F/m} \quad (2.5)$$

The electric field strength is a vector of quantity which has both magnitude and direction. The magnitude of the electric field strength is defined in terms of how it is measured. The strength of the source charge's electric field could be measured by any other charge placed somewhere in its surroundings. Let call the charge that is used to measure the electric field a test charge. When a test charge  $q$  is placed within the electric field, it will experience an electric force. From equation 2.4, and assuming that  $q_1$  is the source charge and the  $q_2$  is the test charge we can rewrite equation 2.4 as: ( $a_r$  is the unit vector in direction of  $q_1$  to  $q_2$ ) [19]

$$E = \frac{F}{q_2} = \frac{q_1}{4\pi\epsilon_r\epsilon_0 r^2} a_r \quad \text{N/C} \quad (2.6)$$

Electric field lines are useful for visualizing the electric field. Field lines begin on positive charge and terminate on negative charge, and are parallel to the direction of the electric field. The mechanical work energy which is required to move a charge,  $Q$ , along the electric fields lines from point a to b, can be calculated as below: [19]

$$W_{ab} = -Q \int_a^b E \cdot dL \quad \text{J} \quad (2.7)$$

where  $E \cdot dL$  is the dot product of the electric field and an incremental distance of  $a$  to  $b$  along the path.

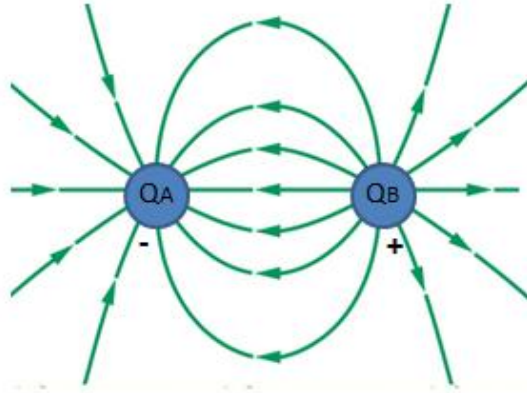


Figure 2.6: schematic of Electric field lines.

The work which is required to bring a unit charge from infinity to its current location is called Potential energy, the voltage difference between two points ( $a, b$ ) can be calculated from equation below:[19]

$$V_{ab} = -\int_a^b E \cdot dL \quad \text{V} \quad (2.8)$$

For a charge distribution instead of point charge, we can say:[19]

$$E = -\nabla V \quad \text{V/m} \quad (2.9)$$

Also  $W_e$  will be the required work for creating the charge distribution: [19]

$$W_e = \frac{1}{2} \int_{\text{vol}} (D \cdot E) dv = \frac{1}{2} \int_{\text{vol}} \epsilon E^2 dv \quad \text{V} \quad (2.10)$$

where  $E$  is the electric field vector in the domain and  $D$  is electric displacement field ( $D = \epsilon_r \epsilon_0 E$ , where  $\epsilon_r$  is relative dielectric constant and  $\epsilon_0$  is permittivity of the free space).

The force that an electric field applies to a charged body in its domain can be calculated as the negative gradient of its work energy. From this, the magnitude of the electric field can be determined by force based measurement techniques. [19]

$$F = -\nabla W_e \quad N \quad (2.11)$$

By neglecting the fringing effect, the system can be modeled as a parallel plate capacitor. By calculating the stored energy in a capacitor, equation 2.11 can be simplified and an equation for the relationship between field to force can be formed (equation 2.14).

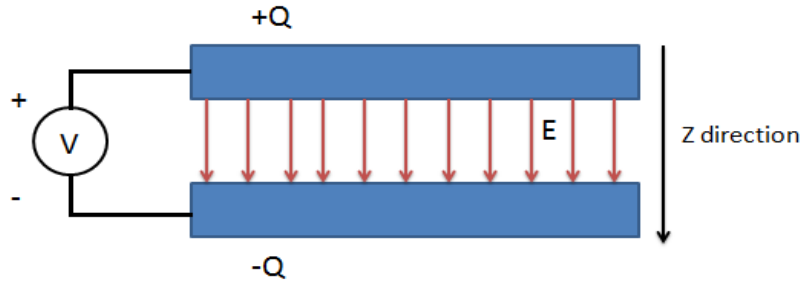


Figure 2.7: a parallel plate capacitor model.

The energy stored in a capacitive system is given as:

$$W_e = \frac{1}{2} CV^2 = \frac{1}{2} \frac{\epsilon A}{z} (E_z z)^2 = \frac{1}{2} \epsilon A E_z^2 z \quad (2.12)$$

By assuming having a uniform electric field in the  $z$  direction, and expanding out equation 2.9 the electric field in the  $Z$  direction will be: ( $a_x$ ,  $a_y$  and  $a_z$  are the unit vectors for  $x, y$  and  $z$  direction in cartesian coordinates)

$$F = -\nabla W_e = -\frac{\partial W_e}{\partial x} a_x - \frac{\partial W_e}{\partial y} a_y - \frac{\partial W_e}{\partial z} a_z \quad \text{N} \quad (2.13)$$

Which can be written as:

$$F = -\nabla W_e = 0 a_x - 0 a_y - \frac{\partial(\frac{1}{2}\epsilon A E_z^2 Z)}{\partial z} a_z \quad \text{N}$$

$$F_z = \frac{1}{2} \epsilon A E_z^2 Z \quad \text{N} \quad (2.14)$$

where  $F_z$  is the force between two charged bodies.

## 2.4 Mechanical Theory

The first membrane based electric field sensor in our group was designed by Roncin et al.

[21] Figure 2.8.a shows the sensor structure:

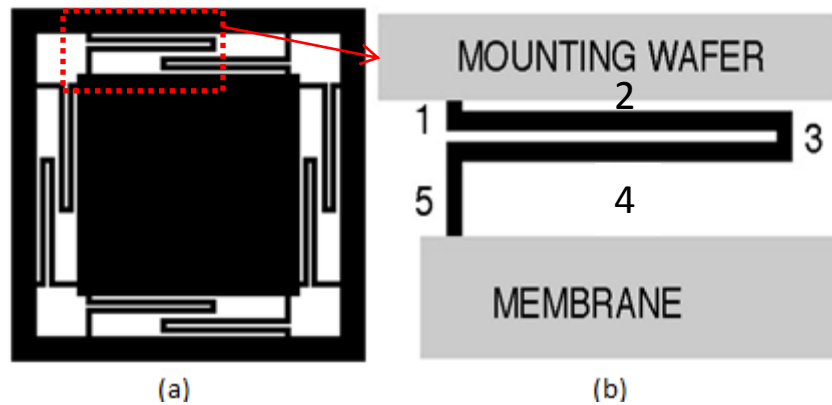


Figure 2.8: Schematic of the membrane based electric field sensor by Roncin et al. a: sensor schematic. b: membrane structure. [22]

As shown in Figure 2.8a, the sensor consists of a membrane which is connected by 8 ribbons to the wafer. In MEMS technology these ribbons are modeled to act like a spring. For predicting the behavior of the membrane deflection, first the spring's constant should be approximated. In order to approximate the behavior of the springs, the geometry of

the springs should be divided into small beams and then by simplifying the structure with the parallel and series relationship between the small beams, the total spring behavior can be approximated. For the sensor of Figure 2.8 we can simplify the geometry by assuming the membrane is held up by two springs (2 and 4 in Figure 2.8.b) on each corner, resulting in 8 parallel beams. Considering the symmetry in spring structure it can be assumed that there is symmetry in the lateral forces on the membrane. Therefore, for each spring we can assume to have two parallel cantilever beams (One side is fixed and one side is free to move). Figure 2.9 shows a fixed-free cantilever model.

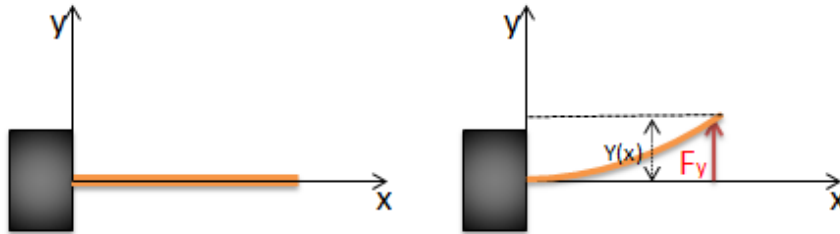


Figure 2.9: fixed-free cantilever model

equation 2.15 is showing the movement of this type of beams[28]:

$$Y(x) = \frac{F_y}{6E_{young's}I}(3x^2L-x^3) \quad m \quad (2.15)$$

where  $Y(x)$  = vertical deflection,  $F_y$  = y directed applied force,  $L$  = total beam length.  $E_{Young's}$ =Young's modulus,  $x$  = distance from the fixed. The moment of inertia for a beam with rectangular cross-section is given by: [28]

$$I = \frac{1}{12} wt^3 \quad m^4 \quad (2.16)$$

Where,  $w$ = width of the beam,  $I$  = moment of inertia and end and  $t$  = thickness of the beam. By assuming to have a uniform electrostatic force along the cantilever, the

maximum deflection of cantilever can be calculated at the end of the cantilever ( $x=L$ ), equation 2.17 as:

$$Y(x=L) = \frac{12F}{6E_{young's} wt^3}(2L^3) = \frac{4FL^3}{E_{young's} wt^3} \quad m \quad (2.17)$$

Therefore the force can be written as:

$$F(x=L) = \frac{E_{young's} wt^3 Y}{4L^3} \quad (2.18)$$

The use of two equal cantilever beams results in the curvature and deflection of each beam to canceling each other. Therefore, the fixed and guided endpoints of the spring will remain in the same plane. Since the midpoint is free to move, we assume that have a series fixed-free cantilever. The equation can be rewritten as:

$$Y(x, 2 \text{ beams in series}) = 2 \times \frac{F_y}{6E_{young's} I}(3x^2L-x^3) \quad m \quad (2.19)$$

The eight springs in all the corners are in parallel with each other. Therefore the complete structure can be considered as eight parallel springs with two beams on each, and so the equation can be written as:

$$Y(x, 8 \text{ springs}) = \frac{2}{8} \times \frac{F_y}{6E_{young's} I}(3x^2L-x^3) \quad m \quad (2.20)$$

We can conclude that the theoretical model for spring force of the system can be written as:

$$F_m = -kz = \left( \frac{\text{Number of springs in parrallel}}{\text{Number of the beams in series}} \times \frac{1}{4} \frac{E_{young's} wt^3}{6E_{young's} I} \right) za_z \quad N \quad (2.21)$$

where  $F_m$  is the mechanical restoring force of the spring.

In the design of this thesis, shown in Figure 2.10, the membrane is attached to the silicon wafer with four ribbons which are working as springs during the deflection process. If we break each spring from the center into two parts we can assume two springs in series. (Figure 2.11) Then each of these springs (the half of original spring) will have four parts; two main parts (Beam 2 and 4 in Figure 3.11) and two short segments for the connection (Beam 1 and 3 in Figure 2.11). We can assume that the two main beams (2,4) are in series and neglect the short connection segments to simplify our model, by making all the assumptions that already have been mentioned for beam 2 and 4 in the older design.

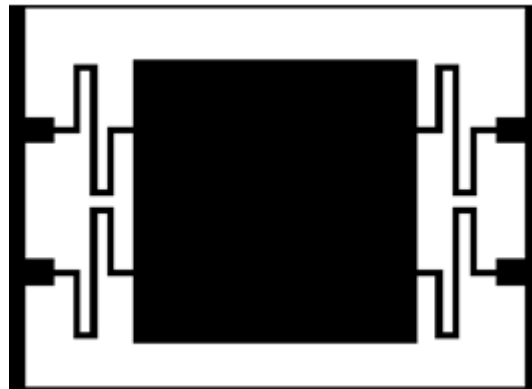


Figure 2.10: Schematic of the new membrane structure.

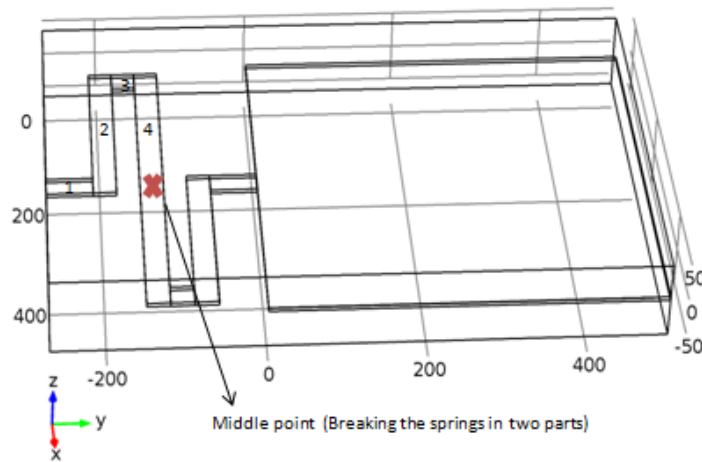


Figure 2.11: Schematic of the spring with beam elements.

Therefore for each half we have two beams in series and we have:

$$Y(x, 2 \text{ beams in series}) = 2 \times \frac{F_y}{6E_{young's} I} (3x^2L - x^3) \text{ m} \quad (2.22)$$

For a complete spring we have two springs (considering each half as one spring) in series:

$$Y(x, 2 \text{ springs in series}) = 2 \times 2 \times \frac{F_y}{6E_{young's} I} (3x^2L - x^3) \text{ m} \quad (2.23)$$

By assuming the four springs that are supporting the membrane are in parallel, we will obtain:

$$Y(x, 4 \text{ springs}) = \frac{4}{4} \times \frac{F_y}{6E_{young's} I} (3x^2L - x^3) \text{ m} \quad (2.24)$$

If we solve the equation above at  $x=L$ , then we will have obtain:

$$Y(x=L, 4 \text{ springs}) = \frac{4}{4} \times \frac{F_y}{6E_{young's} I} (3x^2L - x^3) \text{ m} = \frac{12F}{6E_{young's} wt^3} (2L^3) = \frac{4FL^3}{E_{young's} wt^3} \quad (2.25)$$

Equation 2.25 shows that the maximum deflection (the deflection at the end of the cantilevers,  $X=L$ ) of the springs (the equivalent model for all of the springs together) is proportional to the cube of the spring's length, inversely proportional to the spring's width, inversely proportional to the cube of the spring's thickness. In the next chapter the behavior of the springs and deflection of membrane in the presence of the electric field will be modeled in COMSOL finite element software for different electric fields to see if the simulation results agree the presented models in this chapter for the exerted electrostatic force on the membrane and the spring's deflection behavior.

## 2.5 Spring-Mass system

Before starting the modeling and simulation it is necessary to have a review on the theory of spring-mass damped systems, since our system is a mass-spring damped system. The structure of a spring-mass damped system is shown in Figure 2.12.

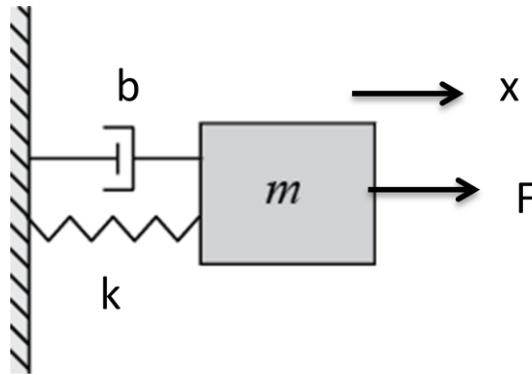


Figure 2.12: Spring-Mass damped system

At equilibrium the relation between the applied force to the spring and its movement is governed by Hooke's law [29];

$$F=kx \quad (2.26)$$

where  $F$  is the applied force and  $k$  is the spring constant. However, during the motion of the springs, the movement of system is governed by a second order linear differential equation with constant coefficients shown below [29];

$$F(t) = kx(t) + b \frac{dx}{dt} + m \frac{d^2x}{dt^2} \quad (2.27)$$

where  $F(t)$  is the net force,  $k$  is the spring constant,  $b$  is the damping coefficient and  $m$  is the mass of the system. For the case that the  $b$  is zero, there is no damping and the spring will oscillate by its natural frequency which is calculated as below [29]:

$$\omega_0 = \sqrt{\frac{k}{m}} \quad (2.28)$$

where  $\omega_0$  is the natural frequency,  $k$  is the spring constant,  $m$  is the mass of the system. For the case that  $b$  is not zero, the motion is no longer an oscillation with natural frequency.

For the case that the driving force,  $F$ , is a sinusoidal force, the equation will be like:[29]

$$F_0 \sin(\omega t) = kx(t) + b \frac{dx}{dt} + m \frac{d^2x}{dt^2} \quad (2.29)$$

The solution for movement of the structure in this case is a superposition of transient and steady state behavior. Depending on the system parameters, the transient motion will fall into one of these three categories:

- 1- Over damped
- 2- Under damped
- 3- Critically damped

The steady state behavior of the system is following the equation below [29]:

$$x(t) = \frac{F_0}{mZ_m\omega} \sin(\omega t + \phi) \quad (2.30)$$

where  $Z_m$  is: ( $\omega_0$  is the natural frequency of the system)

$$Z_m = \sqrt{(2\omega_0\zeta)^2 + \frac{1}{\omega^2}(\omega^2 - \omega_0^2)^2} \quad (2.31)$$

$$\phi = \arctan\left(\frac{2\omega_0\omega\zeta}{\omega^2 - \omega_0^2}\right) \quad (2.32)$$

$$\zeta = \frac{b}{2\sqrt{mk}} \quad (2.33)$$

For a specific frequency called resonance frequency,  $\omega_r = \omega_0\sqrt{1 - 2\zeta^2}$ , the displacement amplitude can get to high values for the case that the system is strongly under damped. We want to avoid the operation of our sensor under this condition, because the amplitude of the deflection for this case is higher than the deflection values for the same dc field in the equilibrium condition and the measurement will not be valid. Therefore the ac measured signals should have significantly lower frequencies than the resonance frequency.

### 2.5.1 Over damped

For the case that  $\zeta > 1$ , displacement function is called over damped.[29]. We want our designed sensor to operate in this mode, because during the measurement of the ac fields we want the maximum deflection of the membrane be the same as the deflection of membrane under dc field at the equilibrium state. To gain such a behavior it is necessary to operate much below the system natural resonant frequency.

### 2.5.2 Under damped

For the case that  $\zeta < 1$ , the system's displacement function is called under damped. [29]

For the case of significantly under damped systems ( $\zeta < 1/\sqrt{2}$ ), the amplitude of the

deflection for a given force,  $F_0$ , for the driving frequencies close to the resonance frequency will reach high values. We do not want our system to operate in this condition.

### **2.5.3 Critically damped**

For the case that  $\zeta = 1$ , the system's displacement function is called critically damped. [29] For the critically damped system, the system does not have a high deflection values for the frequencies close to the resonance frequency.

### **2.5.4 Mode of damping for the designed sensor of this project**

As already mentioned, we want our designed sensor to operate such that during the measurement of the ac fields, the maximum deflection of the membrane be approximately the same as the deflection of membrane under dc fields at the equilibrium state, and the membrane movement behaves similar to the movement under dc fields. Let have a look at our second order differential equation (2.27) and comparing it with Hooke's law (2.26), there are two terms which make the difference between the equilibrium static states of Hooke's law and the inertial damped motion in differential equation,  $b\dot{x}$  and  $m\ddot{x}$ . By reducing the effects of these two terms the membrane motion under ac fields will be much closer to the movement under dc fields and will be governed by the  $kx$  term. For the second term,  $b\dot{x}$ , the air damping effect will be studied in chapter three, section 3.3. It will be shown that the air damping force is small compared to the electrostatic force which will cause the membrane motion. Also by making a new design this value could be reduced to less than 1% of the electrostatic force. For the  $m\ddot{x}$  term, in section 3.5, by calculating the resonance frequency of the system for different designs it will be shown that the frequency of the ac measured signals are much lower than the

resonance frequency of the structure. This means that the motion of the structure is very slow when compared with the resonance frequency and the term  $m\ddot{x}$  which is proportional with the second derivative of the membrane motion is very small and can be neglected.

# **3. Chapter Three**

## **Sensor Modeling & Simulations**

In this chapter a model for our MEMS based electrostatic field sensor is presented. Then deflection of the sensor is calculated both by simulation and theoretical. Two sets of simulations have been done with 5  $\mu\text{m}$  and 10  $\mu\text{m}$  as the thickness of the membrane and springs. These thicknesses are chosen to have a robust and flexible membrane at the same time. In the first design and simulations we are using the membrane with these thicknesses, however after the first design and fabrication has been done successfully, the next project could be optimizing the membrane thickness to get the best deflection range and lowest stress. Simulation models will also be designed to solve the vibrating issue of the membrane for measuring the ac electric fields and see if by adding perforations to the surface of the membrane, it is possible to reduce the mass of membrane and still have similar electrostatic force on the membrane and consequently reduce the damping due to air resistance in membrane movement during measurement of ac electric fields.

### **3.1 Use of COMSOL Multiphysics**

By using symmetry, only a quarter of the sensor has been simulated in order to save time and memory. The electromechanics interface is used for defining mechanical and electrical conditions of the model, which is solving the coupled equations for the structural deformation and the electric field [30]. A box of air is surrounding the sensor in the model and an electrical potential is applied to the top boundary of the air box while the springs, membrane and bottom boundary of the box are electrically grounded. The end of each spring is defined as a fixed constraint while the rest of the structure is free to move. An electrostatic force caused by an applied potential to the top boundary deflects the springs and membrane toward the grounded boundary beneath it. To compute the electrostatic force, this model calculates the electric field in the surrounding air. As the

Membrane and springs being deflected, the geometry of the air gap changes, resulting in a change in the electric field. The coupled physics is handled automatically by the Electro mechanics interface.

The electrostatic field in the air and in sensor is governed by Poisson's equation [30]:

$$-\nabla \cdot (\epsilon \nabla V) = 0 \quad (3.1)$$

where derivatives are taken with respect to the spatial coordinates. The numerical model represents the electric potential and its derivatives on a mesh, which is moving with respect to the spatial frame. The necessary transformations are taken care of by the Electromechanics interface, which also contains smoothing equations governing the movement of the mesh in the air domain.

The force density that acts on the membrane and spring's beam results from Maxwell's stress tensor [30]:

$$F_A = -\frac{1}{2}(E \cdot D)n + (n \cdot E)D \quad (3.2)$$

where E and D are the electric field and electric displacement vectors, respectively, and n is the outward normal vector of the boundary. This force is always oriented along the normal of the boundary.

Both of the above equations will be solved in COMSOL by using FEM<sup>2</sup> models. One important issue is the number of meshes which determines the accuracy of the model. For

---

<sup>2</sup> Finite Element Method

the solution to be valid, a minimum number of meshes are required. To find the minimum number of meshes, we can start from a low number of mesh elements and calculate the solution, then gradually make the mesh finer and check the solution. If the solution does not change significantly after several trials then the last trial can be considered as a good final solution.

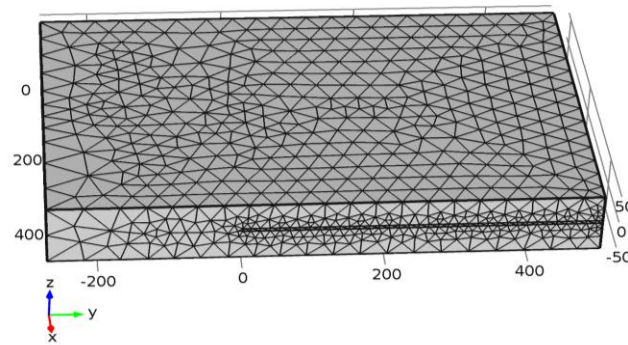


Figure 3.1: The meshed model.

As shown in Figure 3.1, the mesh structure consists of different geometries with different resolutions. The areas close to the membrane and on the surface of membrane are defined with extra fine mesh structure while for the rest of the model just fine meshing structure has been used. Below is the detail on the meshed structure extracted from the COMSOL software:

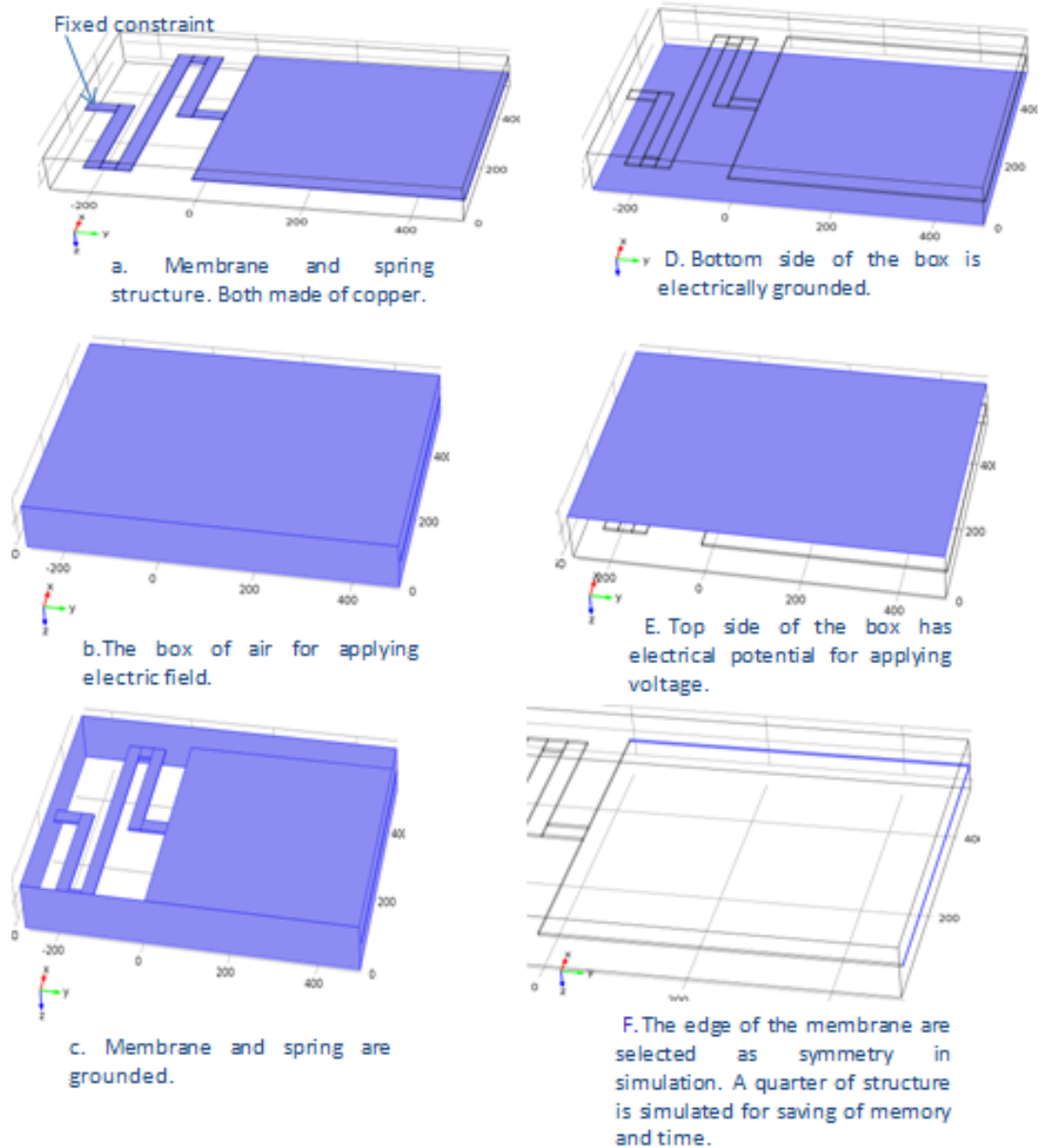


Figure 3.2: Electrical and mechanical applied conditions

Table 3-1: Detail of the meshed structure [30]

Name	Value
Maximum element size	77 $\mu\text{m}$
Minimum element size	1.39 $\mu\text{m}$
Resolution of curvature	0.6
Resolution of narrow regions	0.5
Maximum element growth rate	1.5

Table 3-2 is showing the copper parameters that COMSOL uses for running the simulations.[30]

Table 3-2: Copper parameters

Name	Value	Unit
Density	8700	kg/m <sup>3</sup>
Young's modulus	110*10 <sup>9</sup>	Pa
Poisson's ratio	0.35	1

## 3.2 Simulations and Results

### 3.2.1 Membrane deflection under DC field

The previous version of the sensor [31] was a silicon based membrane which was 5  $\mu\text{m}$  thick and had 200 nm sputtered copper surface coating. Since the membrane of this project will be made entirely from copper, the first set of simulations should be done to check the range of the deflection of membrane, in order to see whether the new design have enough deflection range to be sensed with the capacitance interrogation system. Second, the model should determine if results agree with theoretical expected values based on equation 3.2. Due to the limitation in fabrication process and need for enough strength in the membrane, copper thicknesses between 2 - 10  $\mu\text{m}$  are investigated. The results for the deflection of the membrane for different electric fields for thickness of 5 $\mu\text{m}$  and 10 $\mu\text{m}$  are shown in Table 3-3. In Table 3-4 the expected deflection values based on the theoretical formula from chapter two (equation 2.14 for calculating the

electrostatic force and equation 2.25 for calculating the spring constant) are shown (The same value of the Young's modulus from the simulation parameter, Table 3-2, was used for spring constant calculation,  $110 \times 10^9$  Pa). Comparing tables 3-3 and 3-4, we can see that the deflections for both theoretical and simulations agree, with the range of the deflections closely in the same order. Also, the range of the deflection of membrane is large enough to be create the capacitance change in range of femtofarads (for the lowest deflections) which can be detected by our capacitance convertor chip (AD7747) [32].

By referring to equation 2.25, it can be seen that the deflection of the membrane depends on the spring's thickness, width and length. Since the only parameter that is changing between two sets of simulations is the spring's thickness and the deflection of the springs is inversely proportional to the cube of the spring's thickness, we expect to get eight times lower deflection values for  $10\mu\text{m}$  thick membranes where compared to  $5\mu\text{m}$  thick membranes. By a simple calculation on values of the Table 3-3 and 3-4 between  $5\mu\text{m}$  and  $10\mu\text{m}$  thick membranes it can be conferred that the ratio between the deflections for the theoretical model is 8 times, this ratio for the simulated result have values close to 8.

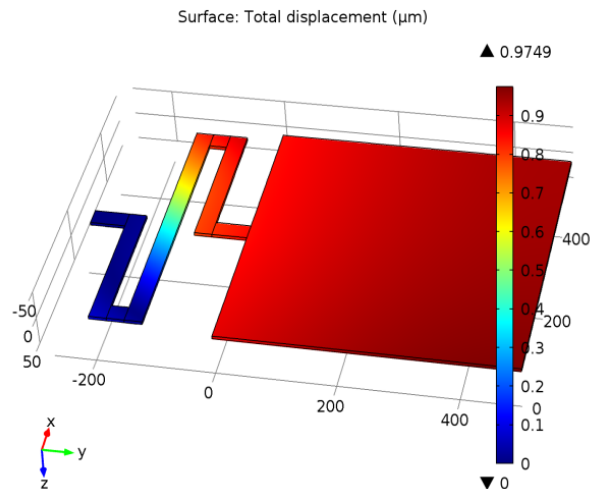


Figure 3.3: The simulation results for the deflection of the membrane in presence of 500 kV/m electric field.

Table 3-3: Simulation results for membrane sensor deflection vs. incident electric field.

<b>Electric Field</b>	<b>10 (kV/m)</b>	<b>50(kV/m)</b>	<b>100 (kV/m)</b>	<b>500 (kV/m)</b>	<b>1000 (kV/m)</b>
5 $\mu\text{m}$ thick copper membrane ( $\mu\text{m}$ )	3.77e-4	9.33e-3	0.0374	0.975	4.55
10 $\mu\text{m}$ thick copper membrane( $\mu\text{m}$ )	6.29e-5	1.57e-3	6.27e-3	0.158	0.626

Table 3-4: Theoretical expected values for membrane sensor deflection.

<b>Electric Field (kV/m)</b>	<b>10 (kV/m)</b>	<b>50 (kV/m)</b>	<b>100 (kV/m)</b>	<b>500 (kV/m)</b>	<b>1000 (kV/m)</b>
5 $\mu\text{m}$ thick copper membrane( $\mu\text{m}$ )	3.45e-4	8.38e-3	0.0335	0.838	3.34
10 $\mu\text{m}$ thick copper membrane( $\mu\text{m}$ )	5.21e-5	1.30e-3	5.21e-3	0.130	0.521

### 3.3 New design for solving the damping under ac field

This sensor system can also be implemented for the measurement of ac electric fields. The main difference between measuring the dc and ac electric fields is the motion of the membrane. Under the dc field, the membrane will be deflected to a steady state, however in the ac case the membrane vibrates. Imagine the case that we want to measure the amplitude of an ac electric field that has the same value of a dc electric field. In this case, and assuming no air drag and mass effects, the highest deflection of the membrane should

be the same as the deflection of the membrane in the steady state for measuring dc signals. This is only possible when the membrane's resonance is higher than the ac field frequency, and if air drag effect is minimized. For studying this situation a new model for the sensor is described below.

### **3.3.1 Membrane with holes to reduce the air drag**

In the new design, holes have been added to the surface of the membrane. Since we want to do the capacitance measurement, it is important to understand if the holes will affect the electrostatic force on the membrane from the incident field. This can be explored by determining if any incident field causes a charge build-up on the capacitive interrogating electrode below the perforated membrane. Since any charge on the underlying electrode would be a reduction in membrane charge, and so force on the membrane. To simulate this, a fixed grounded copper electrode has been added to the model, 5  $\mu\text{m}$  below the membrane. It has the same size of the membrane with same thickness. The model is used to first explore up to what size of holes the charge on the lower electrode would be negligible. Simulations were run for nine rectangular holes of the same size. The results are shown in Table 3-5.

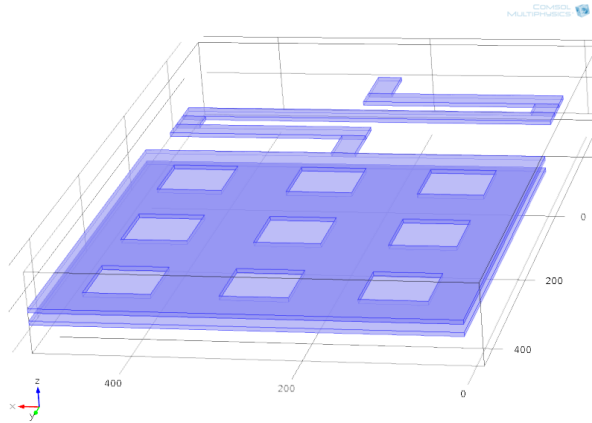


Figure 3.4: Sensor structure for AC measurement.

In the Table 3-5, Q1 stands for the charge on the total surface of the membrane and the Q2 stands for the charge on the surface of the lower electrode. It can be seen in Table 3-5 that for the holes with size less than 40 x 40  $\mu\text{m}$ , the value of Q2 compared to Q1 is less than 2.0%, and the reduction in Q1 is below 5%.

Table 3-5: Total charge at the surface of membrane and lower electrode. The electric field was 10 kV/m, thickness of the membrane was 5  $\mu\text{m}$  and lower electrode spacing was 5  $\mu\text{m}$ .

Hole size	Q1: Membrane charge (C)	Q2: Underlying electrode charge (C)	(Q2/Q1)*100 (%)
No holes	-5.59e-14	-5.64e-16	1.00%
10x10 $\mu\text{m}$	-5.57e-14	-5.62e-16	1.00%
20x20 $\mu\text{m}$	-5.51e-14	-6.29e-16	1.14%
30x30 $\mu\text{m}$	-5.44e-14	-8.36e-16	1.5%
40x40 $\mu\text{m}$	-5.36e-14	-1.10e-15	2.05%
50x50 $\mu\text{m}$	-5.32e-14	-1.41e-15	2.65%
60x60 $\mu\text{m}$	-4.99e-14	-2.67e-15	5.35%

A second set of simulations is shown in Table 3-6, where the membrane is perforated with an array of many holes, confined within a boundary of 50  $\mu\text{m}$  from the edge of the membrane. Three simulations are done, with 20 x 20  $\mu\text{m}$  holes with 20  $\mu\text{m}$  spacing, 40 x 40  $\mu\text{m}$  holes with 40  $\mu\text{m}$  spacing, and 80 x 80  $\mu\text{m}$  holes with 80  $\mu\text{m}$  spacing (Figure 3.5). The simulations for the three different sizes of the holes are shown in Table 3-6. As shown in Table 3-6 with holes up to the 40 x 40  $\mu\text{m}$  size, Q2 is below 5% from Q1. However, Q1 itself falls considerably compared to the case with no holes in the membrane shown in Table 3-5. This is due to the considerably larger surface area of holes, compared to the case in Table 3-5. Further study will need to be done with thicker membranes, and for larger membrane to underlying electrode spacing, to minimize the reduction in charge Q1 on the membrane, due to the presence of holes on the membrane surface.

Table 3-6: Total charge at the surface of membrane and lower electrode. The electric field was 10 kV/m, thickness of the membrane was 5  $\mu\text{m}$  and lower electrode spacing was 5  $\mu\text{m}$ .

Hole size	Q1: Membrane charge (C)	Q2: Underlying electrode charge (C)	(Q2/Q1)*100 (%)
20x20 $\mu\text{m}$	-4.84e-14	-2.23e-16	0.46%
40x40 $\mu\text{m}$	-4.49e-14	-3.70e-16	0.82%
80x80 $\mu\text{m}$	-4.00e-14	-6.22e-15	15.5%

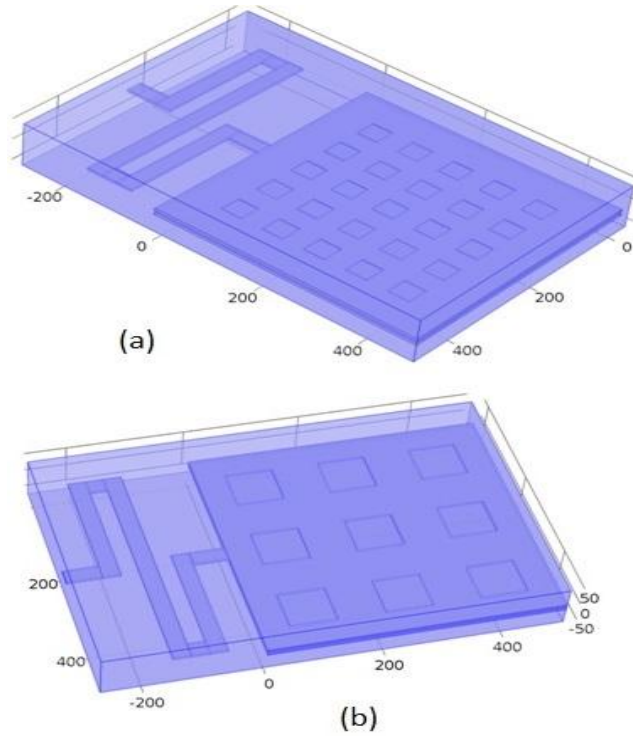


Figure 3.5: Membrane design with 50% duty cycle holes: (a) 40x40 holes. (b) 80x80 holes.

### 3.3.2 Air drag effect on the sensor motion for incident ac electric fields

For studying the effect of the air drag on the motion of the sensor under the ac field the same model with holes is used. In order to calculate the air drag force which is caused by the motion of the membrane under an ac field by voltage of “ $A\sin(\omega t)$ ”; where  $A$  is the amplitude and  $\omega$  is the frequency of ac voltage, two sets of the simulations have been done as described below: (Note: This is valid with the assumption that ac frequencies are much lower than the resonance frequency of the structure)

- 1- Calculating the deflection of the membrane under the dc field with value of “ $m$ ” which defines the maximum of the deflection that the membrane will have under the ac field with voltage value of “ $A\sin(\omega t)$ ”.
- 2- Calculating the air drag force by applying an air flow to the surface of the membrane. The air flow speed is calculated based on the maximum deflection of

the membrane which is calculated in first set of simulations and the voltage frequency which is defining the required time for reaching to the maximum deflection.

### Calculating the maximum deflection

The COMSOL model which is used for the first set of the simulations is as shown in Figure 3.2. The dc voltage is applied to the upper side of the box and the lower side and the membrane are grounded. The voltage from 1 to 50V applied for creating the electric field and applying electrostatic force to the solid metal membrane. The same simulation has been done on the membranes with 40 $\mu\text{m}$  x 40 $\mu\text{m}$  and 80 $\mu\text{m}$  x 80 $\mu\text{m}$  holes. The results for the deflection values are as shown in Table 3-7 to Table 3-12. The simulations have been done for the membranes with thickness of 5 and 10  $\mu\text{m}$ .

#### D) The simulation results for 5 $\mu\text{m}$ thick membranes

Table 3-7: Simulation results for solid membrane with thickness of 5 $\mu\text{m}$

Applied Voltage (V)	Electric Field on the membrane surface (V/m)	Electric Charge (C)	Deflection	Electrostatic force (N)
1	22221.1	-4.98455e-14	0.397nm	1.1075e-10
10	2.21153e5	-5.00783e-13	0.0398 $\mu\text{m}$	1.105e-7
25	5.38096e5	-1.25073e-12	0.2512 $\mu\text{m}$	6.726e-7
50	9.35966e5	-2.49208e-12	1.0408 $\mu\text{m}$	2.332e-6

Table 3-8: Simulation results for 5 $\mu\text{m}$  thick membranes and 40 $\mu\text{m}$ x40 $\mu\text{m}$  holes

Applied Voltage (V)	Electric Field on the membrane surface (V/m)	Electric Charge (C)	Deflection	Electrostatic force (N)
1	22222.7	-4.41119e-14	0.3719nm	9.8029e-10
10	2.21238e5	-4.41015e-13	0.0373 $\mu\text{m}$	9.7569e-8
25	5.39511e5	-1.10113e-12	0.2351 $\mu\text{m}$	5.9407e-7
50	9.59356e5	-2.19146e-12	0.9736 $\mu\text{m}$	2.1024e-6

Table 3-9: Simulation results for 5 $\mu\text{m}$  thick membranes and 80 $\mu\text{m}$ x80 $\mu\text{m}$  holes

Applied Voltage (V)	Electric Field on the membrane surface (V/m)	Electric Charge (C)	Deflection	Electrostatic force (N)
1	22244.6574	-4.0842e-14	0.3535nm	9.0852e-10
10	2.21507e5	-4.08315e-13	0.0354 $\mu\text{m}$	9.0445e-8
25	5.40712e5	-1.01937e-12	0.2233 $\mu\text{m}$	5.5119e-7
50	9.62597e5	-2.0279e-12	0.9244 $\mu\text{m}$	1.9521e-6

II) The simulation results for 10 $\mu\text{m}$  thick membranes

Table 3-10: Simulation results for solid membrane with thickness of 10 $\mu\text{m}$

Applied Voltage (V)	Electric Field on the membrane surface (V/m)	Electric Charge (C)	Deflection	Electrostatic force (N)
1	24999.92987	-5.5976e-14	6.368e-11	1.3994e-9
10	2.4993e5	-5.59746e-13	6.37nm	1.3990e-7
25	6.23901e5	-1.39919e-12	0.0399 $\mu\text{m}$	8.7296e-7
50	1.24113e6	-2.79708e-12	0.1605 $\mu\text{m}$	3.4715e-6

Table 3-11: Simulation results for 5 $\mu$ m thick membranes and 40 $\mu$ m $\times$ 40 $\mu$ m holes

Applied Voltage (V)	Electric Field on the membrane surface (V/m)	Electric Charge (C)	Deflection	Electrostatic force (N)
1	25000.80823	-4.90217e-14	5.901e-11	1.2256e-9
10	2.49944e5	-4.90201e-13	5.9nm	1.2252e-7
25	6.24008e5	-1.22529e-12	0.037 $\mu$ m	7.6459e-7
50	1.24186e6	-2.44909e-12	0.1486 $\mu$ m	3.0414e-6

Table 3-12: Simulation results for 10 $\mu$ m thick membranes and 80 $\mu$ m $\times$ 80 $\mu$ m holes

Applied Voltage (V)	Electric Field on the membrane surface (V/m)	Electric Charge (C)	Deflection	Electrostatic force (N)
1	25013.57991	-4.51119e-14	5.643e-11	1.1284e-9
10	2.50073e5	-4.51103e-13	5.64nm	1.1281e-7
25	6.24341e5	-1.12755e-12	0.053 $\mu$ m	7.0398e-7
50	1.24262e6	-2.25363e-12	0.1421 $\mu$ m	2.8004e-6

### Calculating the air drag force

For calculating the air drag force, a COMSOL model the same as in Figure 3.2 is used, by the modification that instead of having any electric potential in the model, an airflow is coming from the upper side of the box and flowing to the membrane. COMSOL is solving Navier-Stokes equations for finding the pressure which is caused by the air flow to the surface area of the membrane; by multiplying the surface area to the pressure the air drag force will be calculated. In order to start the simulations first the mean airflow velocity was calculated from the deflection values which are calculated in the previous set of simulations. The airflow velocity is calculated from equation 3.3:

$$\text{Velocity} = \frac{dx}{dt} \quad (3.3)$$

where  $t$  is the time and  $x$  is the deflection of the membrane. Since the  $x$  is proportional to the square of the voltage (see equation 2.15), then:

$$x \propto V^2 \quad (3.4)$$

And the voltage is ac with frequency of  $\omega$ , then we have,

$$V = A \sin(\omega t) \quad (3.5)$$

From equations 3.4-5 it can be concluded that;

$$x \propto V^2 \quad (3.6)$$

$$\text{Velocity} \propto 2A^2 \omega \sin(\omega t) \cos(\omega t) \quad (3.7)$$

$$\text{Velocity} \propto A^2 \omega \sin(2\omega t), \quad \omega = 2\pi f \quad (3.8)$$

By making an assumption that the maximum velocity of the membrane during the membrane vibration is  $m\omega$  ( $m$  is the maximum deflection of membrane), the maximum velocity of the air flow can be calculated as  $m2\pi f$ . The simulation has been done for both solid membranes and membranes with holes to see the effect of the air drag on their vibration. The simulation results have been shown in Tables 3-13 to 18, for the frequency of 100 Hz.

Table 3-13: Simulation results for solid membrane with thickness of 5 $\mu$ m

<b>Airflow (m/s)</b>	<b>Pressure (Pa)</b>	<b>Area (mm<sup>2</sup>)</b>	<b>Air drag force (N)</b>
2.57256e-6	7.8e-9	1mm	7.8e-15
2.57904e-5	0.00789	1mm	7.89e-9
1.62778e-4	0.0495	1mm	4.95e-8
6.74438e-4	0.1986	1mm	1.98e-7

Table 3-14: Simulation results for 5 $\mu$ m thick membranes and 40 $\mu$ m $\times$ 40 $\mu$ m holes

<b>Airflow (m/s)</b>	<b>Pressure (Pa)</b>	<b>Area (mm<sup>2</sup>)</b>	<b>Air drag force (N)</b>
2.40991e-6	1.943e-9	9.6e-1	1.8653e-15
2.40991e-6	1.950e-3	9.6e-1	1.8720e-09
2.40991e-6	0.0123	9.6e-1	1.1808e-08
2.40991e-6	0.05091	9.6e-1	4.8874e-08

Table 3-15: Simulation results for 5 $\mu$ m thick membranes and 80 $\mu$ m $\times$ 80 $\mu$ m holes

<b>Airflow (m/s)</b>	<b>Pressure (Pa)</b>	<b>Area (mm<sup>2</sup>)</b>	<b>Air drag force (N)</b>
2.29068e-6	7.193e-11	9.4240e-1	6.7787e-17
2.29392e-5	7.1994e-9	9.4240e-1	6.7847e-15
1.44698e-4	4.537e-3	9.4240e-1	4.2757e-09
5.99011e-4	0.0188	9.4240e-1	1.7717e-08

Table 3-16: Simulation results for solid membrane with thickness of 10 $\mu$ m

<b>Airflow (m/s)</b>	<b>Pressure (Pa)</b>	<b>Area (mm<sup>2</sup>)</b>	<b>Air drag force (N)</b>
4.12646e-8	1.724e-11	1	1.724e-17
4.12776e-6	1.251e-3	1	1.251e-9
2.58552e-5	0.0108	1	1.08e-8
1.04004e-4	0.0541	1	5.41e-8

Table 3-17: Simulation results for 10 $\mu$ m thick membranes and 40 $\mu$ m $\times$ 40 $\mu$ m holes

<b>Airflow (m/s)</b>	<b>Pressure (Pa)</b>	<b>Area (mm<sup>2</sup>)</b>	<b>Air drag force (N)</b>
3.82385e-08	3.87e-13	9.6e-1	3.7152e-19
3.8232e-06	1.2403e-9	9.6e-1	1.119e-10
2.3976e-5	2.432e-3	9.6e-1	2.3347e-09
9.62928e-05	9.772e-3	9.6e-1	9.3811e-9

Table 3-18: Simulation results for 10 $\mu$ m thick membranes and 80 $\mu$ m $\times$ 80 $\mu$ m holes

<b>Airflow (m/s)</b>	<b>Pressure (Pa)</b>	<b>Area (mm<sup>2</sup>)</b>	<b>Air drag force (N)</b>
3.65666e-8	1.41e-13	9.4240e-1	1.3288e-19
3.65472e-6	1.416e-9	9.4240e-1	1.3344e-15
3.4344e-5	1.331e-3	9.4240e-1	1.2543e-9
9.20808e-05	3.569e-3	9.4240e-1	3.3634e-9

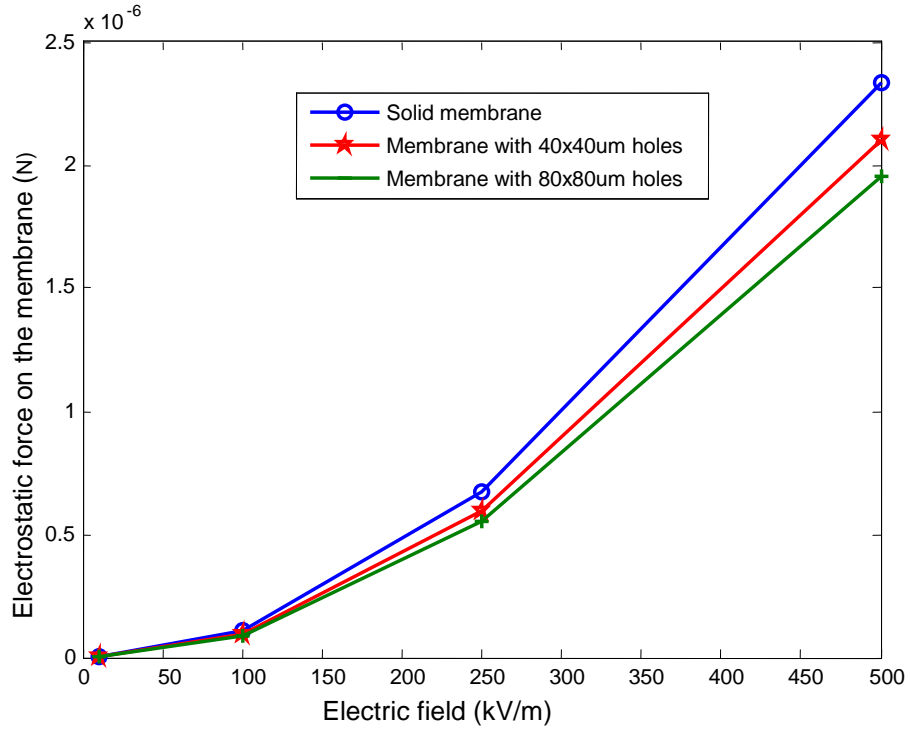


Figure 3.6: The electrostatic force on different 5µm thick membranes

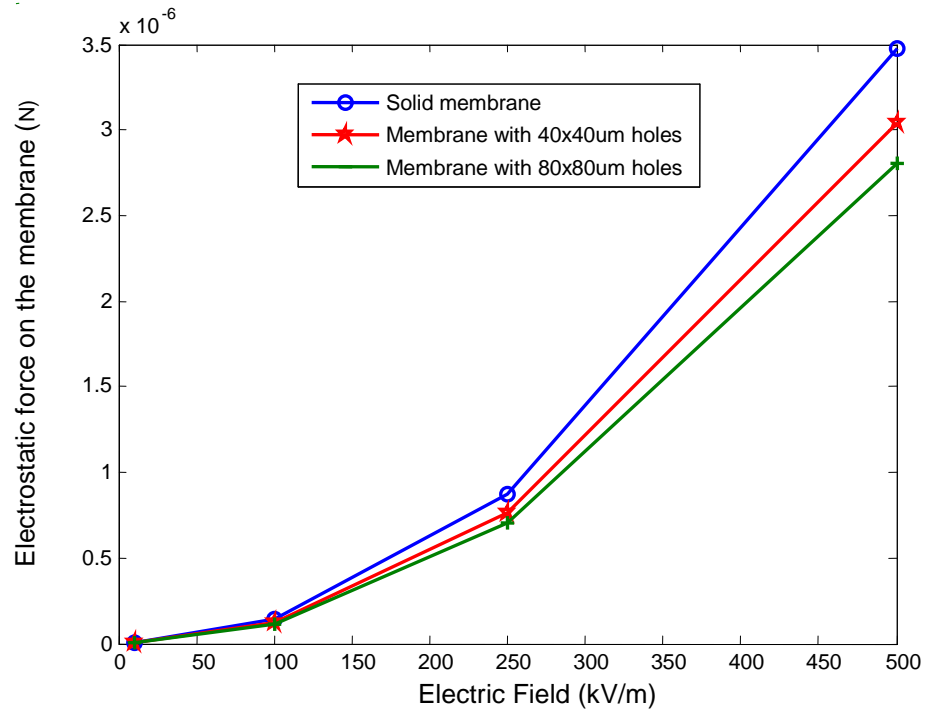


Figure 3.7: The electrostatic force on different 10µm thick membranes

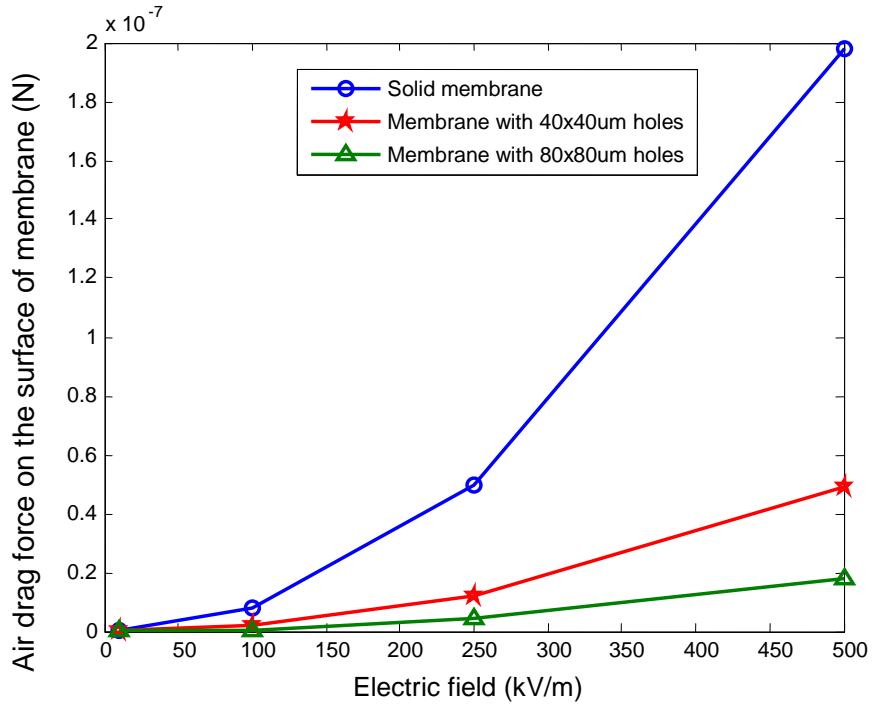


Figure 3.8: The air drag force on the different 5µm thick membranes, using the mean velocity for the dc electric field.

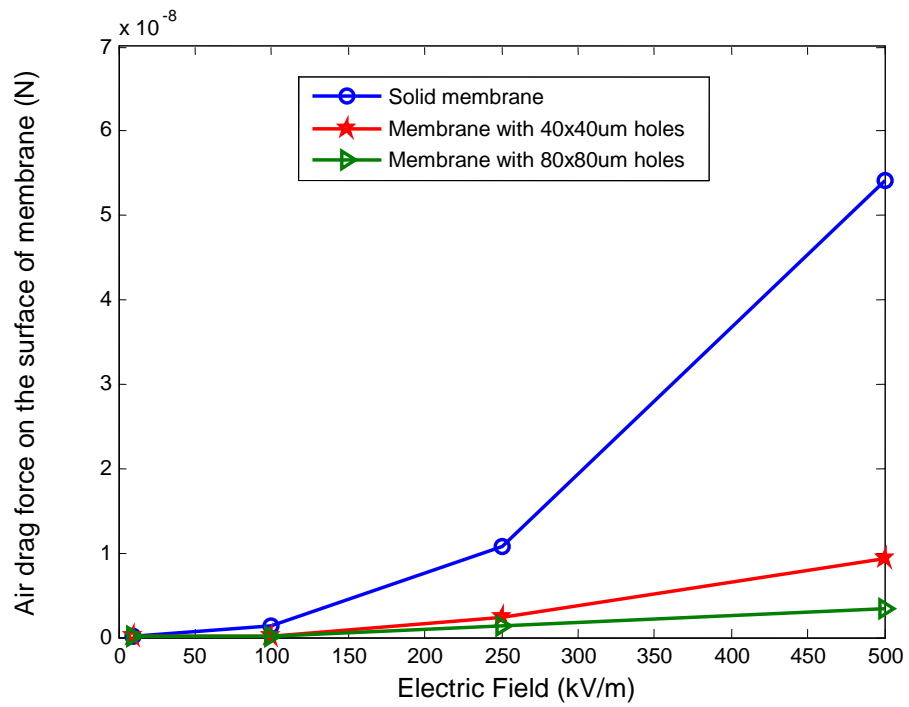


Figure 3.9: The air drag force on the different 10µm thick membranes, using the mean velocity for the dc electric field.

From the simulated results, Table 3-19 and 3-20, it can be seen that in the solid membranes the air drag force in presence of 100 kV/m fields and higher approaches to 10% of the electrostatic force which will cause problems for the membrane movement. By comparison in the membranes with holes the air drag force is reduced to less than 1% of the electrostatic force for the same applied electric field. This indicates that using holes in the membranes structure has the potential to solve the membrane's air drag problem under the ac electric field.

Table 3-19: Simulation results for 5μm thick membranes

<b>Electric field (kV/m)</b>	<b>Structure</b>	<b>Electrostatic force (F1) (N)</b>	<b>Air drag force F(2) (N)</b>	<b>(F(2)/F(1))*100 %</b>
10	Solid membrane	1.1075e-10	7.8e-15	<0.001
	Membrane with 40μm*40μm holes	9.8029e-10	1.8653e-15	<0.001
	Membrane with 80μm*80μm holes	9.0852e-10	6.7787e-17	<0.001
100	Solid membrane	1.105e-7	7.89e-9	7.1
	Membrane with 40μm*40μm holes	9.7569e-8	1.8720e-9	1.9
	Membrane with 80μm*80μm holes	9.0445e-8	6.7847e-15	<0.001
250	Solid membrane	6.726e-7	4.95e-8	7.3
	Membrane with 40μm*40μm holes	5.9407e-7	1.1808e-8	2.0
	Membrane with 80μm*80μm holes	5.5119e-7	4.2757e-9	0.72
500	Solid membrane	2.332e-6	1.98e-7	8.5
	Membrane with 40μm*40μm holes	2.1024e-6	4.8874e-8	2.3
	Membrane with 80μm*80μm holes	1.9521e-6	1.7717e-8	0.91

Table 3-20: Simulation results for 10 $\mu$ m thick membranes.

Electric field (kV/m)	Structure	Electrostatic force (F1) (N)	Air drag force F(2) (N)	(F(2)/F(1))*100 %
10	Solid membrane	1.3994e-9	1.724e-17	<0.001
	Membrane with 40 $\mu$ m*40 $\mu$ m holes	1.2256e-9	3.7152e-19	<0.001
	Membrane with 80 $\mu$ m*80 $\mu$ m holes	1.1284e-9	1.3288e-19	<0.001
100	Solid membrane	1.3990e-7	1.251e-9	0.88
	Membrane with 40 $\mu$ m*40 $\mu$ m holes	1.2252e-7	1.119e-10	<0.1
	Membrane with 80 $\mu$ m*80 $\mu$ m holes	1.1281e-7	1.3344e-15	<0.001
250	Solid membrane	8.7296e-7	1.08e-8	1.2
	Membrane with 40 $\mu$ m*40 $\mu$ m holes	7.6459e-7	2.3347e-9	0.18
	Membrane with 80 $\mu$ m*80 $\mu$ m holes	7.0398e-7	1.2543e-9	0.12
500	Solid membrane	3.4715e-6	5.41e-8	1.56
	Membrane with 40 $\mu$ m*40 $\mu$ m holes	3.0414e-6	9.3811e-9	0.12
	Membrane with 80 $\mu$ m*80 $\mu$ m holes	2.8004e-6	3.3634e-9	0.08

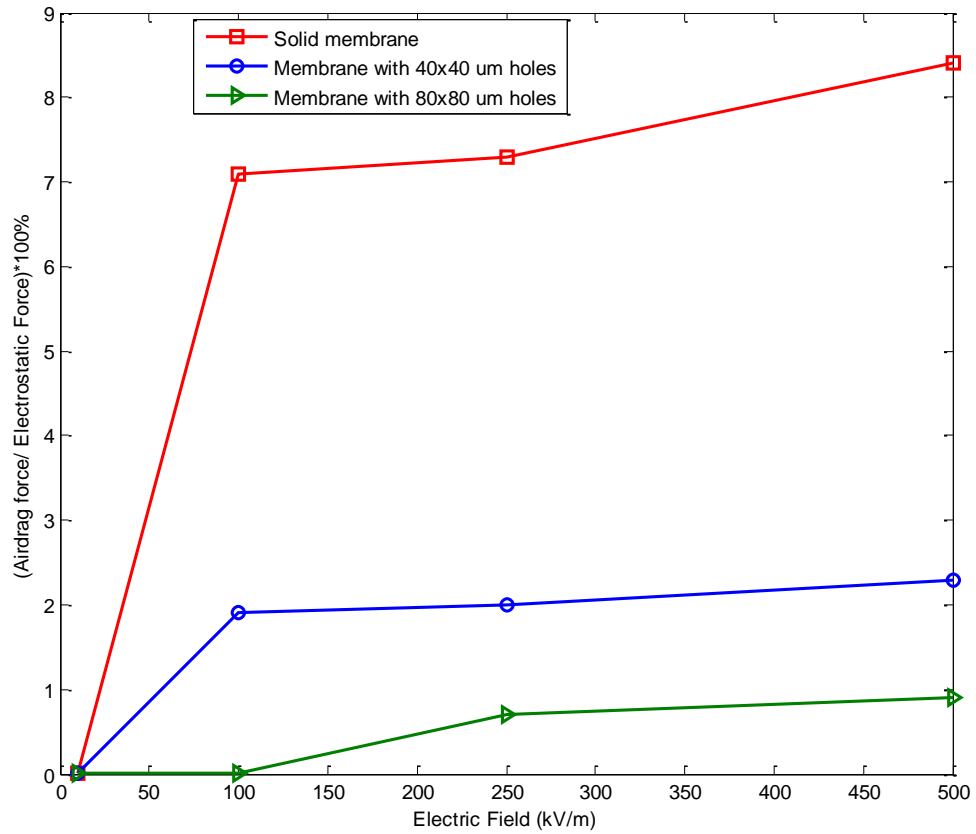


Figure 3.10: Air drag as a percentage of electrostatic force for different membranes.

In order to study the effect of the frequency of the ac field on the behavior of the membrane's deflection, the same study was performed on solid membranes and membranes with holes for different frequencies. In this set of simulations the electric field was 500kV/m, because it has the largest ratio between air drag force and electrostatic force in the previous simulations. The thickness of the membrane was 5  $\mu\text{m}$ , because from the previous simulation (Tables 3-19 and 3-20) it can be seen that the ratio between air drag force and electrostatic force is not large enough for the case of 10 $\mu\text{m}$ . The results are shown in Table 3-21 and Figure 3.11. From the results it can be seen that

adding the perforations to the membrane plays the same role in different frequencies and will reduce the air drag force effect on the vibration of the membrane.

Table 3-21: Simulation results for 5 $\mu$ m thick membranes, in presence of 500 kV/m field

Frequency	Membrane Type	Airflow	Pressure	Area (mm <sup>2</sup> )	Air drag force (F2)	Electrostatic force (F1)	(F1/F2)*100%
50 (Hz)	Solid membrane	3.372 e-4	0.0981	1	9.813e-8	2.332e-6	4.2
	Membrane with 40 $\mu$ m*40 $\mu$ m holes	3.059 e-4	0.0246	9.6e-1	2.364e-8	2.1024e-6	1.12
	Membrane with 80 $\mu$ m*80 $\mu$ m holes	2.995 e-4	0.0091	9.424e-1	8.574e-9	1.9521e-6	0.44
100 (Hz)	Solid membrane	6.7443e-4	0.1986	1	1.982e-7	2.332e-6	8.5
	Membrane with 40 $\mu$ m*40 $\mu$ m holes	6.1173e-4	0.05091	9.6e-1	4.881e-8	2.1024e-6	2.3
	Membrane with 80 $\mu$ m*80 $\mu$ m holes	5.9901e-4	0.0188	9.424e-1	1.777e-8	1.9521e-6	0.91
150 (Hz)	Solid membrane	1.0116e-3	0.2893	1	2.898e-7	2.332e-6	12.4
	Membrane with 40 $\mu$ m*40 $\mu$ m holes	9.177e-4	0.0742	9.6e-1	7.129e-8	2.1024e-6	3.4
	Membrane with 80 $\mu$ m*80 $\mu$ m holes	8.985e-4	0.0285	9.424e-1	2.681e-8	1.9521e-6	1.4
200 (Hz)	Solid membrane	1.3489 e-3	0.3878	1	3.873e-7	2.332e-6	16.6
	Membrane with 40 $\mu$ m*40 $\mu$ m holes	1.2235 e-3	0.0987	9.6e-1	9.471e-8	2.1024e-6	4.5
	Membrane with 80 $\mu$ m*80 $\mu$ m holes	1.1980 e-3	0.0381	9.424e-1	3.595e-8	1.9521e-6	1.8

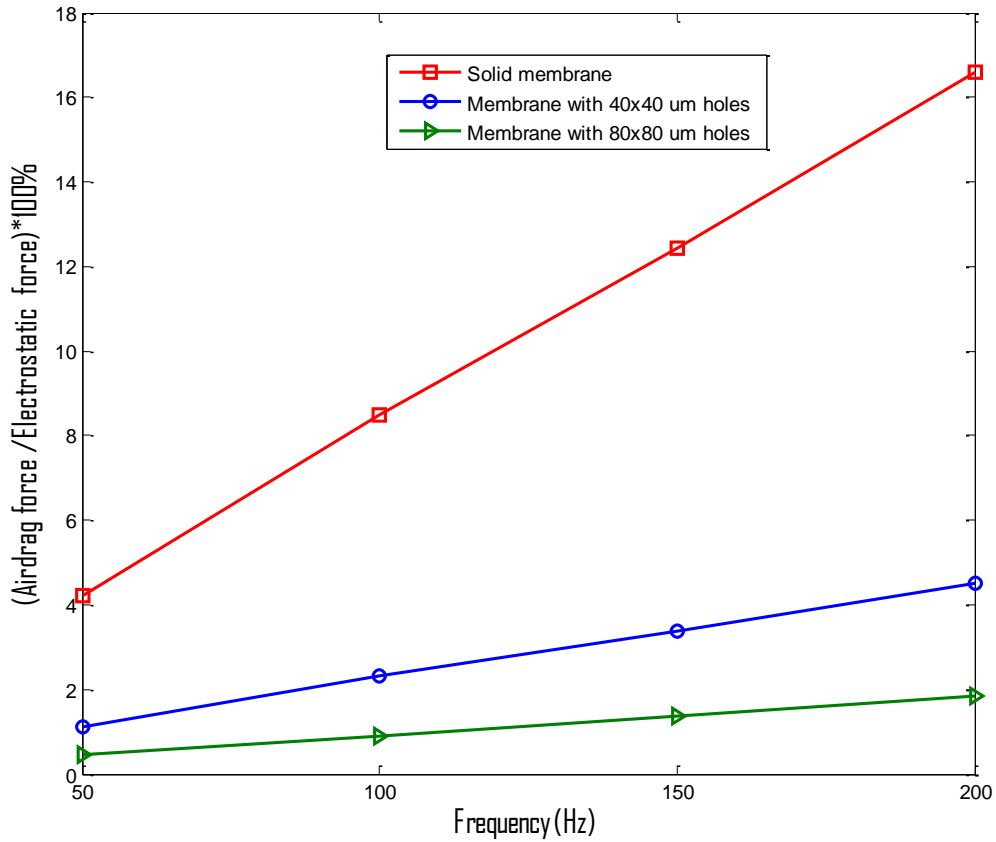


Figure 3.11: Air drag force as electrostatic force in different frequencies.

### 3.4 Natural frequencies of the different structures

The designed sensor should operate such that during the measurement of the ac fields, the maximum deflection of the membrane be the same as the deflection of membrane under dc fields at the equilibrium state. This is only possible when the damping effect is minimized. In the previous section we showed a new design for reducing the damping effect. In this section by calculating the resonance frequency of the system for different designs we will show that frequency of the ac measured signals are much lower than the resonance frequency of the structure. This means that the motion of the structure is very

slow compared to the resonance frequency and the mass effect which is proportional with the second derivative of the membrane motion is very small and can be neglected. Table 3-22 is showing the resonance frequency of different structures. The resonance frequency is calculated from  $\omega_r = \omega_0 \sqrt{1 - 2\zeta^2}$  and  $\zeta = \frac{b}{2\sqrt{mk}}$ . The value of  $b=110$  mg/s was used for the calculations. [29]

Table 3-22: Resonate frequency of different structures

Membrane Thickness	Membrane type	Membrane mass	Spring constant	Natural Frequency ( $\omega_0$ )	Resonance Frequency ( $\omega_r$ )
5 $\mu$ m	Solid membrane	4.47e-8 kg	1.65	6.03 kHz	5.78 kHz
	Membrane with 40 $\mu$ m x40 $\mu$ m holes	4.29e-8 kg	1.65	6.20 kHz	5.95 kHz
	Membrane with 80 $\mu$ m x80 $\mu$ m holes	4.21e-8 kg	1.65	6.26 kHz	6.00 kHz
10 $\mu$ m	Solid membrane	8.94e-8 kg	13.2	12.15 kHz	12.02 kHz
	Membrane with 40 $\mu$ m x40 $\mu$ m holes	8.58e-8 kg	13.2	12.40 kHz	12.27 kHz
	Membrane with 80 $\mu$ m x80 $\mu$ m holes	8.42e-8 kg	13.2	12.52 kHz	12.39 kHz

As shown in table 3-22, the resonance frequencies of all the designed structures are more than ten times higher than frequency of ac measured signals.

### 3.5 Sensor Output vs. Electric Field

In order to check the sensor's capability for sensing the electric field, it is necessary to calculate the corresponding capacitance change of the sensor for different deflection values of the membrane. The capacitance of the 5 $\mu$ m thick, solid membrane sensor in the initial state for the case of 1x1 mm<sup>2</sup> membrane and electrode, with a gap of 5 $\mu$ m is calculated by: [19]

$$C = \epsilon_0 \epsilon_r \frac{A}{d} \quad (3.8)$$

where, A is the area of the membrane and electrode, d is the gap between them and  $\epsilon_0$  and  $\epsilon_r$  are permittivity of the free space and relative permittivity of air.

Table 3-23: Corresponding Capacitance change for membrane deflections for 5 $\mu$ m thick membrane.

Approximated electric field	Deflection Value	C <sub>initial</sub>	$\Delta C$
5 kV/m	0.1nm	1.77 pF	3.5e-17 F
16 kV/m	1nm	1.77 pF	0.35fF
50 kV/m	10nm	1.77 pF	3.54fF
160 kV/m	100nm	1.77 pF	36.1fF
500 kV/m	1 $\mu$ m	1.77 pF	0.44pF
790 kV/m	2.5 $\mu$ m	1.77 pF	1.77pF

By referring to the datasheet of our capacitance to digital convertor (AD7747) [32], it can be found that the device is capable of sensing capacitance changes of 32 aF and higher. Therefore, for the deflection of 0.1nm and higher we are capable of sensing the electric field, which is electric field of 5 kV/m and higher.

### **3.6 Conclusions**

A new design has been shown for the membrane based electric field sensor. For dc electric field measurement simulations, the electrostatic force applied to the membrane deflects the membrane vertically towards the field. The deflection of the membrane has been calculated from both theory and simulation by COMSOL. Comparing the simulation results and the expected theoretical values shows that the model is working properly and this design potentially is a proper design for the sensor. In addition, the range of the deflection of membrane is large enough to be detected by our capacitance to digital convertor (AD7747). Simulations were done to explore perforated membranes for operation in the presence of ac fields. Holes added to the surface of the membrane reduce the effect of air drag force on the membrane. However, larger holes result in reduced the electrostatic force on the membrane, reducing sensor sensitivity. The other sets of simulation have been done for studying the role of perforation on the air drag force. It has been shown that adding perforation will reduce the air drag force and facilitate membrane motion under the ac fields. The same behavior was observed for the membrane deflection under electric field with different frequencies. This shows that while perforation has positive effect on reducing the air drag issue during the vibration of the membrane, at the same time by increasing the holes sizes will reduce the electrostatic force and subsequently will reduce the sensitivity of the sensor. This trade-off can result

in general improvement in performance of the sensor as long as the size of the perforations is chosen smartly, like case of 40x40  $\mu\text{m}$  holes in this study. For getting the best results, further studies need to be done to find out the optimized size of perforations.

### **3.7 Future Work**

The thickness of the simulated membrane should be optimized to find out the best deflection results while having an acceptable mechanical stability for the structure. For the ac field measurement, the structure of the sensor is not still optimized. Several factors such as spacing between the holes and gap between the membrane and lower electrode should be studied to find the minimum mass of the membrane with the highest charge on the surface of the membrane. As well, the effect of the air drag on the sensor motion for incident ac electric fields needs to be explored as a function of perforation geometry. A study on the size and geometry of the perforation should be done to find out the optimized value of sensitivity while reducing the air drag effect on the membrane vibration.

## **4. Chapter Four**

# **Sensor Fabrication**

Figure 4.1 shows the schematic of the sensor. The sensor consists of a copper made membrane (Electroplated copper) mounted on top of a reference electrode (patterned sputtered copper on glass) with a gap in between, provided by a spacer. The fabrication process of the copper made membrane consists of three general steps:

- 1- Silicon wafer back etching and lithography process for creating photoresist mold for electroplating
- 2- Electroplating of the copper made membranes on silicon wafer
- 3- Releasing of the electroplated structure

In this chapter we will discuss these steps in detail. In order to start each step, first the fabrication process should be designed, then lithography masks should be designed for patterning during the fabrication process.

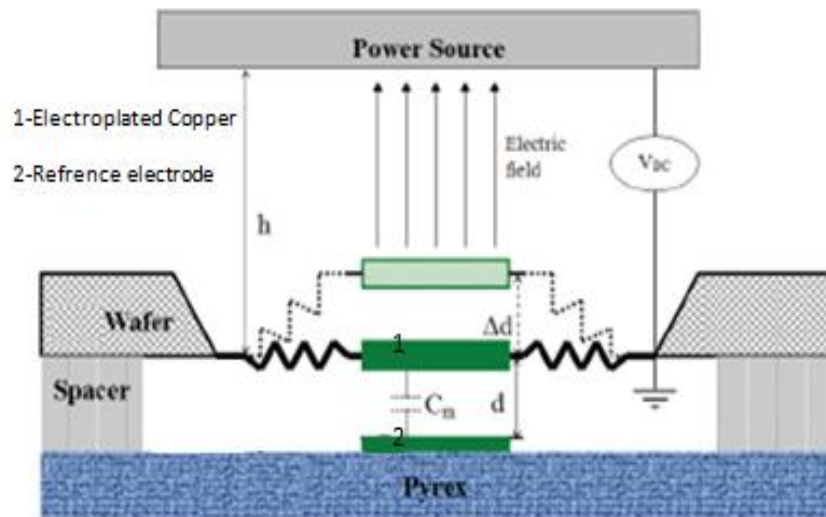


Figure 4.1: Schematic of the designed sensor.

## **4.1 Silicon wafer back etching and photoresist mold patterning**

In order to fabricate the copper made membrane on a silicon wafer, it is necessary to etch the backside of silicon wafer under the electroplated membranes first. Because it makes us able to release the electroplated structure in the last step. The fabrication of the sensors is done on a 3'', 400  $\mu\text{m}$  thick,  $\langle 100 \rangle$  silicon wafer with a pre-deposited 200 nm  $\text{Si}_3\text{N}_4$  film on both sides. The silicon wafer with nitride layers has been chosen because the nitride layer protects the silicon wafer in the KOH solution, from being etched. The etching process will just take place in the areas that the nitride layer has been removed, therefore we are able to create the back etch holes by removing the nitride layer from specific parts of the wafer while protecting the rest of the wafer from any damages in the etching bath. Back side etching process will take place in a KOH (potassium hydroxide) bath, and we want to etch the wafer down until we get less than 10% of the wafer thickness, 35 nm. Because 35 nm is thick enough to survive during the microfabrication processes and thin enough to be released at the last step by plasma etching. After creating the back etch holes, the seed layer for electroplating should be sputtered on the silicon wafer frontside. Then the photoresist mold should be created on top of seed layer by lithography techniques in order to make the sample ready for electroplating. The details of these processes will be discussed in details in this section.

### **4.1.1 Silicon wafer back etching and mold patterning process design**

The designed fabrication process is shown in figures 4.2-4.5 (Note: Figures are not in scale).

- 1- First a 3" silicon wafer which has silicon nitride layer in both sides is patterned with SPR504 photoresist on its backside. Then in the areas which were not covered by the resist, nitride layer is etched with reactive ion etching.



Figure 4.2: Nitride layer photoresist patterning and plasma etching.

- 2- The back etch is done (in the potassium hydroxide, KOH, bath) through the etched silicon nitride openings to form a diaphragm structures.



Figure 4.3: backside etching in KOH bath

- 3- The silicon nitride layer is removed from the frontside of the wafer, using RIE<sup>3</sup>, and a seed layer of copper is sputtered on the frontside.



Figure 4.4: Front side nitride plasma etching and copper metallization

- 4- The seed layer of the copper is patterned with photoresist to make a mold for the copper electroplating.

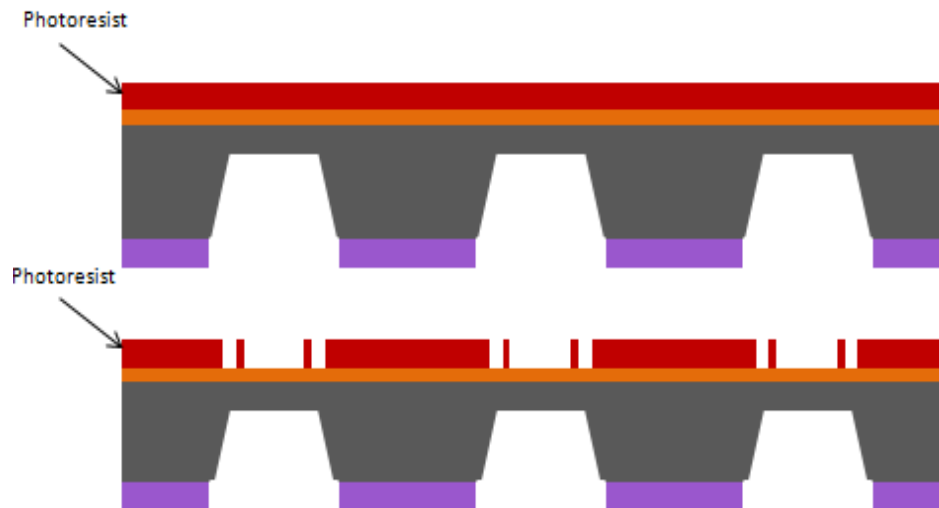


Figure 4.5: patterning the seed layer with photoresist and preparing the mold for electroplating

For designing the mask of the back etch holes, it is necessary to be familiar with the structure of the membranes and springs. In the next section the structure of the sensors

---

<sup>3</sup> Reactive Ion etching

will be introduced and based on that lithography masks for different purposes will be designed.

#### **4.1.2 Mask design**

Two masks are needed for membrane fabrication; top layer mask for membranes patterning and the back etch mask for releasing the electroplated membranes. Also a mask layer is needed for the lower electrode patterning. In order to study different types of the membranes, three types of the membranes has been drawn on the mask. The first type of the membrane is the same as the solid membrane in chapter 3, the second type is the same membrane with holes and the third membrane designed to have double length of spring, to have less spring constant for more flexibility in case the fabricated membranes have lower deflection in presence of the electric field compared to the simulation results (Figure 4.6). Three sizes of each type of the membranes have been drawn on the mask which results in total of nine membranes. Therefore there are three 1mm x 1mm, three 2mm x 2mm, and three 3mm x 3mm membranes in the mask design. Basically all the feature sizes of the simulated membrane (membrane sizes, spring width, spring length, holes sizes) has been multiplied by two for the 2mm x 2mm membrane and by three for the 3mm x 3mm membrane. As illustrated in Figure 4.7, the springs length for the 1mm x 1mm membrane, type A, is 470 $\mu$ m and the width of the spring is 210 $\mu$ m. Type B has the same size of membrane and springs, the only difference is the holes in its membrane. The holes are designed to be 40 $\mu$ m x 40 $\mu$ m. Type C has the same membrane structure of type A with different spring length which is 940 $\mu$ m for this type.

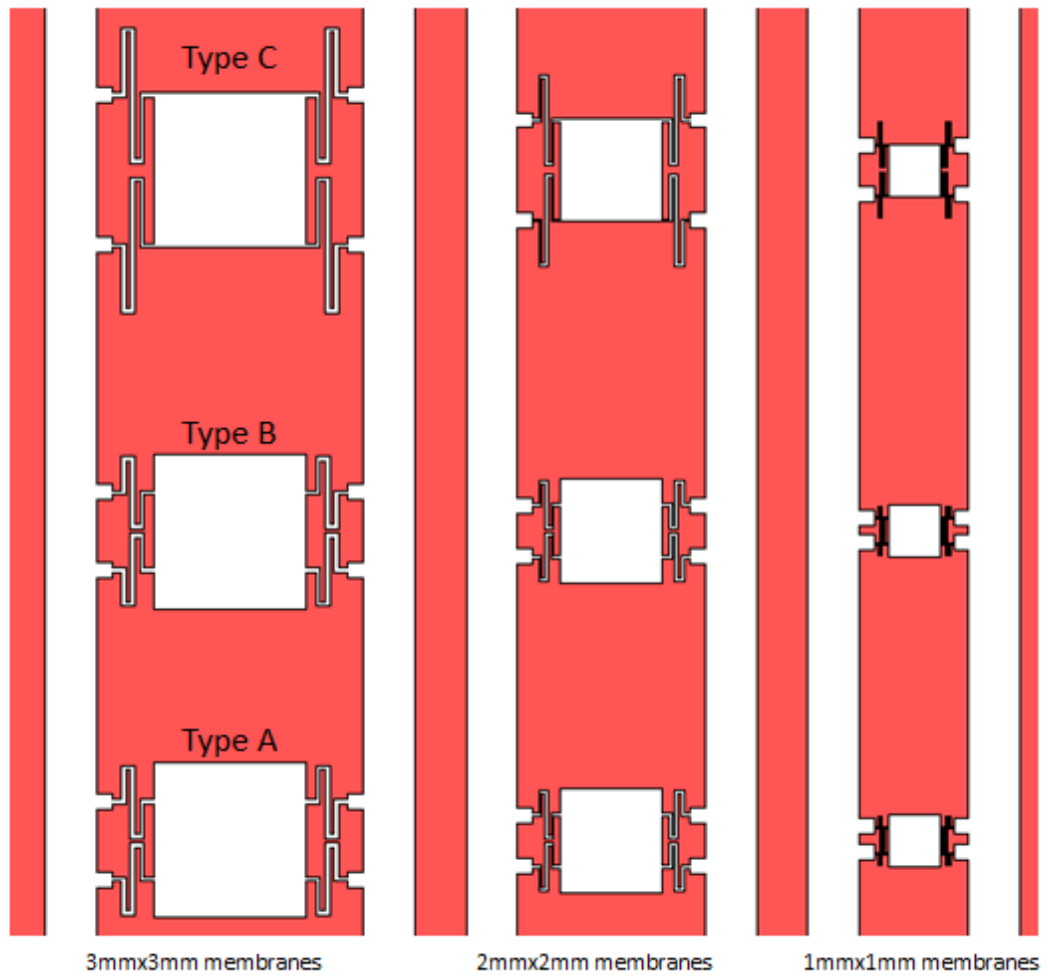


Figure 4.6: Frontside mask for making mold before electroplating of the membranes

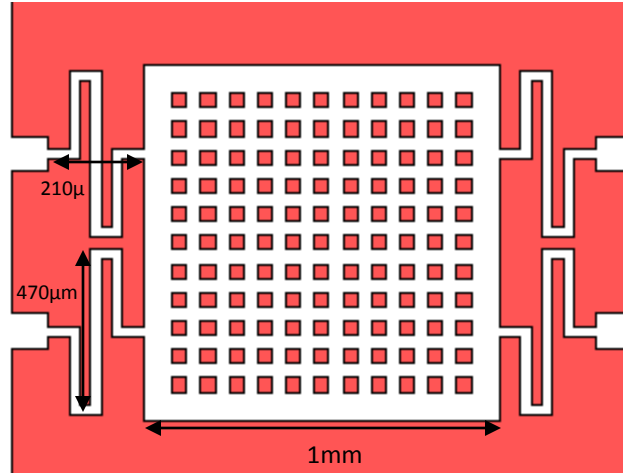


Figure 4.7: 1mm x 1mm Type B membrane with the 40μm x 40μm holes. Type A has the same sizes for the springs and membrane without any holes. There are no holes in Type C and spring length is 940μm instead of the 470μm and the rest of the sizes are the same.

### Back etch mask

As mentioned in the fabrication process design section, before starting the sensors patterning and electroplating, for each membrane a backside hole should be etched in order to release the structure after the electroplating step. Therefore the backside etch mask should consist of nine rectangular holes. The size of the back-etch holes should be designed by considering three factors; membrane and springs sizes, silicon horizontal etch due to anisotropic etching of silicon in KOH and alignment error. The membrane and spring sizes are known from the front mask design but the other two factors should be calculated. The thickness of the wafers has been measured in order to calculate the horizontal etch value, the thickness of the wafers was 385μm. The size of the horizontal etch can be calculated from:

$$a = b \times \tan^{-1}(\alpha) \quad (4.1)$$

where  $a$  is the lateral (horizontal) etch,  $b$  is the depth of the etch and  $\alpha$  is the angle of the side walls of the holes. By assuming  $b$  as  $360\mu\text{m}$ ,  $a$  is calculated as  $254.9\mu\text{m}$  which in our design  $255\mu\text{m}$  is used as an approximate value.

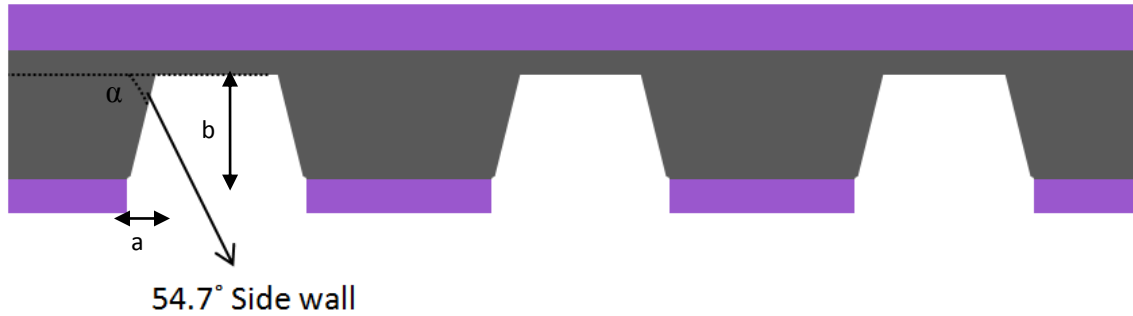


Figure 4.8: Anisotropic etching of the Si in the KOH bath

For alignment error  $300\mu\text{m}$  space is considered in the mask design. The sizes of back-etch holes are summation of all three factors, for instance for the case of the  $1\text{mm} \times 1\text{mm}$  membrane, type A, the back-etch hole size for X axes is (the axes which contains the springs):

$$1\text{mm} + (2 \times 210\mu\text{m}) + (2 \times 300\mu\text{m}) + (2 \times 255\mu\text{m}) = 2.530\text{mm}$$

In the Y axis there is not any spring (except for Type C membranes) therefore the size of the hole in this axes is:

$$1\text{mm} + (2 \times 300\mu\text{m}) + (2 \times 255\mu\text{m}) = 2.010\text{mm}$$

Therefore for Type A,  $1\text{mm} \times 1\text{mm}$  membrane, the size of the hole will be  $2.530\text{mm} \times 2.010\text{mm}$ .

The back-etch holes for membranes are shown in Figure 4.9.

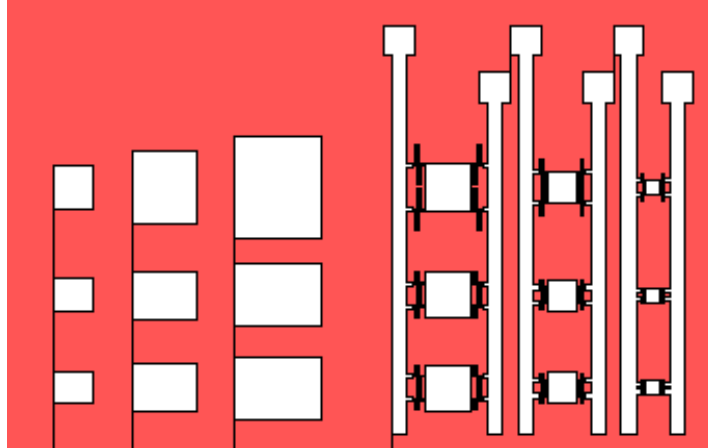


Figure 4.9: The backside mask for etching the backside holes

### **Lower electrodes' mask**

The lower electrodes will be fabricated on a separate glass substrate. They have a rectangular structure with the same size of their corresponding membranes. As shown in Figure 4.10 for each electrode one pad with electrical connection line to the electrode drawn in the mask.

### **Resistor Pattern for studying the electrical properties of electroplated copper**

For studying the electrical properties of the electroplated copper, a line with the length and width of 2.98 m, 100 $\mu$ m has been designed on the front side mask. The length of the resistor is calculated based on equation 4.2, supposing the value of same resistor with solid copper and thickness of the 5 $\mu$ m will be 100  $\Omega$ , which is large enough value to have low error in the study: [19]

$$R= \rho \times L/A \quad (4.2)$$

where  $\rho$  is the resistivity of metal,  $L$  is the length and  $A$  is the cross section area of the resistor.

The mask pattern for the resistor is shown in Figure 4.10.

The total mask structure is shown in Figure 4.11, the diameter of the circle is three inches as the sensors will be fabricated on the three inches wafers.

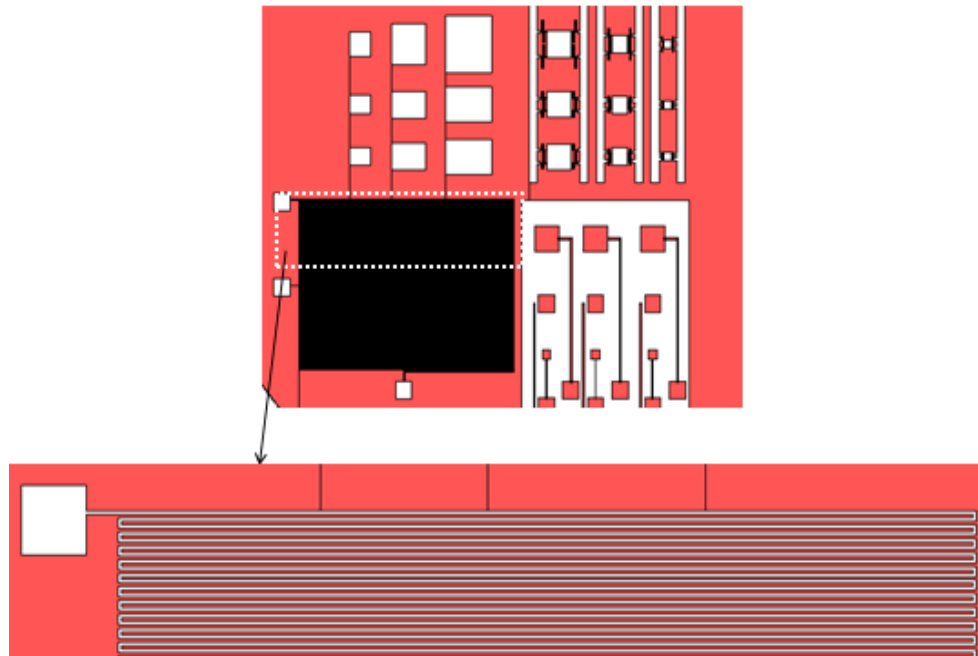


Figure 4.10: Mask for patterning of resistor

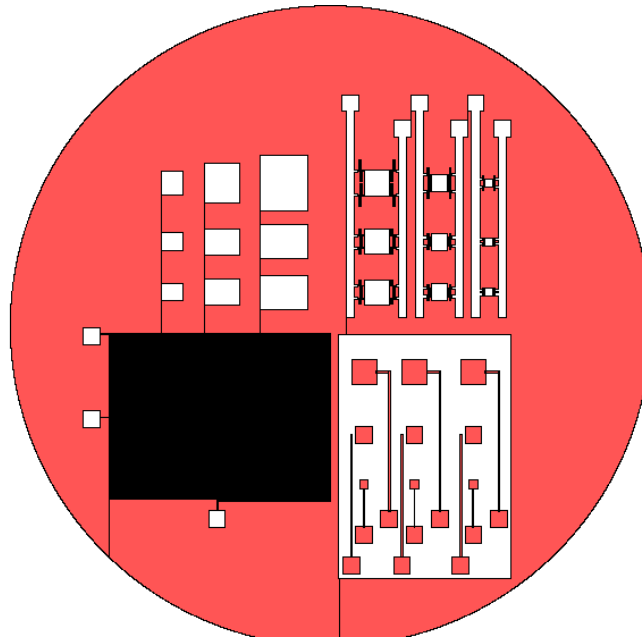


Figure 4.11: Mask for front and back sides patterning, a circle with diameter of three inches

### 4.1.3 Silicon wafer back etching process

In order to do the backside etching in KOH bath, first the backside nitride layer should be patterned and removed. HPR504 photoresist is used to pattern the backside of the wafer. The spinning of the photoresist has been done with 2700 rpm speed for 25 seconds. After that the wafer has been soft baked in 110 °C temperature for 60 seconds. The patterning has been done with exposure of UV light for 7 seconds and followed with developing in MF354 developer for 30 seconds. The thickness of the photoresist measured with alpha step system and the result was 1.5 $\mu\text{m}$ . After that the thickness of the silicon nitride layer has been measured with nanospec system, the results was 195nm. For removing the nitride layer from backside of the wafer, the wafer has been placed on the Trion Phantom II ICP/RIE plasma etcher (Figure 4.14). The plasma etching has been done by  $\text{CF}_4$  and

O<sub>2</sub> reactive gases under Pressure of 90 mTorr, ICP power of 300W, RIE power of 80W with gas mixture of 45 sccm CF<sub>4</sub> (Tetrafluoromethane) and 5 sccm of O<sub>2</sub>, for 100 seconds. After removing the silicon nitride from the patterned parts on the wafer the photoresist is removed from the surface of the wafer by using acetone followed by rinsing it with isopropanol.



Figure 4.12: ABM mask aligner optical lithography system



Figure 4.13: photresist spinner system



Figure 4.14: plasma etching system

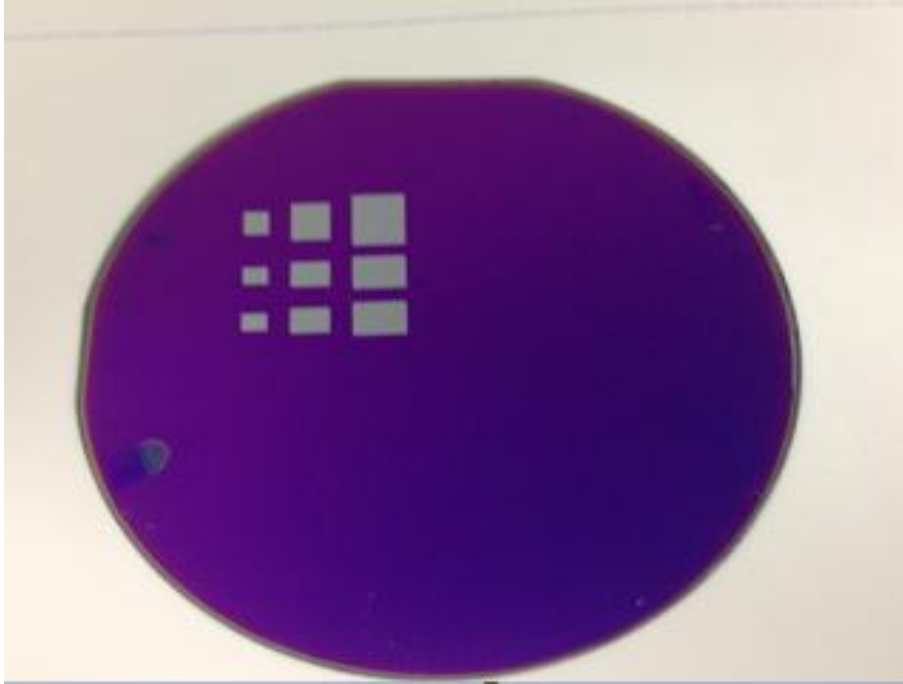


Figure 4.15: Etched nitride windows

Now the wafer is ready for being etched in the KOH bath. The etching will take place in areas with no protective nitride layer. For KOH etching an encapsulated system (Figure 4.16) was used. First the temperature of the KOH solution was warmed up to 80 °C by using a heater which was placed under the solution bath, after that the wafer was placed on a Teflon wafer holder. The Teflon wafer holder was placed in the KOH bath while a magnet spinner was used to stir the solution at speed of 120rpm in order to make the temperature and mixture of the solution even. In addition the spinner makes a flow toward the surface of the wafer. In order to have a control over the etching process, the wafer was taken out of the solution after 3 hours and placed in a beaker of DI water and after that rinsed with water for three times and dried by N<sub>2</sub> gun. The depth of the etched holes is measured with Tencor Alpha Step 500 surface profiler, the result was 205.4 μm. Dividing the etch depth by time of etching process calculated the etch rate as 1.138 μm/min, therefore the wafer was placed again in the solution in the same condition for 2

more hours. Because the thickness of the wafer was measured as  $385\ \mu\text{m}$  and after 5 hours of etching in total, based on the calculated etch rate  $35\ \mu\text{m}$  will be remained which is the desired thickness for doing the rest of sensor fabrication and releasing the final structure. After 2 hours the wafer was taken out and with the same process the etching stopped and the thickness of the remained diaphragm was measured as  $55\ \mu\text{m}$ . Therefore the last step of the KOH etching was done for 20 minutes and the thickness of the diaphragm after this step was  $33.5\ \mu\text{m}$ . (Figure 4.17)

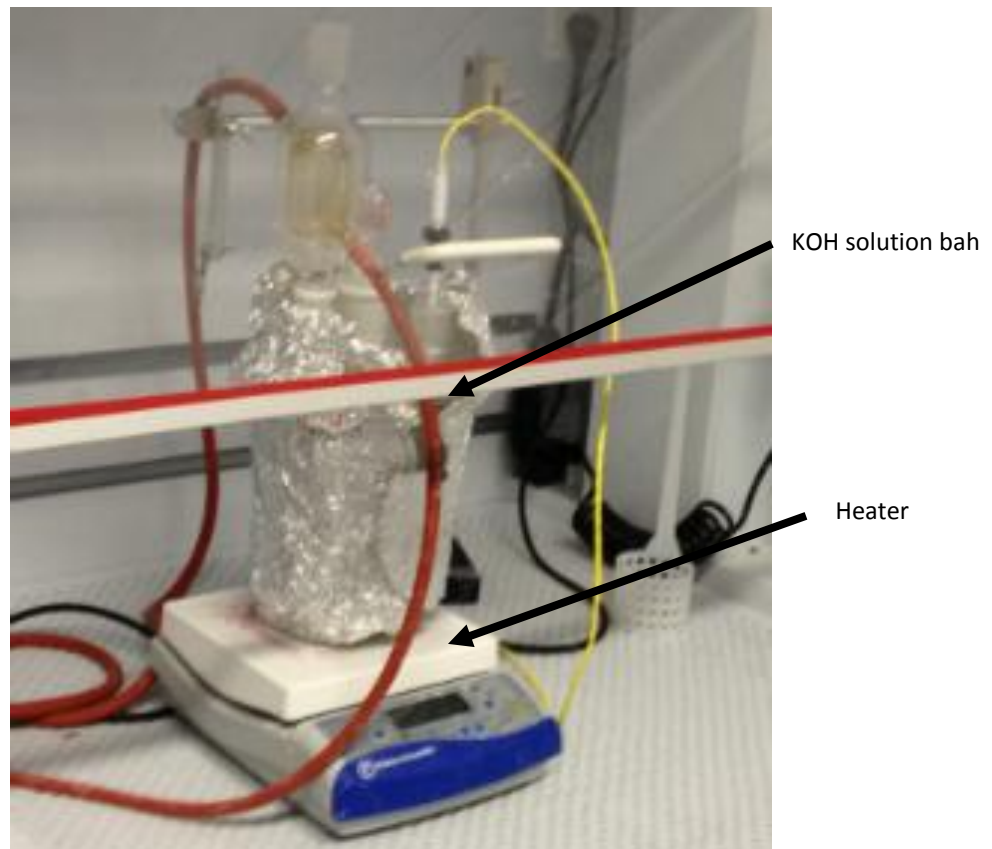


Figure 4.16: KOH etching setup

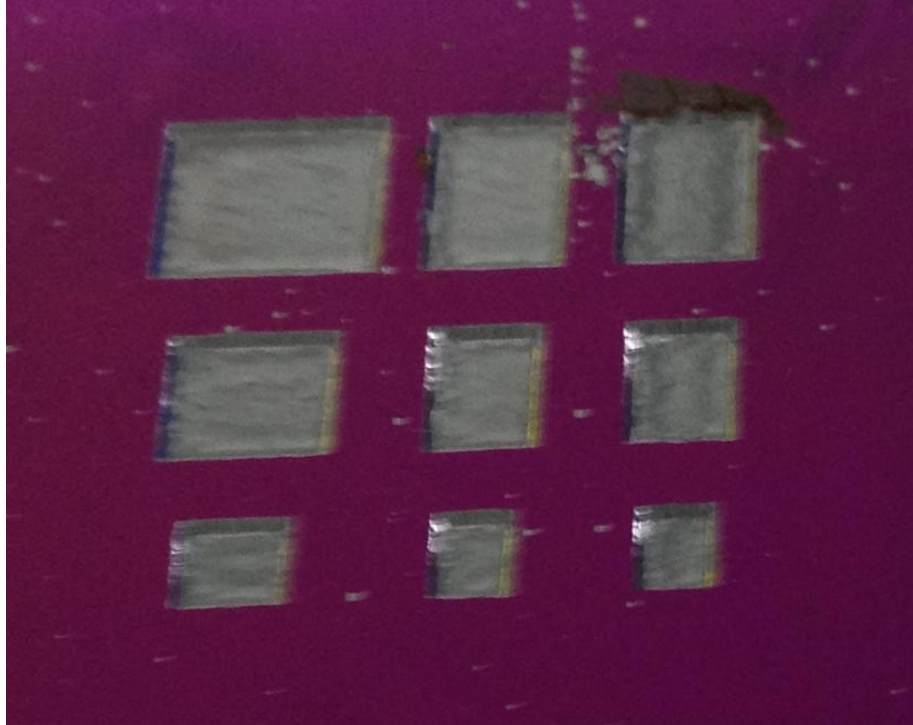


Figure 4.17: Etched holes in the silicon wafer

After back etching is done, before starting any other process the wafer should be cleaned from any contamination of the KOH solution. HCl removes ionic and metal particles left from KOH solutions. Therefore the wafer is cleaned in a piranha process. The process was done by using HCl : H<sub>2</sub>O 1:100, and placing the wafer in the solution for 5 minutes and after that rinsing it with DI water following by drying with N<sub>2</sub> gun.

#### **4.1.4 Frontside metallization**

In order to electroplate the copper membranes on the silicon wafer a seed layer of copper is needed prior to start the electroplating. Since it is not possible to sputter the copper directly on the silicone (it will dope the silicon and it has poor adhesion to silicon) an adhesion layer of titanium should be deposited first on the silicon wafer. Then copper

will be sputtered on the titanium adhesion layer. Before starting the sputtering the nitride layer should be removed from the silicon surface. The nitride etching is done with the plasma etcher system and the same recipe that has been mentioned in the back etching section.

After the nitride has been removed, the wafer is loaded in the MRC 8667 sputtering system and the system is pumped down to  $5.4 \times 10^{-6}$  mTorr. The dc sputtering of the titanium has been done in presence of the Ar gas with airflow of 45sccm with 200W dc power for 25 seconds in order to deposit 25nm of the titanium on the silicon wafer. This process is followed by sputtering of the copper in the same pressure with 45sccm of Ar gas under 200W dc power for 90 seconds, which will results in approximately sputtering of 210nm of copper on titanium.



Figure 4.18: MRC 8667 sputtering system

#### **4.1.5 Photoresist mold patterning for electroplating**

For copper electroplating with thickness of less than 5  $\mu\text{m}$  HPR504 photoresist could be used as a mold, by using lower spin speed during the spinning process. However, for electroplating thicker than 5 $\mu\text{m}$  conventional lithography methods such as using HPR504 is not appropriate. Therefore thicker resists should be used. SPR 220-7 photoresist is one of the thick resists available in our lab. For creating the photoresist mold both SPR 220-7 and HPR504 have been used to electroplate the membranes with different thicknesses.

## **SPR 220-7 Spinning Process**

For making the mold with thickness of 10 $\mu$ m and higher, Megaposit SPR 220-7.0 photoresist is used. It is a positive photoresist and adheres to copper surface very well and acceptable stability in the copper electroplating solution. Films as thick as 11  $\mu$ m can be made with this photoresist in a single spin and with good uniformity. The lithography process is shown:

1. Spin for 30 seconds at 1500 rpm with a 5 second acceleration time.
2. Softbake for 90 seconds at 115°C and with a 90 second ramp.
3. Exposure for 30 second using i-line ABM mask aligner. Several shorter exposure times were tried, but after the developing step a thin layer of photoresist still remained on the substrate surface, and so 30 seconds was used.
4. Leave the sample in the air for at least 4-5 hours to absorb humidity.
5. Post exposure bake for 30 seconds at 90 °C, this step is very short because the photoresist layer is thick and for trials of 2 minutes and more, the photoresist was cracked.
6. Developing for 4 minutes using 354 developer (sodium hydroxide solution) in two steps, each step for 2 minutes. Sample was rinsed with water between the two developing steps.

The thickness of the resist mold measured with Tencor Alpha Step 500 surface profiler and the results was 10.7 $\mu$ m.

This lithography process has been done several times successfully but due to the expired photoresist (expired in 2011), sometimes the same recipe for creating the mold was not successful and during the developing process some resists were still on the wafer surface. In addition sometimes after the post exposure bake and starting the developing, large cracks were appearing in the surface of the resist mold and the cracked parts were immediately peeled off from the surface of the wafer. This lithography process was done successfully several times. But due to the high chance of failure during electroplating or developing as well as low rate of repeatability, for the final devices it was decided to use a more repeatable method of lithography. There HPR 504 photoresist was used to make thinner molds for electroplating of thinner copper.

#### **HPR 504 Spinning Process**

HPR 504 photoresist was used to make the mold for the 5 $\mu$ m thick copper plating. The process was as follows

1. Spin for 30 seconds at 1500 rpm with a 5 second acceleration time.
2. Softbake for 60 seconds at 110°C.
3. Exposure for 10 second using i-line ABM mask aligner.
4. Developing for 60 seconds, using 354 Developer.

Thickness of the resist mold was measured with Tencor Alpha Step 500 surface profiler and the result was 2.9 $\mu$ m.

## 4.2 Membrane electroplating process

### 4.2.1 Membrane electroplating process design

1- The copper is electroplated to the mold in order to create the sensor structure and the resist mold is removed with acetone.

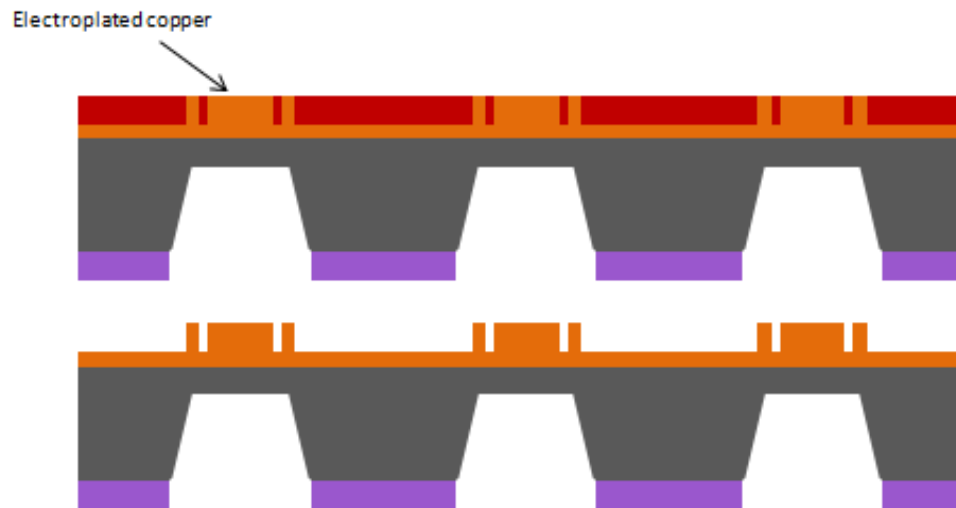


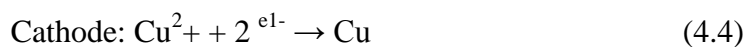
Figure 4.19: Electroplating of the copper into the photoresist mold

### 4.2.2 Theory

Copper electroplating is one of the oldest, protective and decorative metallic coating for steel and other basis metals. However in recent years it has found more high tech applications such as interconnection of printed circuit boards (PCBs) and ultra large scale integration (ULSI) [33]. Using of the copper electroplating in fabrication of microstructures, specifically devices with high aspect ratios, such as micro heat flux sensors, MEMS devices and micro channel heat sinks [34-36] is frequently reported. Electroplating is a process that uses electrical current to reduce dissolved metal cations in solution in order to make a metal coating on an electrode. The process which is used in

electroplating is called electrodeposition. The set up of electroplating system consists of a power supply, two electrodes and an electroplating bath which contains an electrolyte. The electrode that will be plated is the cathode of the circuit and the anode is an electrode made of the metal to be plated. Both electrodes are in a solution which called an electrolyte. It contains dissolved metal salts as well as other ions that permit the flow of electric current. The power supply applies a positive voltage to the anode, oxidizing the metal atoms and allowing them to dissolve in the solution. At the cathode, the dissolved metal ions in the electrolyte will be reduced and they will be deposited on the cathode. Figure 4.20 is showing the schematic of an electroplating bath. A positive voltage is applied to the pure copper source (anode) to provide the copper cations into the solution. These cations move toward the negative electrode (cathode) through the solution and when reached to the cathode will be reduced and deposited on it.

Here is the summary of the reactions in anode and cathode:



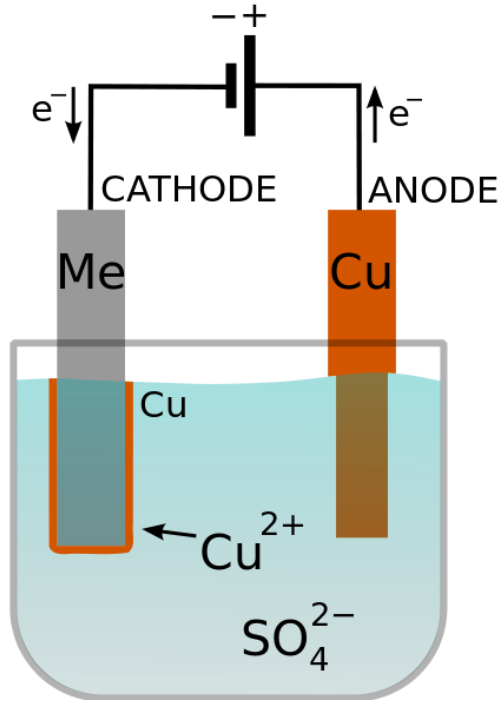


Figure 4.20: The schematic of an electroplating bath for copper plating [37]

Figure 4.21 shows the profile of the concentration of the ions in the electrolyte during electroplating. where  $L$  is half of the distance between cathode and anode. The current density of  $i=i(t)$  is assumed to be carried by a single type of carrier in which its local time-dependent concentration between the electrodes is  $c(z,t)$ . The model is described by the diffusion of carriers:

$$\frac{\partial c}{\partial t} = D \frac{\partial^2 c}{\partial z^2} \quad (4.5)$$

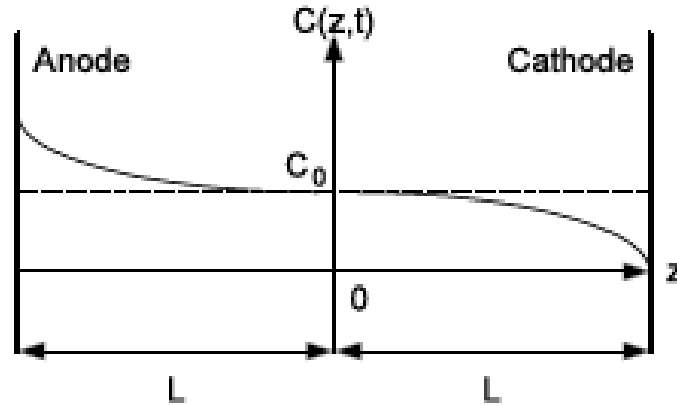


Figure 4.21: The profile of current density between electrodes in the simple electrolytic cell [38]

There are two current components which are making the total electric current density. The local density imbalance of carriers which produces a net diffusion current and drift of carriers, which is resulting from the local electric field. By adding these two components together a model for the current density can be defined which is like the current density model for the semiconductors: [38]

$$i = -nFD \frac{\partial C}{\partial z} + \mu q n C E \quad (4.6)$$

where  $n$  stands for the valence of ions,  $F$  is the Faraday constant,  $D$  is the diffusion constant,  $E$  is the electric field,  $\mu$  is the mobility of ions, and  $q$  is the unit electronic charge. After placing the electrode into solution two parallel layers of ions will form on surface of it which is called electrical double layer [39];

- 1- A layer of surface charge on the surface of the electrode
- 2- A layer consists of the free ions with opposite charge gathered in the liquid very close to the electrode surface

Because the net charges of these two layers are equal the total charge of the double layer structure is neutral and the result is having:

- 1- Two layers of charge (the double layer)
- 2- Potential drop which is confined to double layer region

Since the electrode double layer has charged ions with opposite polarity, they scatter the charged carriers through coulomb collisions which results in domination of the diffusion transport near the electrodes. In the other words the electrode double layer reduces the mobility of carriers considerably; therefore we can assume that the drift term is about zero near the electrodes [40]. In order to have electroplated copper layer with higher quality it is important to reduce the thickness of the electrode diffusion double layer, because due to low ion transport velocity, there is lack of ions at the cathode and the electrode diffusion layer limits the rate of carrier transport which has a negative effect on the properties of the deposited layer.

Several methods are suggested for reducing the diffusion double layer thickness, such as stirring the solution constantly, using ac sinusoidal voltage instead of a dc voltage with an offset value, using pulsed signal voltages with a non-zero average and a frequency between several tens of Hertz and hundreds of kilo Hertz.

In the presented work we employed the pulse signal plating for copper electroplating. Pulse plating has a lot of applications in: plating of alloys, thin films platings, decorative coatings [41-43]. Most of the previous pulse plating works reported the improvement of the plated copper in terms of the hardness and quality after using pulse plating. Pulse reverse current electroplating is one of pulsed plating methods, which is frequently used for thick copper plating [44-46]. In this method current will be used for controlling of the

electroplating process. The benefit of using current rather than voltage is that since current is linearly proportional to the number of deposited ions, by monitoring the current it is much easier to control the transferred mass, while the current which passes through the anode and cathode is very sensitive to the applied voltage and the I-V characteristic of the electroplating solution is highly nonlinear. Therefore monitoring the electroplating process with current instead of using voltage is much more reliable. However, even for the current pulses several parameters such as period (or frequency), forward current amplitude, reverse current amplitude, average current should be optimized to get the best quality of the electroplated copper and having control over the electroplating process. Figure 4.22 shows a typical waveform which can be used as input current signal pulse for electroplating. T in the figure below is corresponding for the period of the signal,  $T_f$  and  $T_r$  are the forward and reverse times,  $I_f$  and  $I_r$  are forward and reverse current amplitudes and  $I_{av}$  is the average current which passes through the electroplating bath.

$$T = 1/f = T_f + T_r \quad (4.7)$$

$$\text{Duty cycle} = T_f / T \quad (4.8)$$

$$IP-P = I_f + I_r \quad (4.9)$$

$$I_{av} = (I_f T_f - I_r T_r) / (T_f + T_r) \quad (4.10)$$

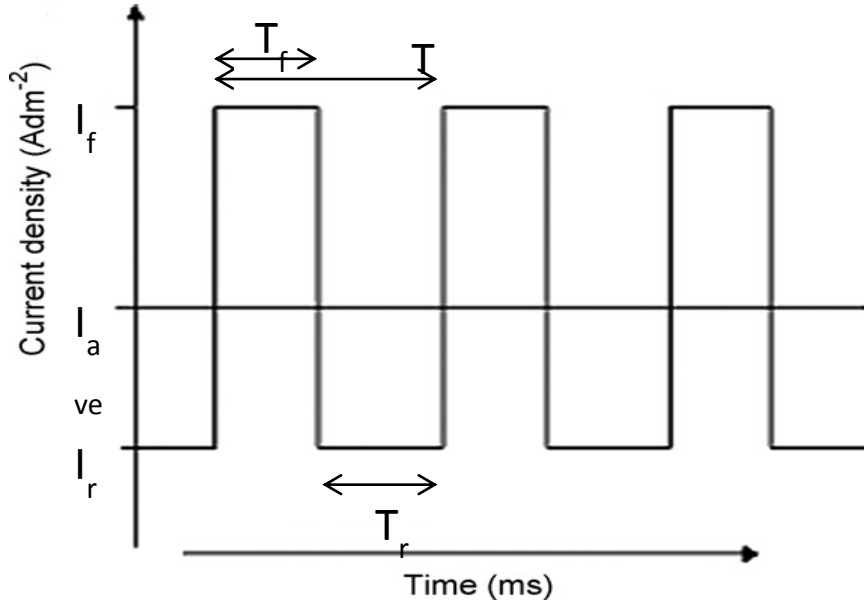


Figure 4.22: pulsed current waveform and the parameters

### 4.2.3 Experimental electroplating

The set up of the electroplating system is shown in Figure 4.24 the system consists of a large bath containing the electroplating solution, a sample holder for keeping the sample fixed in the solution during the electroplating process and making the electrical contact between the current source and sample, electroplating power source which is capable of generating currents pulses with different amplitudes and frequencies, a plunger for making the electroplated copper smoother and a power supply for the mechanical plunger. In this set up the cathode is the sample which is in the sample holder and connected to the negative output of the electroplating power supply via sample holder. By connecting the positive side of the electroplating power supply to the plunger; the circuit will be closed between the sample (cathode) and the plunger (anode) via the solution. For starting the electroplating process it is necessary to prepare the electroplating solution. The name of the acid copper electrolyte is Technic CU-2800 which is bought from

Technic Company. The process of preparing the electrolyte solution is available in appendix 1, from the data sheet which is provided by the company. After preparing the proper electroplating solution, now it is the time to prepare the electroplating setup for the process. The first step is to put the sample in the sample holder. There are 3 thick wires for holding the sample during the electroplating process. These wires also provide the electrical connection to the power supply during the plating process. As shown in Figure 4.23, the sample is placed in the sample holder and the thick wires are connected to the top metalized side of the sample. The electrical connection to the sample holder's screw should be checked with an ohm meter. By turning the power supplies of the electroplating system on, a mechanical pump starts to make a flow in the solution which makes the bath's solution more even during the plating (Before starting the electroplating always the pump should run for 10 minutes in order to make sure that the solution is even enough). The next step is to set the current pulse parameters on the electroplating power supply.

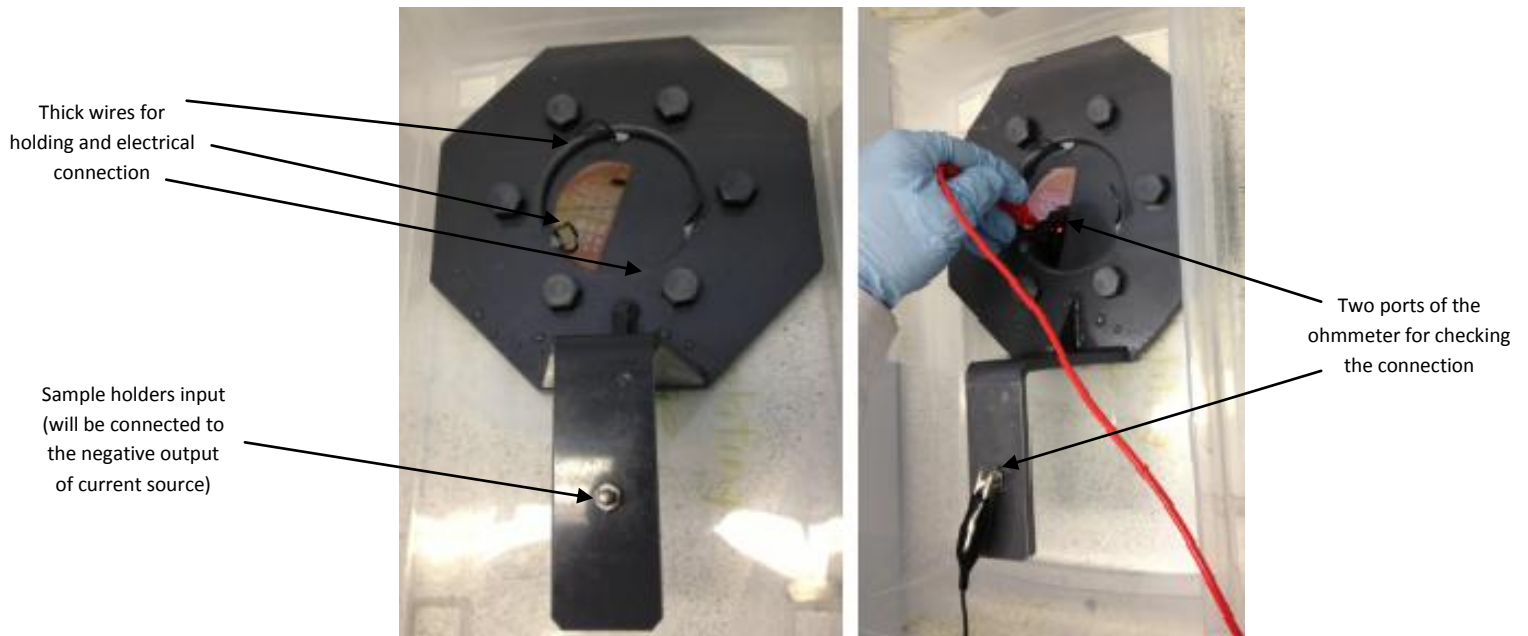


Figure 4.23: Checking the electrical connectivity between sample holder and sample

The electroplating process will start by placing the sample holder in the electroplating solution bath and connecting the negative output of the current pulse generator to the sample holder and the positive output to the plunger. The last step is to turn on the power supply of the mechanical plunger on, to make it run during the electroplating process. The role of the mechanical plunger is to make the plated films smoother, this happens by using of a micro fiber cloth which covers the top surface of the plunger. It is important to preset the position of the plunger such that in its lowest position the microfibers just touch the surface of the sample and this will help to put the copper ions into the very narrow patterns of the photo resist mold.

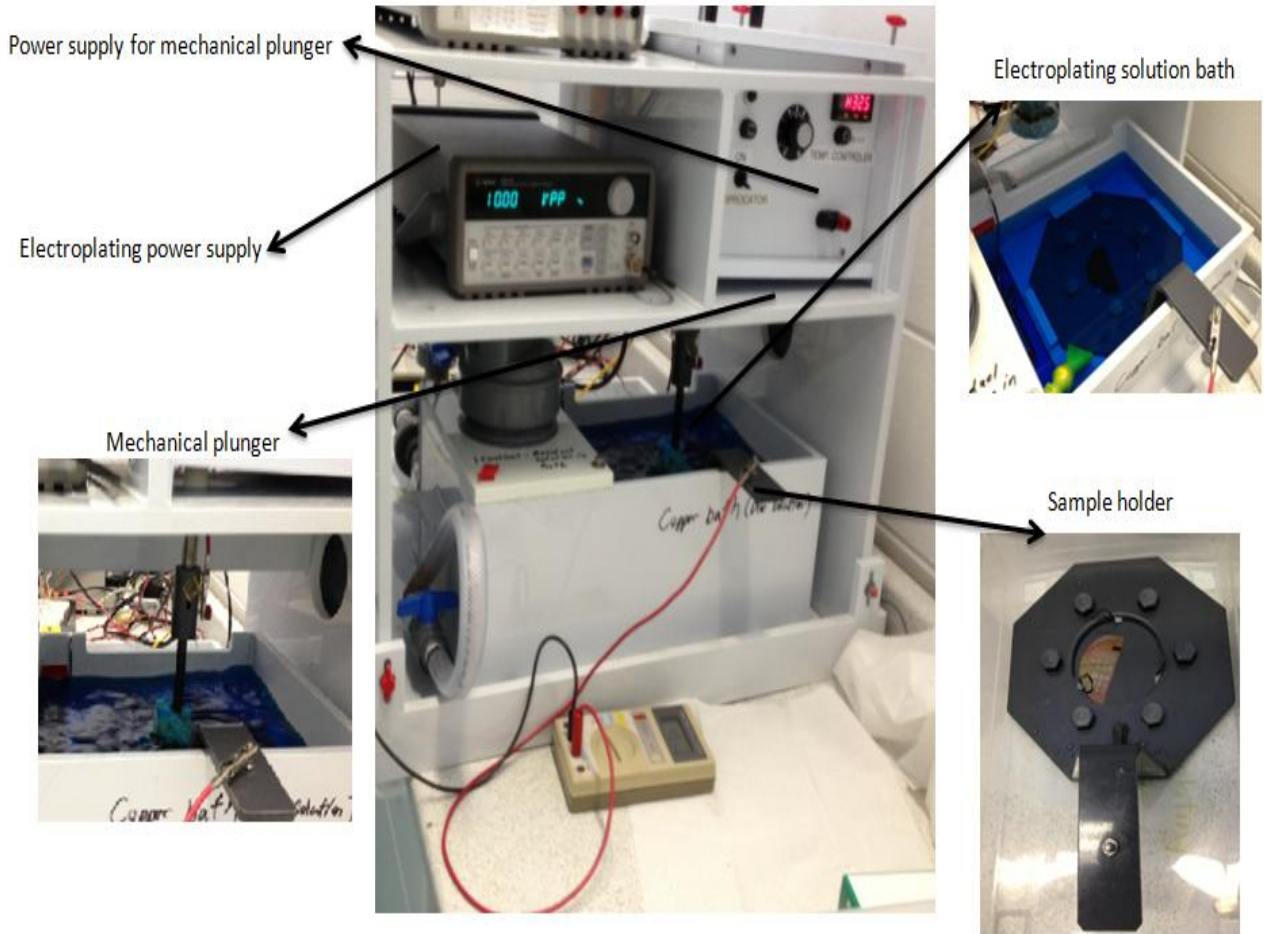


Figure 4.24: Electroplating setup

After setting up the electroplating system, the important step is to optimize the input current pulse signal parameters. Three parameters should be optimized for the electroplating:

- 1-amplitudes of the forward and reverse currents
- 2-duty cycle
- 3-frequency

For optimizing the electroplating parameters, 2cm x 2cm samples of glass have been used which the same copper seed layer was sputtered on them as explained in the frontside metallization section. From the previously electroplating project done in our group, by Motieifar, was found that the frequency of 1 kHz, for the input current pulse, compared to 100 Hz and 10 kHz will results in a higher quality films. Therefore the signal frequency in all of the experiments kept as 1 kHz. Trials with different forward and reverse current and duty cycle applied to the electroplating system to find out the optimum values for these parameters. After the electroplating was done, the average roughness over the surface of each sample measured. In the Table 4-2 Ra indicates the average roughness of the surface over the length (the arithmetic average deviation of the absolute values of the roughness profile from the mean line) that the measurement has been done. The ratio of the average roughness to the thickness of the electroplated copper has been used as a factor to optimize the electroplating parameters. Several samples were plated with the forward current of 20 mA and lower but they were not successful and after 10 minutes there was not any consistent plated film of the samples. Also the lowest thickness over average roughness ratio for the samples which were plated with 400 mA and higher found to be more than 8%, therefore the forward currents in the range of the 26 mA to 208 mA were tested to find the optimum values. As can be seen in the Table 4-2, the electroplating factor for current forward current of 52 mA and reverse current of 68 mA has the best (lowest), Ra to thickness ratio. In all of the experiments we can see that as the duty cycle goes higher the quality gets better. After the first optimized parameters were found now it was the time to do more experiments to optimize the parameters more effectively.

Table 4-1: Pulsed current electroplating recipes and results

	$I_f$ (mA)	$I_r$ (mA)	$T_f$ (msec)	$T_r$ (msec)	Duty cycle	Time (min)	Thickness (nm)	$I_{ave}$ (mA)	Ra(nm)	Factor (Th/Ra)
1	26	34	0.6	0.4	60%	10	-----	2	-----	-----
	26	34	0.7	0.3	70%	10	185	8	11.4	6.21%
	26	34	0.8	0.2	80%	10	332	14.3	18.0	5.43%
	26	34	0.9	0.1	90%	10	390	20	18.3	4.69%
2	52	68	0.6	0.4	60%	10	-----	4	-----	-----
	52	68	0.7	0.3	70%	10	386	16	13.7	3.54%
	52	68	0.8	0.2	80%	10	685	29.6	20.6	3.00%
	52	68	0.9	0.1	90%	10	880	40	23.1	2.62%
3	104	136	0.6	0.4	60%	10	205	8	12.0	5.87%
	104	136	0.7	0.3	70%	10	780	32	38.5	4.94%
	104	136	0.8	0.2	80%	10	1405	59.4	57.8	4.12%
	104	136	0.9	0.1	90%	10	1860	80	71.9	3.87%
4	208	272	0.6	0.4	60%	10	355	16	21.4	6.05%
	208	272	0.7	0.3	70%	10	1374	64	71.1	5.17%
	208	272	0.8	0.2	80%	10	2420	118.8	104.8	4.33%
	208	272	0.9	0.1	90%	10	3150	160	120.9	3.84%

#### 4.2.4 Periodic Pulse Reverse current plating

By adding an off time period between the forward biased pulse and reverse biased pulse, new waveform will form as shown in Figure 4.25. This technique is called periodic pulse reverse current plating (PPR). The reason for adding this off time period to allow the ion concentration in the plating bath to distribute more evenly after forward deposition,

because during both of these processes the ion concentration is higher in areas that the process is already takes place and this will increase the roughness in the surface of the electroplated film. Figure 4.25 illustrates an application of this method in filling of vias with electroplated copper.

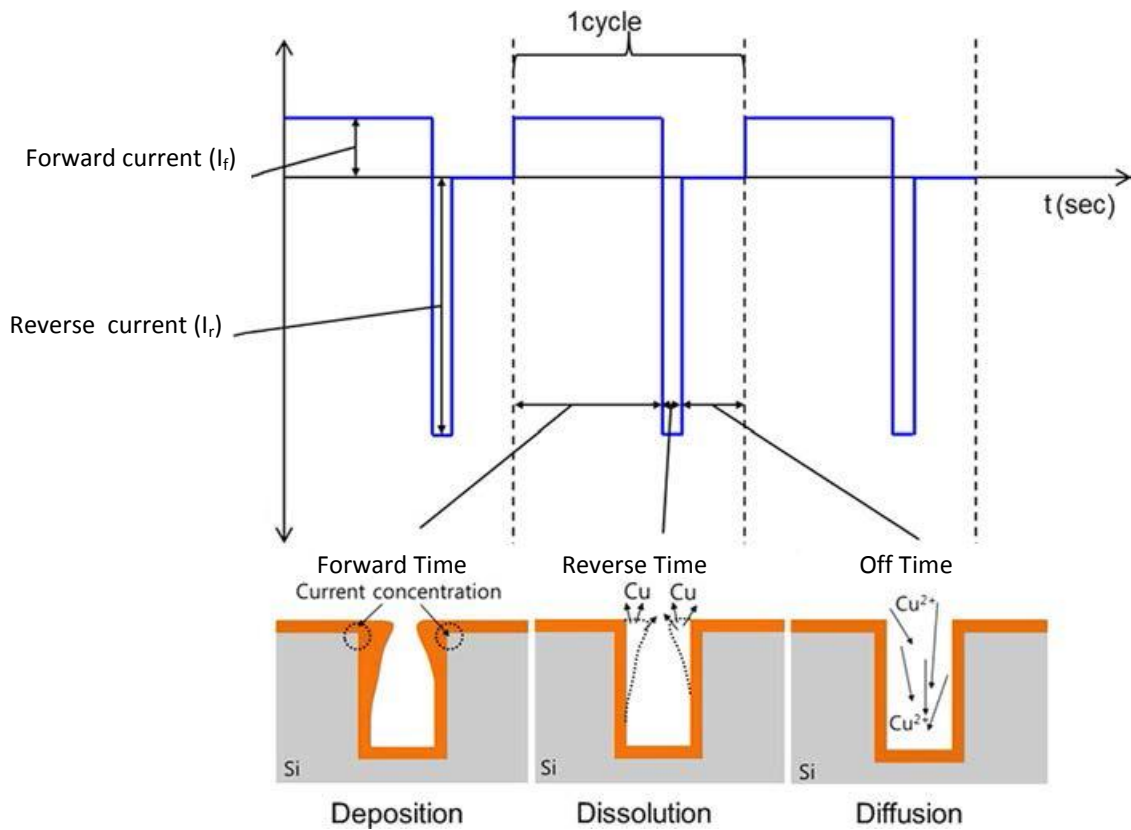


Figure 4.25: periodic pulse reverse current plating for via filling [33]

In order to study the effect of the off time period, a new current waveform is used (Figure 5.26). Several samples with different waveform characteristics have been electroplated. Values of 52mA for forward current and 68mA for reverse current with duty cycle of 90% used for these samples. The current source of the electroplating system has the capability of applying forward current period, reverse current period as well as applying

forward and reverse off periods. waveform characteristics as well as the results of the electroplating experiments are shown Table 4-3.

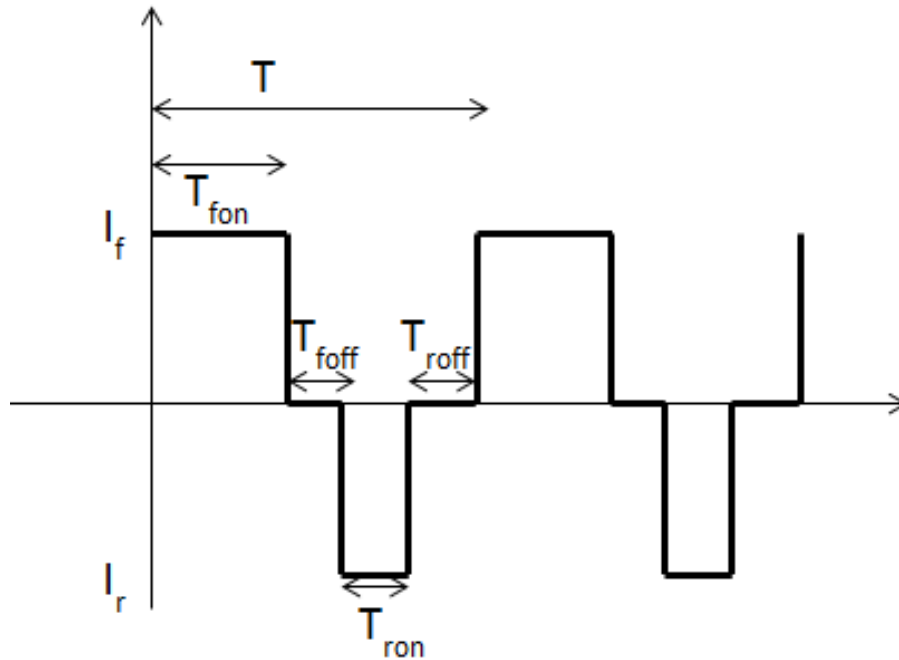


Figure 4.26: periodic pulse reverse current plating waveform

Table 4-2: electroplating recipes and results for periodic pulse reverse current plating

Sample	$T_{fon}$ (msec)	$T_{foff}$ (msec)	Forward Duration (msec)	$T_{ron}$ (msec)	$T_{roff}$ (msec)	Reverse Duration (msec)	$I_f$ (mA)	$I_r$ (mA)	Time (min)	Factor (Th/Ra)
1	0.9	0	0.9	0.1	0	0.1	52	68	10	2.62%
2	0.35	0.1	0.9	0.1	0	0.1	52	68	10	3.38%
3	0.23	0.1	0.9	0.1	0	0.1	52	68	10	4.2%

As shown in table 4-3 there is not that much of difference in the quality of the plated copper by adding the off time current. A small difference is shown for the case of sample 2 which seems to have higher quality, but using this parameter in the plating might be optional as will not make a significant improvement in the quality of the plated copper and also reduces the electroplating rate.

#### 4.2.5 Electroplating of copper Membranes

When it came time to fabricate electroplated membranes, the current pulse generator of the electroplating system failed. Therefore, an external voltage source was used for the electroplating. A dc voltage source has been used for driving the current to the electroplating solution. The circuit of Figure 4.27 was used for dc plating. First of all the voltage vs current characteristics of the circuit studied by doing the same experiments on the  $2 \times 2 \text{ cm}^2$  copper coated samples and the results are shown in Table 4-4.

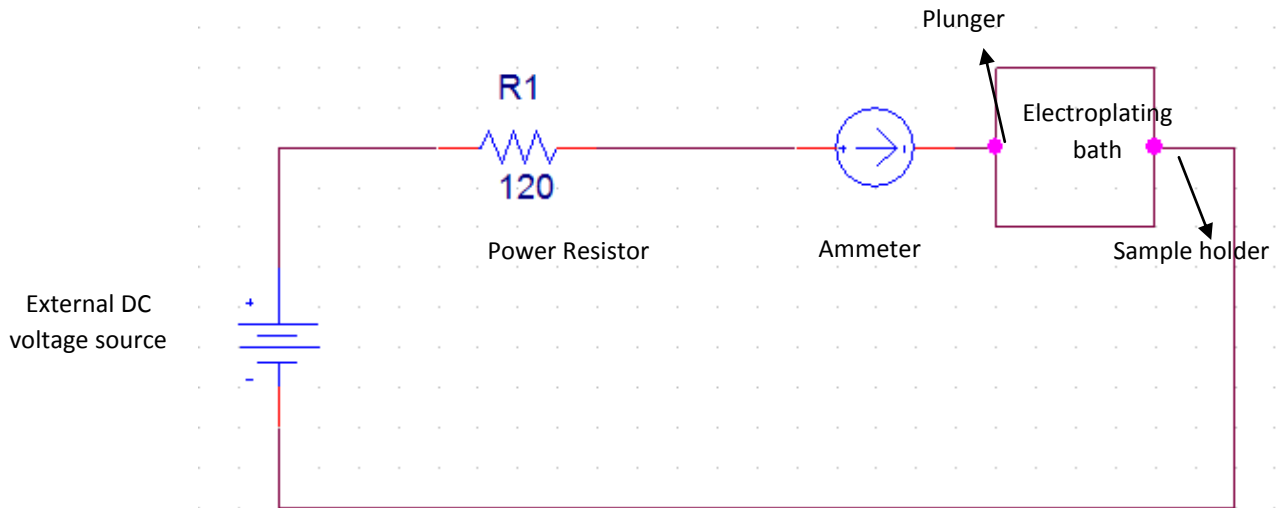


Figure 4.27: Schematic of the circuit used for dc plating

Table 4-4-3: The Voltage-current characteristics of the electroplating solution

Voltage (V)	Current (mA)
1	2.2
2	5.1
3	13.3
4	22.1
5	32.2
8	61
10	80
12	102
15	133

### **Electroplated membranes with dc voltage**

From the values of Table 4-4, the electroplating voltage should be selected such that the current is as close as possible to the optimum values which were found with the current pulse plating system. Therefore the constant dc voltage of 7.5 V was chosen. The first set of the dc electroplated membranes were fabricated and the thickness and roughness of the electroplate copper was measured. The results are shown in Table 4-5. In Figure 4.28-4.30 the images of the several membranes with different thicknesses are shown. The copper features shown in Figure 4.31 increases the roughness of the surface of the electroplated copper. This will result in having copper films with lower quality and higher stress. A possible way for removing these particles from the membrane's surface

is using pulse electroplating which in the negative pulse width will etch these particles which have a weaker bonding to the copper surface.

Table 4-4: Recipes and results for dc plated membranes

Sample number	Thickness	Membrane roughness(Ra)	Spring roughness (Ra)	Average Current	Time
1	0.5 $\mu$ m	7.1nm	10.8nm	53mA	5min
2	1.1 $\mu$ m	13.3nm	18.3nm	53mA	10min
3	1.6 $\mu$ m	24.1nm	31.3nm	53mA	15min
4	2.7 $\mu$ m	37.4nm	40.6nm	53mA	25min
5	4.02 $\mu$ m	42.8nm	48.8nm	53mA	40min

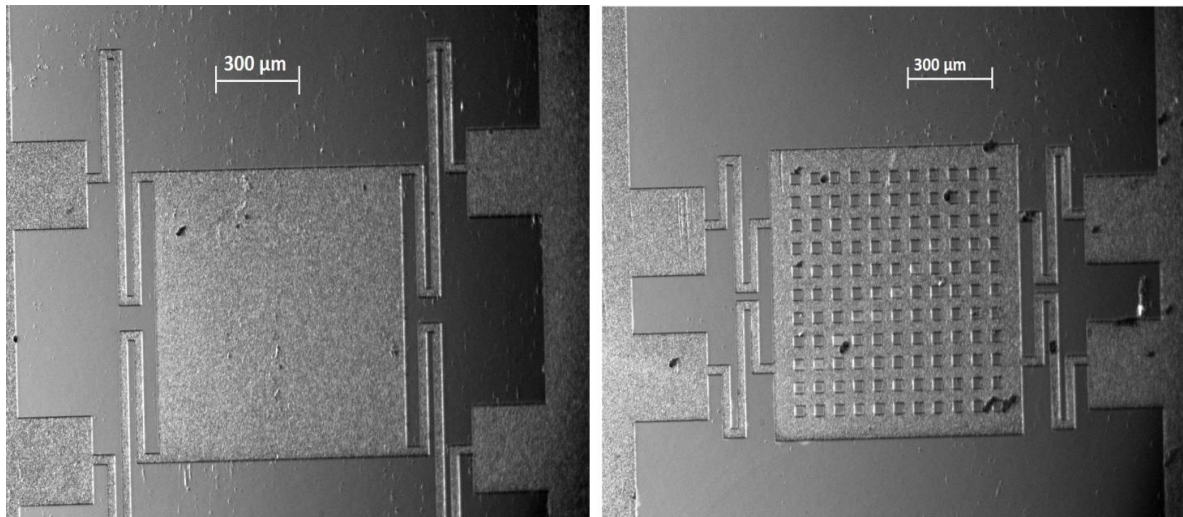


Figure 4.28: Electroplated membranes with Thickness of 0.5 $\mu$ m

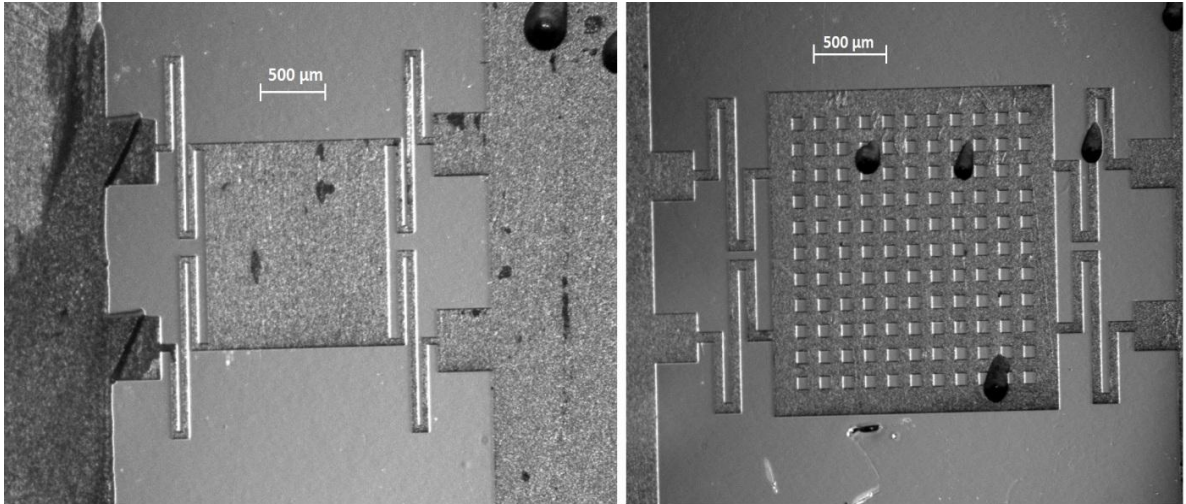


Figure 4.29: Electroplated membranes with Thickness of  $2.7\mu\text{m}$

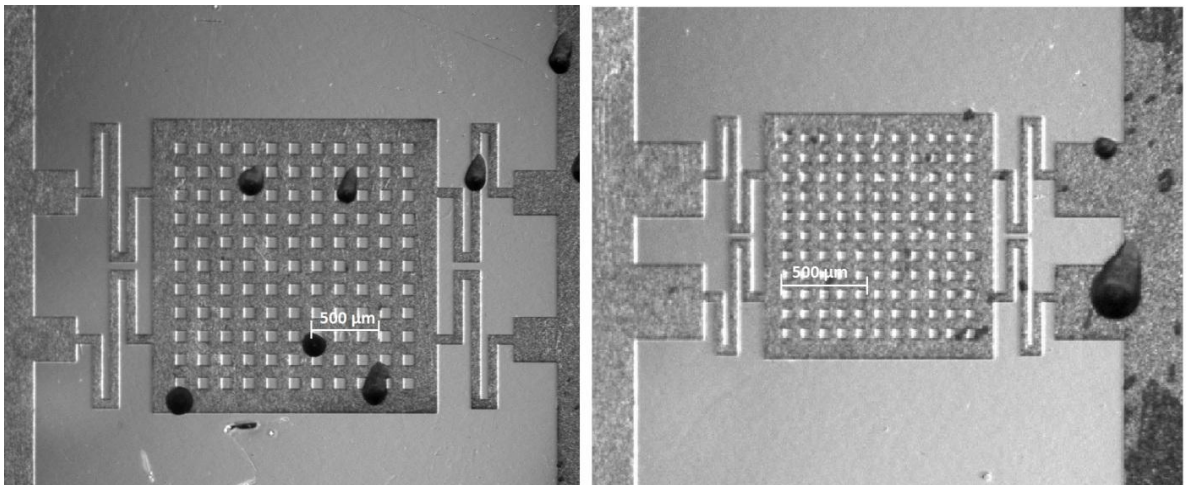


Figure 4.30: Electroplated membranes with Thickness of  $4.02\mu\text{m}$

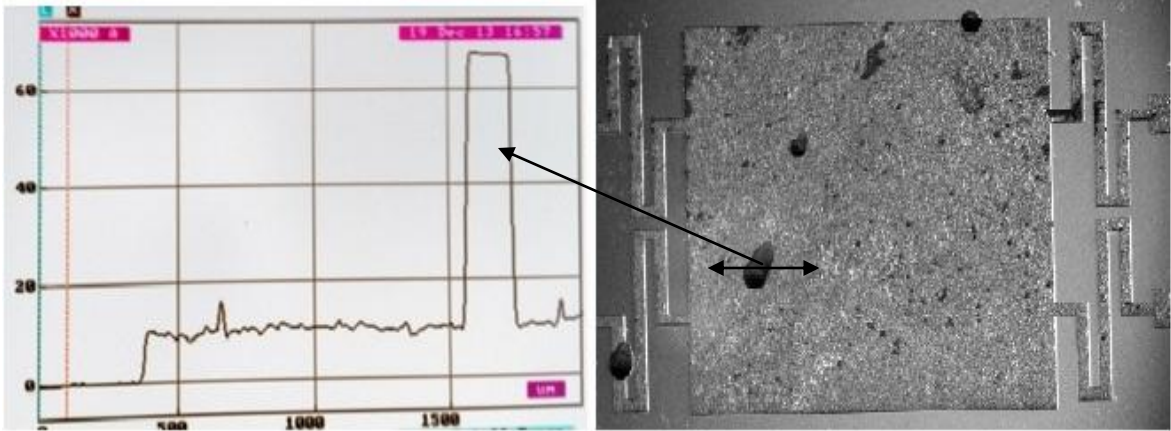


Figure 4.31: Large plated particles with thickness of more than  $6\mu\text{m}$

### Pulse plated membranes

For pulse plating the circuit of Figure 4.32 was used. Since the amplitude of the output voltage and the output current of the signal generator were not large enough, two op-amps were used before connecting the voltage signal to the electroplating bath;

- 1- A LM741 op-amp with gain of 3 to provide the output voltage between -15V and 15V.
- 2- A TDA2030 power amplifier which is used as a buffer to provide large enough output current.

The pulse characteristics have been used such that being as close as possible to the optimized parameters which were found in the Table 4-2. Therefore a pulse voltage with  $V_f = 7.5\text{V}$ ,  $V_r = 8.5\text{V}$  (a pulse with amplitude of 8V and a -0.5V offset voltage) and duty cycle of 80% has been used to for the electroplating. Several membranes have been plated for different times and the results were as shown in Table 4-6. In Figure 4.33-4.36 different membranes which were plated by pulse voltage are shown. As shown in the

figures the copper features which used to be on the surface of the dc plated membranes were no longer deposited on the membranes which are plated with pulse voltage signals.

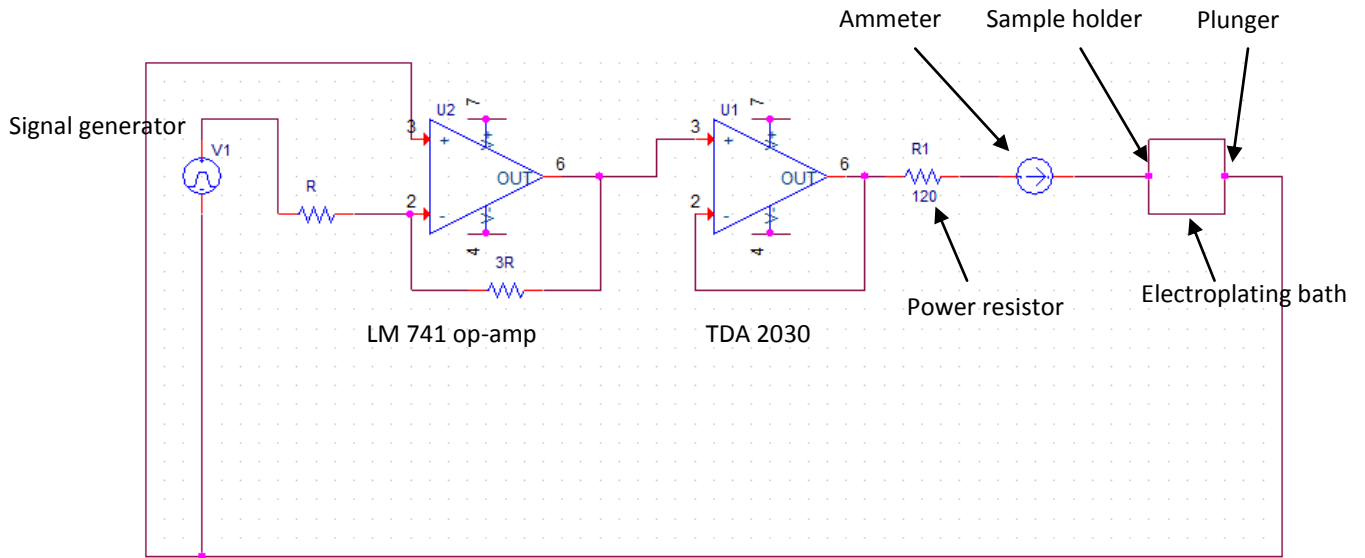


Figure 4.32: Schematic of the circuit used for Pulsed shaped plating

Table 4-5: Recipes and results for pulse plated membranes

Sample number	Thickness	Membrane roughness	Spring roughness	Average Current	Time
1	0.48 $\mu$ m	8.6nm	11.2nm	42mA	5min
2	0.96 $\mu$ m	17.3nm	24.4nm	42mA	10 min
3	2.58 $\mu$ m	33.3nm	38.6nm	42mA	25 min
4	3.21 $\mu$ m	38.7nm	41.3nm	42mA	35min
5	4.11 $\mu$ m	45.9	52.7nm	42mA	45min

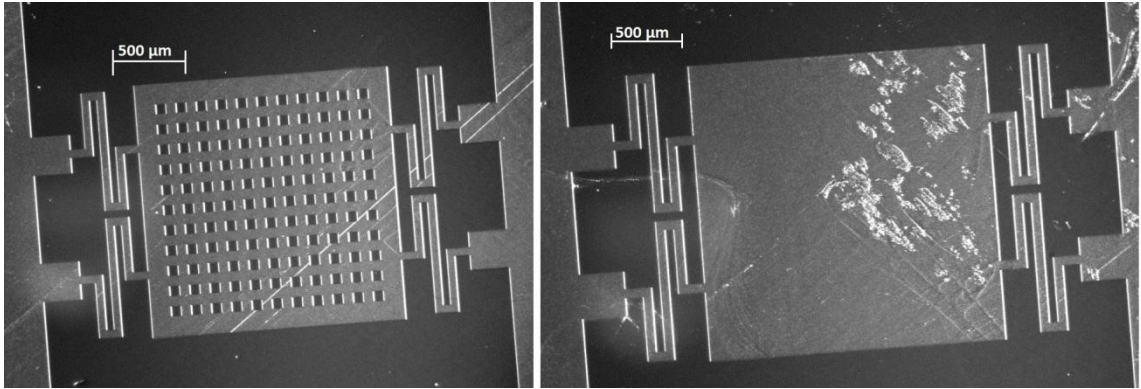


Figure 4.33: Electroplated membranes with Thickness of 1  $\mu\text{m}$

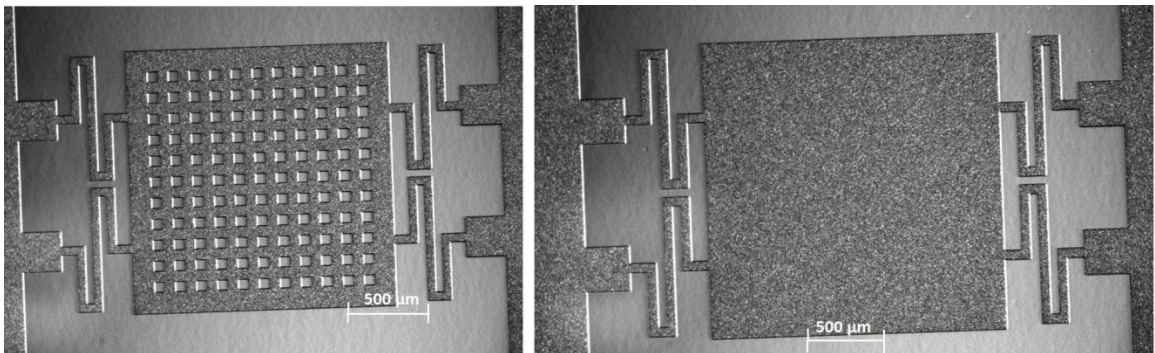


Figure 4.34: Electroplated membranes with Thickness of 2.6  $\mu\text{m}$

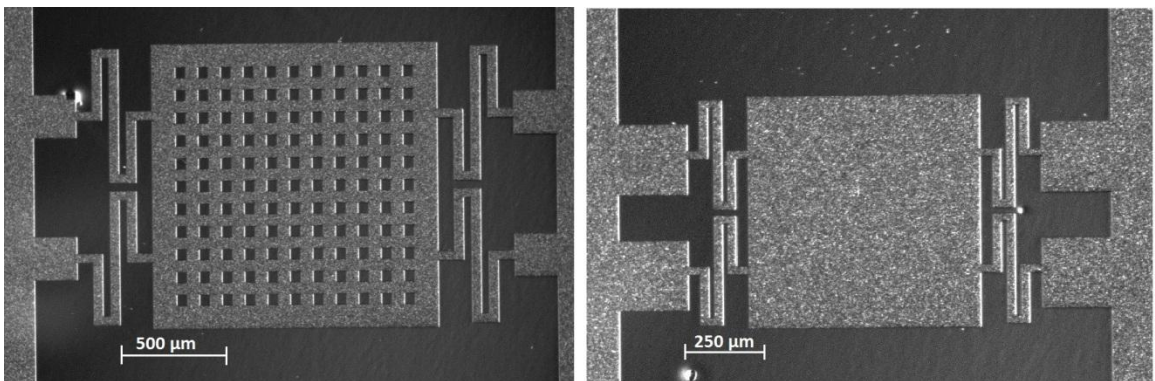


Figure 4.35: Electroplated membranes with Thickness of 3.3  $\mu\text{m}$

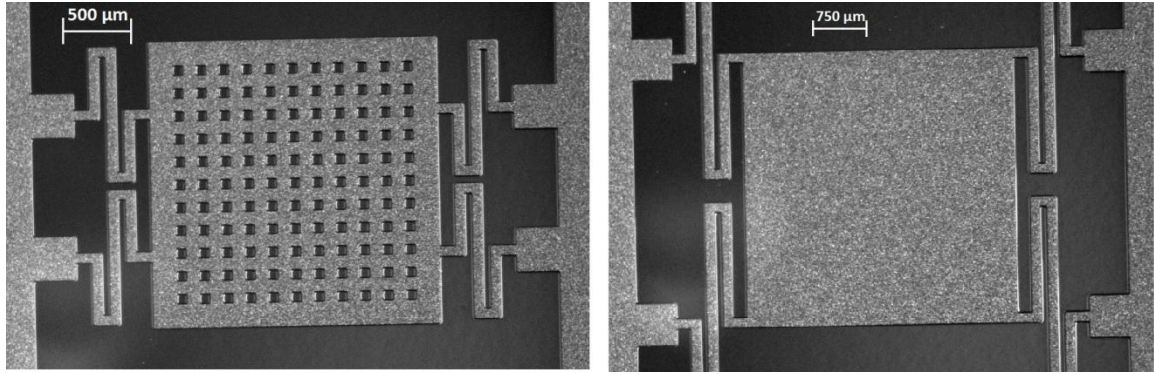


Figure 4.36: Electroplated membranes with Thickness of  $4.2\mu\text{m}$

#### **4.2.5 Surface Roughness Analyses on the copper electroplated structure**

As shown in Figure 4.38 the thickness of the electroplated copper is measured for different features sizes (springs and membranes) to see the effect of the width of each part on the thickness of the electroplate copper, the results are shown in Figures 4.39 and 4.40. Also from the same results the effect of the flow direction on the thickness of the electroplated copper can be studied. The same set of measurements was done on of the dc plated membranes to compare the results.

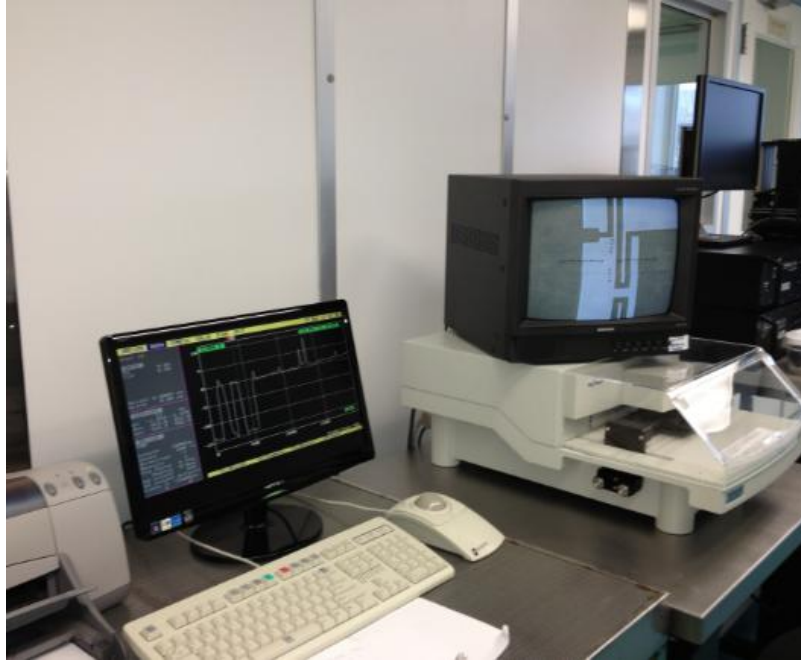


Figure 4.37: Tencor Alpha Step 500 surface profiler, scanning the surface of plated samples

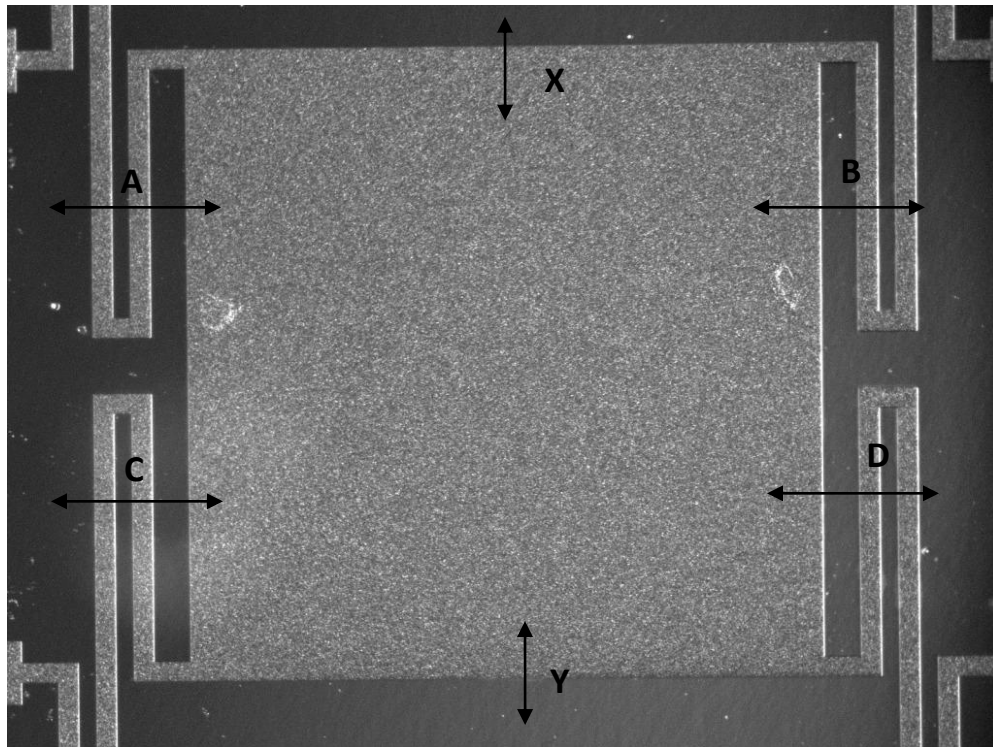


Figure 4.38: Chosen areas for scanning the thickness of the electroplated copper. (pulse plated sample)

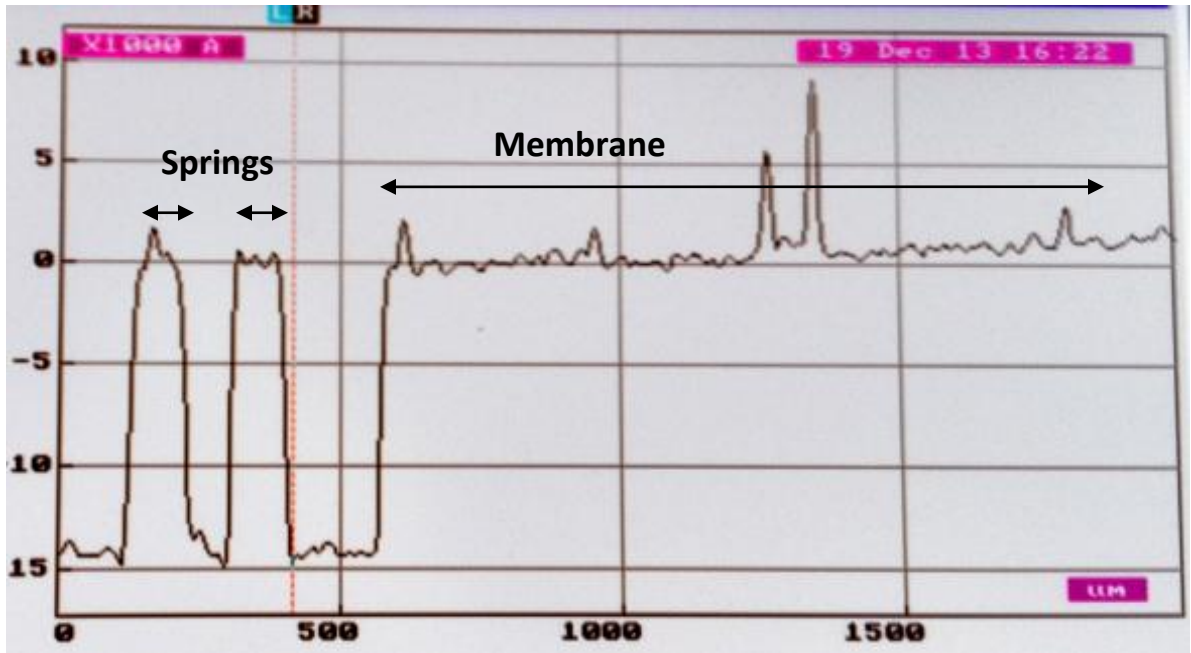


Figure 4.39: Thickness of the electroplated copper over springs and membrane. The membrane were electroplated with a pulsed current electroplating method. The scanned length was 2mm. For the actual value of the thicknesses, the thickness of the photoresist mold should be added to the measured values.

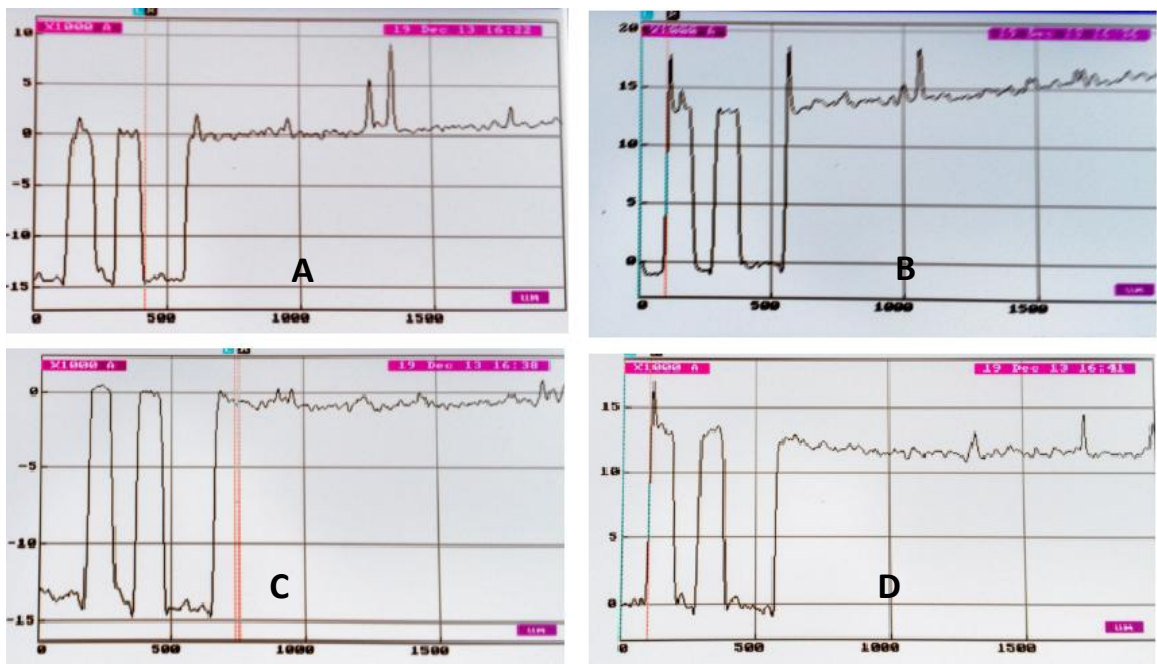


Figure 4.40: Thicknesses of the electroplated copper in different areas.(pulse plated membrane)

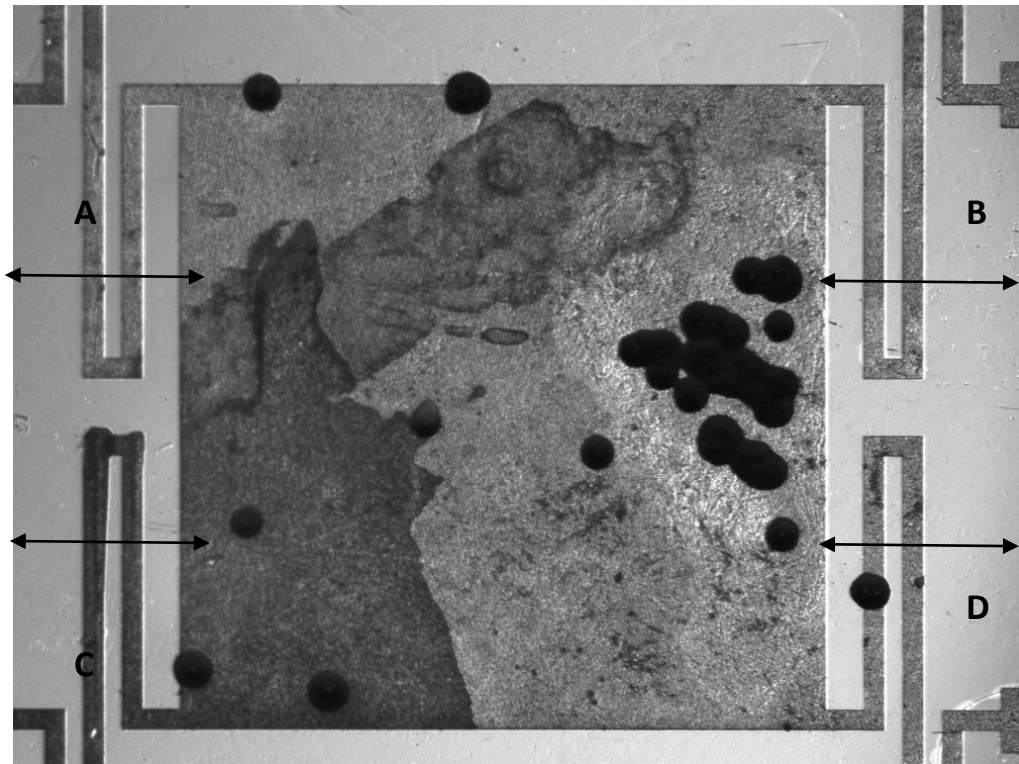


Figure 4.41: Chosen areas for scanning the thickness of the electroplated copper (DC plated sample)

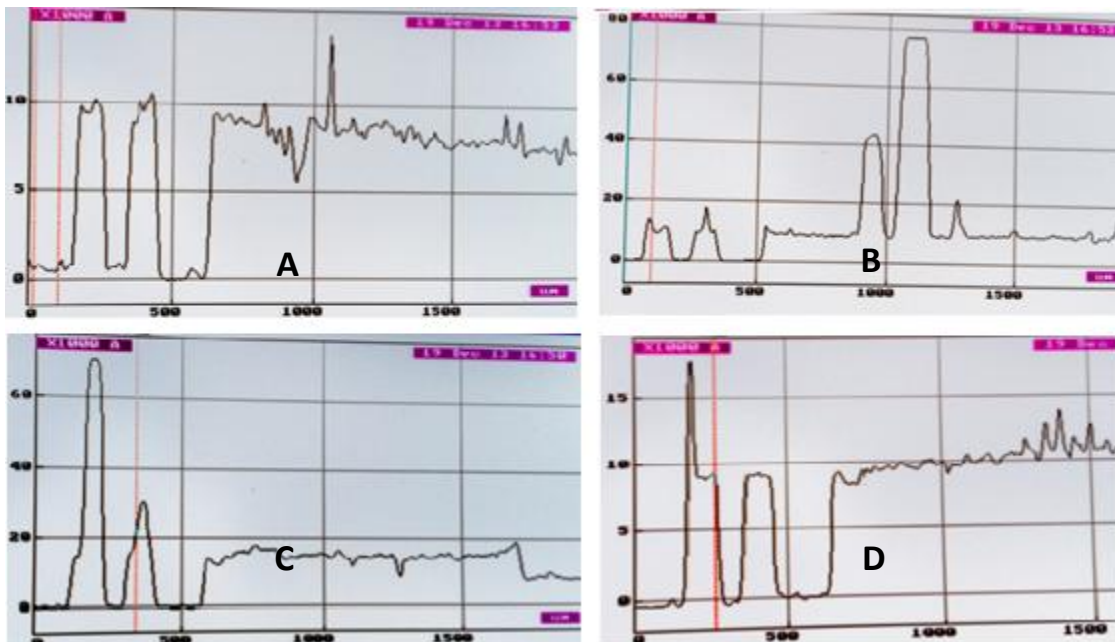


Figure 4.42: Thicknesses of the electroplated copper in different areas. (DC plated membrane)

Scanned results indicate that for the case of the dc plated membranes, the thickness of the electroplated copper in the narrower areas (springs) are more than the thickness in the wider areas (membrane). There are some peaks for the membrane's scanned area which are because of the large plated copper particles; the conclusion has been made by the assumption of neglecting these peaks. For the case of the pulsed plated sample, there is not a significant difference between the thickness of the membranes and springs. This can be considered as benefit of pulse plating over dc plating. Since the measured values in A, B, C, D, X and Y areas does not show that in any specific direction the thickness of the plated film is larger compare to the other directions, It seems that the direction of the flow does not have a significant role in the thickness of the electroplated films. This can be the effect of the plunger, because when it is close to the surface of the sample there is almost no liquid flow in any specific direction.

After the studies on the electroplated membranes were done, the samples were placed on a glass bath of acetone in order to remove the photoresist from the surface of the copper and make the samples ready for the releasing step. The next steps will be etching the seed layer in a copper etch solution and releasing the membranes by etching the remained silicon from the back of the membrane with plasma etching process, and mounting the electroplated membrane on top of the lower electrode. The fabrication of the lower electrode is written in bellow, while the releasing process of the electroplated structure will be investigated in details in the next chapter.

### 4.3 Fabrication of the lower electrodes

The lower electrodes are fabricated on a slide of glass by sputtering of the copper on top of the glass and patterning it with resist, followed by wet etching to form the lower electrodes structures.



Figure 4.43: copper sputtering, patterning and etching on top of glass for making the lower electrodes

#### 4.3.1 Lower electrode microfabrication process

The lower electrodes for applying the electrostatic field have been fabricated by sputtering of 1  $\mu\text{m}$  of copper on top of a slide of glass (a 25nm adhesion layer of titanium has been sputtered on top of the glass slide before sputtering of the copper). Then sputtered copper patterned with HPR504 photoresist, followed by a wet etching in a copper etch bath. At the end BOE (buffered oxide etch) process is used for removing of the titanium adhesion layer.

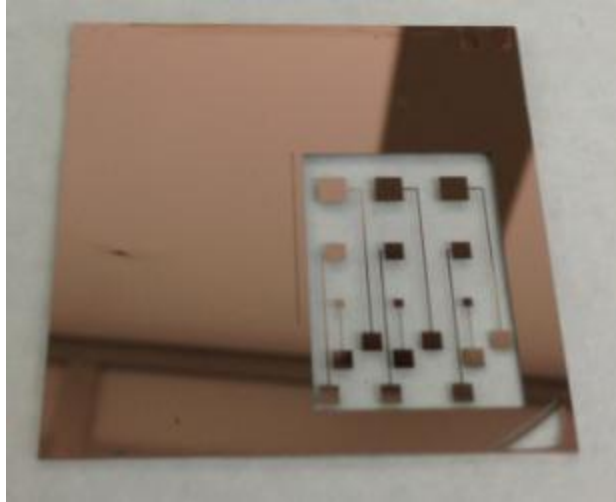


Figure 4.44: Fabricated lower electrodes

# **5. Chapter Five**

## **Sensor Release & Tests**

As mentioned in chapter four, the photoresist mold has been removed by placing the electroplated samples in a acetone bath. The releasing process of the electroplated structures will start with etching of the copper seed layer, and followed by etching of the silicon in plasma etch.

## 5.1 Sensor releasing process design

1- The seed layer is etched.



Figure 5.1: Etching the seed layer

2- The structure is released by etching the silicon from the backside of the wafer with plasma etching process.



Figure 5.2: Releasing the membranes and springs by etching of the silicon

3- By placing the fabricated sensor on top of the lower electrode the fabrication process will be completed.



Figure 5.3: placing the fabricated membranes on top of the electrodes

## 5.2 Etching the copper seed layer

Several factors should be considered for choosing the appropriate method for etching the copper seed layer. There are several solutions which are capable of etching the copper in our clean room. The most important factor to take into the account is that the etch rate of the sputtered copper (seed layer) and the electroplated copper (The sensor structure) might be different. The other important factor is the etch rate in the solution which is being used should not be too fast. Because the etching process will be done manually and if the etching process occurs very fast it might cause over etch on the electroplated sensor structure and results in failure of the sample.

The first choice for copper etching is using copper etch solution which has the etch rate around  $1 \mu\text{m}/\text{minute}$  in the room temperature for sputtered copper. This means for a seed layer with thickness of  $150\text{nm}$ , 10 second should be enough. As a test one of the electroplated samples with thickness of  $3.21\mu\text{m}$  was placed in the etching solution and the etching process stopped by placing the sample in the DI water within 10 seconds. The result was not as expected and there was still a continuous copper seed layer on the surface of the sample. Therefore the sample was placed in the etching solution three more

times (each time for 10 seconds) until the seed layer totally removed from the surface. The total time of the etching was 40 seconds. Figure 5.4 shows the membrane and springs after etching of the seed layer.

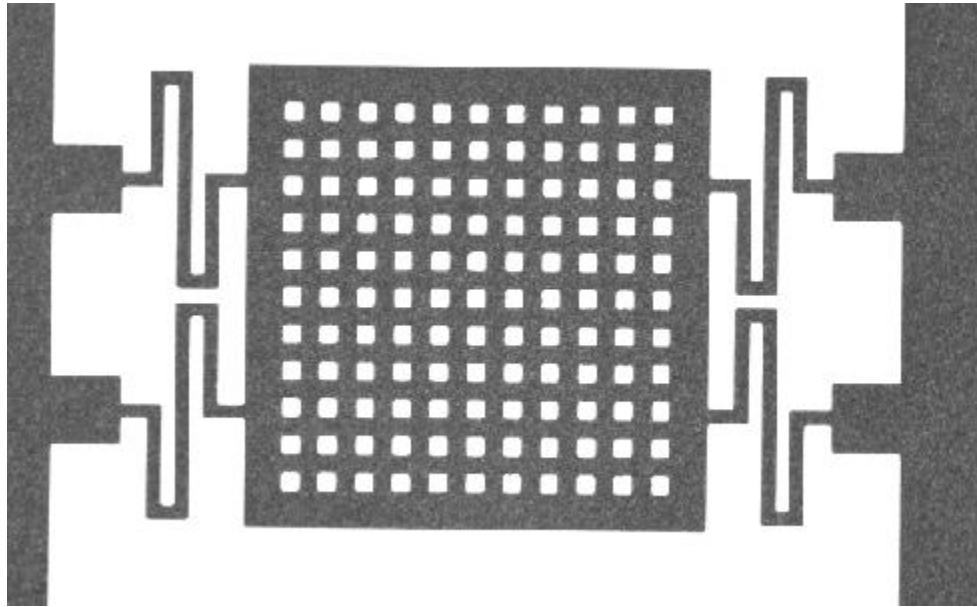


Figure 5.4: The electroplated membrane after etching of the seed layer

After the etching has been done the thickness of the electroplated copper was measured to be  $3.15\ \mu\text{m}$ . Comparing the results with the thickness of the membrane before the etching is showing that the electroplated copper has been etched  $60\text{nm}$  more than the seed layer. Some portion of this difference could be due to the over etch after the seed layer was completely etched, but by neglecting this factor it can be concluded that the etch rate for the electroplated copper is maximum 40% faster compare to the etch rate for the sputtered copper. Due to the thickness of the structure, around  $3.2\ \mu\text{m}$ ,  $60\text{nm}$  of extra etch will not cause any negative effect on the electroplated sensor structures. Therefore, this method is completely safe and effective for seed layer etching in a sense that it will completely etch the seed layer while the electroplated structure is almost untouched.

### 5.3 Etching the titanium adhesion layer

After finishing the copper etching, titanium adhesion layer is etched. Both wet etching and plasma etching are capable of removing the titanium. Since the plasma etching method have the capability of removing the titanium after finishing the silicon back etching or before that, it has been decided to use this method first, for the first sample. Therefore for the first sample test the etching has been done on a plasma etching system.

#### 5.3.1 Releasing the first sample

For releasing the first sample test, it was decided to etch the silicon from the backside until all the silicon is removed and just a layer of titanium remained in the frontside and then by removing the titanium from the frontside releasing the membranes and springs. The reason is we cannot etch the titanium of under the electroplated copper. In order to start the silicon etching in the backside, it is necessary to remove the native silicon oxide which is grown on the backside of silicon wafer first; otherwise the silicon etching will not occur. For removing the native oxide the sample has been placed in the plasma etcher system and silicon oxide has been etched by using  $\text{CF}_4$  and  $\text{O}_2$  with the recipe shown below:

Table 5-1: The recipe for silicon oxide etching, in plasma etching system with  $\text{CF}_4$  and  $\text{O}_2$

ICP (W)	RIE (W)	$\text{CF}_4$ (sccm)	$\text{O}_2$ (sccm)	Pressure (sccm)	Time (sec)
300	45	45	5	50	20

As a reminder the thickness of the native oxide is in range of 10° to 30° and the above process will just acting as a cleaning process before starting the silicon etching process. After the silicon oxide was removed, the silicon etching process was run in presence of SF<sub>6</sub> as below:

Table 5-2: The recipe for silicon etching, in plasma etching system with SF<sub>6</sub>

<b>ICP (W)</b>	<b>RIE (W)</b>	<b>SF6 (sccm)</b>	<b>Pressure (sccm)</b>	<b>Time (min)</b>
300	45	45	50	~45

The silicon etching process was run for 10 min each time and the sample checked to see if still any silicon remained or not. After four times of etching most of the silicon in the backside has been removed and the sample has been placed with the frontside upward in order to remove the titanium. Before running the titanium etch process a change in the color of the electroplated copper was observed, the color of the copper was changed to black, dark brown and dark green in some areas. (Figure 5.5)

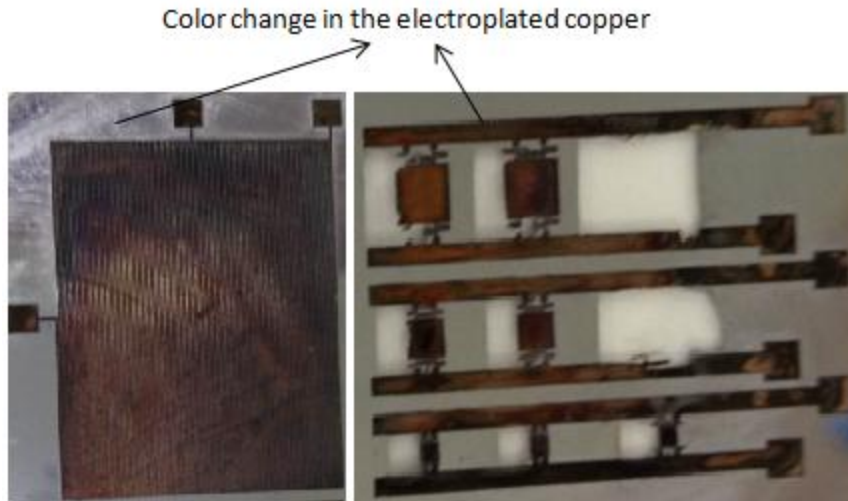


Figure 5.5: Sulfurised electroplated copper after the plasma etching

The recipe for titanium etching is shown below:

Table 5-3: Recipe for Titanium etching, in plasma etching system with CF<sub>4</sub> and oxygen

ICP (W)	RIE (W)	CF <sub>4</sub> (sccm)	O <sub>2</sub> (sccm)	Pressure (sccm)	Time (sec)
300	45	45	5	50	60

After the plasma etching of the titanium, most of the springs were broken. However, still some titanium was remained on the surface of the wafer and between the springs and membranes.

After the first try for releasing of the membranes and springs these results were observed:

- 1- The springs were broken in the last step (removing of the titanium). Therefore, a possible way for improving the releasing process might be removing the titanium

from the front surface and then etching the silicon from the backside for releasing the structures with more safe approach.

- 2- The change in the color of the copper seems to be oxidization on the surface or change in the color of the copper due to the temperature change during the plasma etching.

### **5.3.2 Releasing the second sample**

For releasing the second sample it was decided to first remove the titanium from the frontside and then start to etch the silicon from the backside. To do so, the same recipe as Table 5-3 is used. First the wafer cleaning process to remove the native oxide was done and then the silicon etching was done as mentioned in the previous section. After that the sample was placed with the backside upwards to start the silicon etching.

#### **Color change during the release process**

After the first period of silicon etching with  $\text{SF}_6$  was done the same color change on the electroplated copper has been observed. This color change was quite confusing because the same releasing process has been used before with the older generation of sensors, which had a layer of sputtered copper on top of them, but no change in the color of the color were reported for them. In order to check this difference, a sample of electroplated sensors was used which still had the copper seed layer in none plated areas. As you can see in Figure 5.6, after the plasma etching in the  $\text{SF}_6$  with the same recipe the electroplated areas changed in their color to dark green and brown while for the sputtered seed layer areas the copper seems to be untouched and there is no change in the color of sputtered copper.

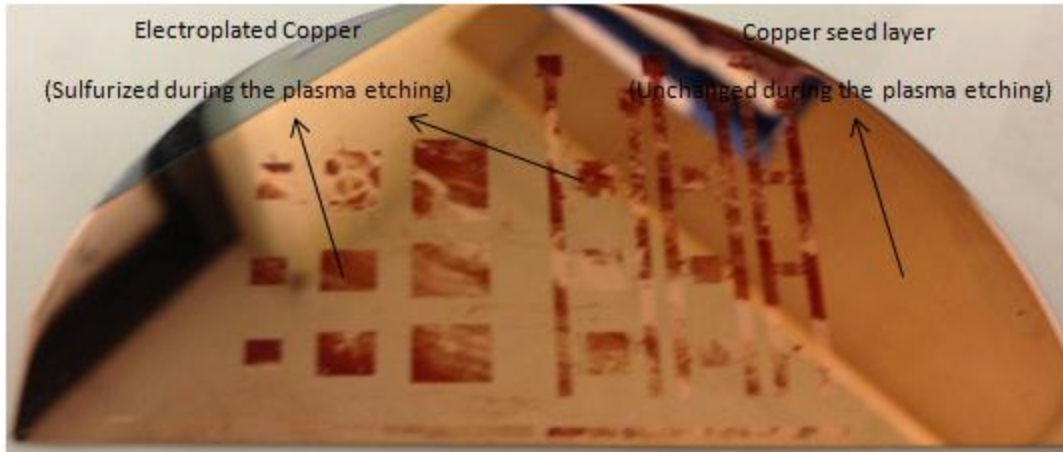


Figure 5.6: The color change in the electroplated copper during plasma etching with SF<sub>6</sub>

By reviewing the literature [47] it was found out that sulfur can have a chemical reaction with copper, which will result in copper sulfide. In fact the dark green and brown areas might be the color of copper sulfide. The reason might be the more porous surface of the electroplated copper compared to the sputtered copper, which will facilitate the reaction between the sulfur and copper. The electrical resistance of the electroplated copper after the SF<sub>6</sub> etch was measured and values in the range of the mega ohms were observed. This value before the SF<sub>6</sub> etch was measured as low as 2 ohms. This shows that this chemical reaction will change the copper to a poorly conductive material, which is absolutely undesirable for the functioning of the sensor. Also the thickness of the damaged copper has been measured and it increased after the SF<sub>6</sub> etch. The thickness of the electroplated copper was measured as 4.2μm before the releasing process however the thickness of the damaged copper was found to be 5.1μm.

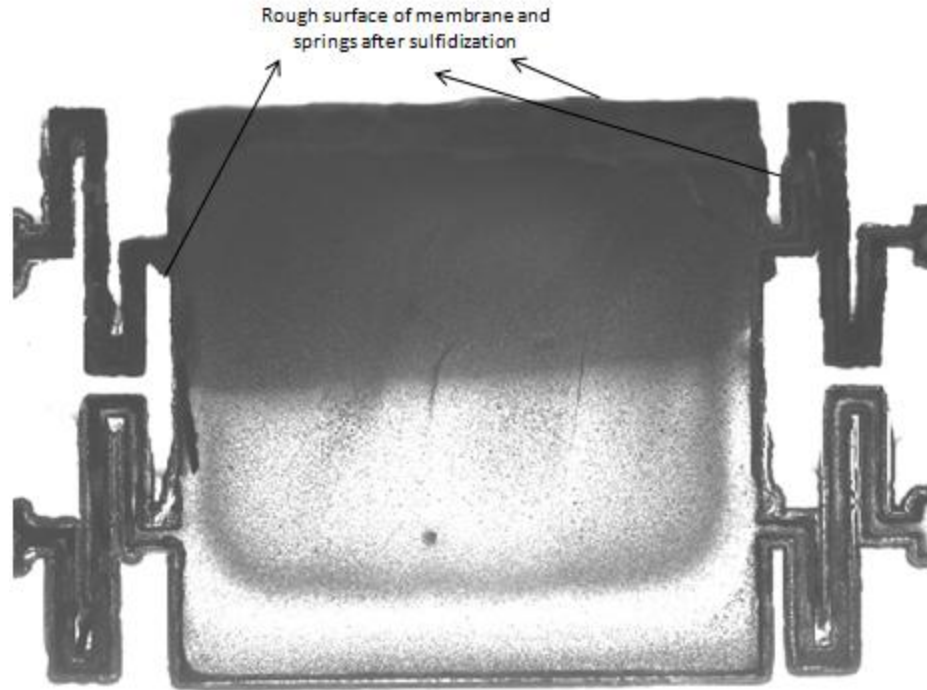


Figure 5.7: The image of the electroplated membrane after plasma etching under microscope

### **Releasing process modification**

After finishing the second sample releasing, results were indicating that the release process should be modified. The first modification should be in titanium etching. While the titanium plasma etching has been reported successfully for many times in our lab, but our experiments shows that it is not 100%. The other method of etching the titanium adhesion layer is using BOE process (Buffered oxide etch), also known as buffered HF or BHF, which is a wet etchant used in microfabrication. As mentioned in fabrication of the lower electrode section, the titanium adhesion layer that had the same thickness, etched successfully by using BOE. The other benefit of this method is that BOE process will etch native silicon oxide and this will reduce the releasing steps. The other releasing step

that should be modified is the silicon etching. The results of the silicon etching with SF<sub>6</sub> are indicating that SF<sub>6</sub> will destroy the electroplated copper. An alternative for silicon etching is using XeF<sub>2</sub> gas. This process will be much slower, but it will not touch the electroplated copper. Therefore the new releasing method will be as show below:

- 1- Etching the titanium with BOE process. This will etch the native silicon oxide at the same time.
- 2- Placing the sample in the XeF<sub>2</sub> gas etching system to etch the silicon.

## **6. Chapter Six**

### **Conclusion & Future works**

In this project a MEMS membrane based electric field sensor was designed and modeled with COMSOL multi-physics software. In the second step the process for the fabrication of the sensor was designed and the electroplating process as one of the most important fabrication steps was optimized. After the sensor structures were electroplated successfully on the silicon wafer, the last step (releasing) was done. In this chapter we will summarize the conclusions from all three steps (Modeling & simulation, Fabrication & electroplating, Releasing) and after that will introduce the future works for each step to improve the next generation of the sensors.

## 6.1 Conclusions

### ❖ Modeling and simulation

- A MEMS based electrostatic field sensor was presented which uses capacitive interrogation of an electrostatic force deflected microstructure. The deflection of the sensor is calculated both by simulation and theoretical model and it was shown that the results of the simulations agree with the theoretical model.
- Simulation models were also designed to solve the vibration issue of the membrane under ac electric fields. It was shown that by adding perforations to the surface of the membrane, it is possible to reduce the air drag effect on the membrane and still have similar electrostatic force on it. This will reduce the damping in membrane movement due to air resistance during ac fields measurements.
- Simulation models also showed that the air drag forces to the surface of the solid membranes gets close to 10% of the electrostatic force. By adding perforations

this value reduced to less than 1%. This illustrates that adding perforations will facilitate the movement of the membrane by reducing the air drag force.

#### ❖ Fabrication & electroplating

- Electroplating process parameters such as forward and reverse current amplitude, duty cycle were optimized to have the lowest roughness over thickness ratio.
- The photoresist patterning has been done successfully for making thick molds of resists for electroplating, with two different photoresists. The 11 $\mu\text{m}$  thick resist mold has been fabricated on top the silicon wafer by one time spinning of SPR-220 photo resist. However, due to the problems with getting the repeatable results it has been decided to use 504 photoresist to get photoresist molds with thicknesses over 3 $\mu\text{m}$ .
- The electroplating of copper made membranes with thicknesses over 4 $\mu\text{m}$  was done successfully.
- After the problem which occurred for the current power source of the plating system. A circuit was designed to provide the current through the electroplating bath. At the first try with dc power supply, the electroplating of the copper was successful. However, the electroplated copper did not have good quality, because of high surface roughness. This problem was solved by using a pulsed power supply and choosing the plating parameter as close as possible to the optimized value.

#### ❖ Releasing

- After the plasma etching of titanium, some titanium will remain between the springs and will not allow them to be released completely. BOE process should be used for etching of the titanium, instead of plasma etching.
- $\text{SF}_6$  in plasma etcher will react and with electroplated copper. Damaged copper has less mechanical robustness and more importantly is a poor conductor, which will disturb the sensor functioning. The measurements indicate that the thickness of the damaged copper is more than the original electroplated copper. During the plasma etching process it has been observed that  $\text{SF}_6$  will not react with the sputtered copper, but it will react with electroplated copper this might be due to more porous surface of electroplated copper compared to the sputtered one.  $\text{XeF}_2$  etching should be used for etching the silicon and releasing the membranes.

## 6.2 Future works

### ❖ Modeling and simulation

- The thickness of the membranes should be simulated in a wider range to find the optimized thickness which provides the best sensitivity.
- The size and number of the holes should be modeled in wider range to find out the optimized number of holes which will reduce the surface area of the membrane for facilitating the movement of the membrane under the ac field while the electrostatic charge on the membrane is still much higher than the electrostatic charge on the lower electrode.
- The space between the membrane and lower electrode should be modeled to find the optimized value which has the highest sensitivity of the capacitance change.

### ❖ Fabrication & electroplating

- The electroplating process parameters such as frequency, amplitude of the reverse and forward current and duty cycle should be optimized more accurately.
  - The characteristics of the electroplated films such as film stress and robustness should be studied in more details in order to get better film quality. High stress may cause failure during the releasing process. Even if the devices survive during the releasing process, the stress may cause tilt in the springs or unwanted curvature on the membrane, which will reduce the efficiency of the sensor.
- ❖ Releasing
- The titanium plasma etching process should be replaced with BOE wet etching in order to successfully etching the titanium adhesion layer.
  - Also silicon plasma etching process should be replaced with  $\text{XeF}_2$  gas etching in order to avoid the  $\text{SF}_6$  reaction with the electroplated copper.

# 7. References

- [1] C. James Dahn, B. N. Reyes, A. Kashani, and J. Finkelshtein, "Electrostatic Hazards of Explosive Propellant And Pyrotechnic Powders", Electrical Overstress/Electrostatic Discharge Symposium Proceedings, 6-8 Oct. 1998, pp. 139-150.
- [2] G. Luttgens and S. Luttgens, "Preventing electrostatic hazards of flexible intermediate bulk containers", Conference Record of the 2000 IEEE Industry Applications Conference, 2000, Vol. 1, pp. 666-669.
- [3] M.Glor, "Electrostatic ignition hazards associated with FIBC filling or emptying and presently available FIBC safety design types", IEE Colloquium on Hazards in Powder Handling with FIBCs: Standards, Measurements and Case Studies (Digest No. 1997/001), 17 Apr. 1997, pp. 21-23.
- [4] BP International, "Hazards of electricity and static electricity", Institution of Chemical Engineers, 2006.
- [5] K. Campden, "Electrostatics field of interest", IEE Review, 17 Oct. 1991, Vol. 37, Issue 10, pp. 335-338.
- [6] D. M. Taylor, P. E. Secker, "Industrial Electrostatics: Fundamentals and Measurements", John Willey & Sons Inc., New York, 1994, ISBN-0-471-95233-8.
- [7] J. Chubb, J. Harbour, "A system for the advance warning of risk of lightning", Proceedings of the Electrostatics Soc. America, June 2000.

- [8] C. L. Ziegler, D.R. MacGonnan, "Observed lightning morphology relative to modeled space charge and electric field distribution in a torondic storm", *Journal of Atmospheric Science*, vol. 51, pp. 833-851,1993.
- [9] K.L. Cummins, E. Philip Krider, Mark D. Malone, "The U.S. National Lightning Detection Network and Applications of Cloud-to-Ground Lightning Data by Electric Power Utilities:", *IEEE transactions on electromagnetic compatibility*, vol. 40, November 1998, pp. 465-480.
- [10] C. Poole, D. Trichopoulos, "Extremely low-frequency electric and magnetic fields and cancer", *Cancer Causes and Control*, Jul. 1991, Vol. 2, No. 4, pp. 267-276.
- [11] J. Schuz, "Exposure to electromagnetic fields and cancer", *The epidemiological evidence*, General Assembly and Scientific Symposium, 13-20 Aug. 2011, pp. 1- 4.
- [12] Y. Guo-Sheng, W. Jiang, Han Chun-Xiao, Liu Yu-Liang, Deng Bin, and Wei Xi-Le, "Bifurcation analysis of a minimal neuron to ELF AC electric field", 30<sup>th</sup> Chinese Control Conference, 22-24 Jul. 2011, pp. 594-598.
- [13] I.Vbzquez, R. Hemhdez-Corona, and G. Montoya-Tena, "Diagnostic of nonceramic insulators aged in a salt fog chamber by using electric field sensor", *Conference Record of the 2004 IEEE International Symposium on Electrical Insulation*, Indianapolis, IN USA, 19-22 September 2004, pp. 471-474.
- [14] G. H. Vaillancourt, S. Carignan, and C. Jean, "Experience with the Detection of Faulty Composite Insulators on High-Voltage Power Lines by the Electric Field Measurement Method, *IEEE trans. on power delivery*, Apr. 1998, Vol. 13, pp. 661-666,.
- [15] C. Peng, P. Yang, S. Liu, H. Zhang, K. Feng, and S. Xia, "Detecting internal defect of non-ceramic insulators using a novel micromachined electric field sensor", *IEEE 24th*

International Conference on Micro Electro Mechanical Systems (MEMS), Cancun, MEXICO, January 23-27, 2011, pp 561-564.

[16] H. Okubo, A. Sawacla, K. Kato, and M. Hikita, "Direct Measurement of Electric Field using Kerr Electro-Optic Method in Transformer Oil Pressboard Composite System at dc Polarity Reversal", Conference Record of the 1998 IEEE International Symposium on Electrical Insulation, Arlington, Virginia, USA, June 7-10, 1998, Vol. 2, pp. 486-489.

[17] IEEE standard procedure for measurement of power frequency electric and magnetic field from ac power lines (IEEE standard 644-1994), The Institute of Electrical and Electronics Engineers Inc., New York, 1995.

[18] IEEE recommended practices for instrumentations: Specifications for magnetic flux density and electric field strength meters- 70 Hz to 3 kHz (IEEE standard 1308-1994), The Institute of Electrical and Electronics Engineers Inc., New York, r99s.

[19] D.K Cheng,. Field and wave electromagnetics. Vol. 2. New York: Addison-Wesley, 1989.

[20] D. M. Taylor and P. E. Secker, "Industrial Electrostatics: Fundamentals and Measurements", John Willey & Sons Inc., New York, 1994, ISBN-0-471-95233- 8.

[21] Y.Zhou, "Investigation of a Micromachined Electric Field Mill to Maximize the Electrostatic Field Sensitivity", M.sc Thesis, University of Manitoba, 2011.

[22] A.Roncin, C.Shafai, and D.R. Swatek, "Electric field sensor using electrostatic force deflection of a micro-spring supported membrane", Sensors and Actuators A, Sept. 2005, vol. 123-124, pp. 179-184.

[23] T.Chen, E.Tahmasebian, and C.Shafai, "MEM electric Field sensor using force deflection mechanism", Manitoba Materials Conference, Spring 2013.

- [24] M. N. Horenstein and P. R. Stone, "A micro-aperture electrostatic field mill based on MEMS technology, " *J. Electrostat.*, May 2001, Vol. 51–52, pp. 515–521.
- [25] P. Yang, H. Zhang, Shiguo Liu, D. Fang, and S. Xia, "A high sensitivity SOI electric-field sensor with novel combshaped microelectrodes", 16th International Solid-State Sensors, Actuators and Microsystems Conference, 5-9 Jun. 2011, pp. 1034-1037.
- [26] C. Xianxiang, P. Chunrong, H. Tao, C. Ye, Q. Bai, S. Chen, and S. Xia, "Thermally driven micro-electrostatic fieldmeter", *Sensors and Actuators A: Physical*, 20 Nov. 2006, Vol. 132, Issue 2, pp. 677–682.
- [27] G. Wijeweera, B. Bahreyni, Cyrus Shafai, and Athula Rajapakse, "Micromachined electric-field sensor to measure AC and DC fields in power systems", *IEEE Trans. Power Delivery*, July 2009 ,vol. 24, pp. 988-995.
- [28] M.Gad-el-Hak (ed) 2002 *The MEMS Handbook* (Boca Raton, FL: CRC Press)
- [29] N.William, Jr.Sharpe, editor, *Springer Handbook of Experimental Solid Mechanics*.Springer, Berlin, 2008. ISBN: 0-387-34362-8.
- [30] COMSOL Multiphysics 4.5, COMSOL, inc., 1998 - 2011.
- [31] T. Chen and C. Shafai, "MEM Electric Field Sensor using Force Deflection with Capacitance Interrogation," 2013 IEEE Power & Engineering Society (PES) General Meeting, Vancouver, July 21-25, 2013.
- [32] 24-Bit Capacitance-to-Digital Converter with Temperature Sensor (AD7747 datasheet), Analog Devices, 2007 [Online].

- [33] M. Roh, J. Lee, W. Kim, J. Jung, (2013) "Cu filling of TSV using various current forms for three-dimensional packaging application", *Soldering & Surface Mount Technology*, Vol. 25 Iss: 4, pp.209 – 217.
- [34] G. Kandlikar, "Evolution of Microchannel Flow Passages--Thermohydraulic Performance and Fabrication Technology" *Grande Heat Transfer Engineering* Vol. 24, Iss. 1, 2003
- [35] S.H. Oh, S.H. Lee, J.C. Jeon, M.H. Kim, S.S. Lee, "Bulk-micromachined circular foil type micro heat-flux sensor", *Sensors and Actuators A: Physical*, Volume 132, Issue 2, 20 November 2006, pp. 581-586.
- [36] J. Y.Park, , G.H. Kim, K.W. Chung, "Electroplated rf MEMS capacitive switches," *Micro Electro Mechanical Systems, The Thirteenth Annual International Conference on MEMS*, 23-27 Jan 2000 , pp.639-644.
- [37] [http://en.wikipedia.org/wiki/Electroplating#mediaviewer/File:Copper\\_electroplating.svg](http://en.wikipedia.org/wiki/Electroplating#mediaviewer/File:Copper_electroplating.svg). 2014.08.07
- [38] A.Motieifar, "Investigation of Performance and Fabrication of Metal Microfluidic Heat Sinks", M.sc Thesis, University of Manitoba, 2009.
- [39] J. T. Hinatsu, and F. R. Foulkes, "Diffusion Coefficient for Copper (II) in Aqueous Cupric Sulfate-Sulfuric Acid Solutions", *Journal of Electrochemical Society*, Vol. 136, i989, PP. 125-132.
- [40] W. Tsai, C. Wan, and Y. Wang, "Pulsed Current and Potential Response of Acid Copper System with Additives and the Double Layer Effect", *Journal of Electrochemical Society*, Vol. 149, No. 5, 2002,pp. C229-C236

[41] C. Van Horn, "Pulsed Current Plating, in ASM Handbook", ASM International, 1994.

[42] E. J. Podlaha, and D. Landolt, "Pulse Reverse Plating of Nanocomposite Thin Films", Journal of Electrochemical Society, 1997, Vol. pp. L200-L202.

[43] K. Ogura, K. Sakurai, and S. Uehara, "Room Temperature-Coloration of Stainless Steel by Alternating Potential Pulse Method", Journal of Electrochemical Society, 1994, Vol. 141, pp. 648-651.

[44] L.J. Dumey, "Electroplating Engineering Handbook", 4th Edition, Van Nostrand, 1984, Berkshire.

[45] C. Van Horn, "Pulsed Current Plating, in ASM Handbook", ASM International, 1994.

[46] N. Tantavichet, and M. Pritzker, "Low- and High-Frequency Pulse Current Plating of Copper onto a Rotating Disk Electrode", Journal of Electrochemical Society, Vol. 149, No. 5, 2002, pp. C289-C299.

[47] N. Greenwood, A. Earnshaw, (1984). Chemistry of the Elements. Oxford: Pergamon Press. p. 1373. ISBN 0-08-022057-6.

# 8. Appendix 1

## Preparing the plating solution

1. To an appropriately cleaned electroplating tank, add approximately 50% of the final total tank volume, with deionized water.
2. Add the required amount of liquid copper sulfate pentahydrate (22.2% v/v for high aspect ratios) and thoroughly mix.
3. SLOWLY, with thorough mixing, add C.P. grade concentrated Sulfuric Acid (SG 1.84). (CAUTION!! This reaction is EXOTHERMIC: a considerable amount of heat will be generated.)
4. Bring the solution level to operating level with deionized water.

5. Using a 1 micron polypropylene filter cartridge, continuously filter the solution in the electroplating tank and allow the solution to cool to 27°C (80°F).
6. Determine the chloride ion concentration. Add C.P. grade concentrated Hydrochloric acid (SG 1.18) to raise the chloride level to 60 ppm (60mg/l) [2.64 ml/100 liters; 10 ml/100 gal = 12 ppm (12 mg/l) Chloride ion]. Once added, confirm the chloride concentration and make adjustments, if necessary.
7. Insert bagged anodes into the plating tank.
8. Electrolysis – (Required before running production). Conditioning of Technic CU 2800 solution is required to film the anodes and produce optimum conditions of operation.
  - A. With the solution cooled to 27°C (80°F), Pre-electrolyze using clean copper-clad laminate cathodes according to the following schedule. Electrolyze solution at 0.5 A/dm<sup>2</sup> (5 A/ft<sup>2</sup>) for 3 hours.
  - B. Next, add 0.7% v/v (7.0 ml/l) of TECHNIC CU 2800 Brightener, 0.7% v/v (7.0 ml/l) of TECHNIC CU 2800 Carrier and mix thoroughly. (0.7% v/v (7.0 ml/l) is 0.7 gallon per 100 gallons of the final bath volume.) If using new anode bags, an additional 0.02 to 0.4% v/v (0.2 – 0.4 ml/l) may be required due to absorption by the anode bags. Allow the solution to thoroughly mix for 20 minutes before moving to step C.
  - C. Next, electrolyze the solution using a new set of clean copper-clad laminate cathodes according to the following schedule. Electrolyze the solution at 0.5 A/dm<sup>2</sup> (5 A/ft<sup>2</sup>) for 2 hours. Make TECHNIC CU 2800 Replenisher additions every hour equal to 1.0 ml/Amp-

hr. Check the chloride concentration and adjust to 60 ppm, if necessary. D. Electrolyze solution at 2 A/dm<sup>2</sup> (20 A/ft<sup>2</sup>) for 3 hours. Make TECHNIC CU 2800 Replenisher additions every hour equal to 1.0 ml/Ampconcentration and adjust to 60 ppm, if necessary.

9. The solution is now ready.

Table A-8-1: solution mixture for making one liter of the electrolyte

<b>Chemicals required</b>	<b>1 Liter</b>	<b>1 gallon</b>
Deionized water	644 ml	64.4% v/v
Purified Liquid Copper Sulfate [270 g/l (36 oz/gal) CuSO <sub>4</sub> ·5H <sub>2</sub> O]	222 ml	22.2% v/v
C.P. Grade Concentrated Sulfuric Acid (H <sub>2</sub> SO <sub>4</sub> )	120 ml	12% v/v
C.P. Grade Concentrated Hydrochloric Acid (HCL)	0.13 ml	0.013% v/v
TECHNIC CU 2800 Brightener	7.0 ml	0.70 % v/v
TECHNIC CU 2800 Carrier	7.0 ml	0.70 % v/v